Modelling and processing of flexural wave noise in sea ice

Kristian Jensen

Thesis for the degree
Master of Science

DEPARTMENT OF EARTH SCIENCE

UNIVERSITY OF BERGEN

April 2016

Abstract

One of the most common problems with seismic data obtained on sea ice is the presence of flexural ice wave noise on the seismic raw data. Flexural wave noise occurs on seismic data acquired on ice in the so-called transition zone between the shoreline and deep sea. As the flexural waves are highly dispersive they are manifested as a broad fan of noise on the seismic data, often having an order of magnitude 40-60 dB higher than reflected signals. In addition, the frequency spectrum of flexural ice waves frequently overlaps with reflected signals, and due the low velocities of flexural waves, spatial aliasing commonly occurs. Thus, flexural waves may be difficult to remove using conventional seismic processing techniques.

This study outlines how flexural waves can be modelled and discuss various processing techniques for removing energy related to the flexural waves while preserving the reflected signals as much as possible. Modelling and processing help us to understand how various parameters such as ice temperature and ice thickness affect the flexural wave pattern, which can be important when designing a proper processing work flow. For this study, three primary processing methods have been applied and compared on several datasets: conventional frequency-wave number ($f-k$) processing, slant-stack ($\tau-p$) processing, and radial trace (RT) transform processing.

Modelling reveals that a decrease in ice temperature and/or an increase in ice thickness will increase the phase velocity of the flexural waves whereas the same is true for group velocities at lower frequencies only. Testing of processing work flows indicate that when receivers are densely spaced to better exclude spatial aliasing problems, the best results are obtained with conventional $f-k$ filtering. At larger receiver offsets, however, a combination of $\tau-p$ and RT filtering produces the best results on both synthetic and real data. Thus, not one single method will always produce the best result, and different processing approaches may be used depending on the data at hand.

Acknowledgements

This thesis has been written at Department of Earth Science, University of Bergen, under the supervision of Professor Tor Arne Johansen (principal supervisor) and Senior Engineer Bent Ole Ruud (co-supervisor). I would, first and foremost, like to extend my sincere gratitude to my supervisors for excellent follow-up, assistance, and multiple interesting discussions during my work on this thesis. Your assistance has been greatly educational as well as inspiring and motivational. Bent Ole's assistance on MATLAB issues and processing techniques has, in particular, been invaluable to this thesis.

Further, I would like to thank Professor Emeritus Einar Mæland for continuously giving me feedback and helpful input during the writing stages of this study, and I would also like to thank Postdoctoral researcher Marcus Landschulze for advice, tips and assistance regarding the finer details of signal theory. In addition, I am very grateful to everyone in Professor Tor Arne Johansen's research group and at the Department of Earth Science for their input at various stages of the process. Special mentions should go to PhD-Candidate Ronny Tømmerbakke with whom I have shared office this year, and who has continually looked at my progress and offered suggestions, as well as Professor Stéphane Rondenay who took his time to discuss various sampling problems with me.

I also want to thank Research Geophysicist David C. Henley at CREWES, University of Calgary, for responding quickly to e-mails regarding some questions I had about the RT transform. His input was very helpful in making me understand the inticracies of the transform.

Finally, I would like to thank my wife, Iryn, and my children, Tristan and Katrin, for their continuous love and support.

Contents

Chapter 1

Introduction

Seismic acquisition in Arctic environments poses several difficult challenges. Harsh working environments, unpredictable weather, changing ice dynamics, logistics challenges, dangers from local wildlife, and general Health, Safety and Environment (HSE) risks must be taken into account at all times (e.g. Johansen et al. (2011), Rice et al. (2013)). In addition, any seismic acquisition operation in Arctic environments must, at all times, adhere to local governmental rules regarding the preservation of the environment so that no harm is inflicted on the natural environment and wildlife (Trupp, Hastings, Cheadle, & Vesely, 2009). Finally, seismic data obtained in the Arctic often require special processing efforts in order to effectively separate signal from noise.

1.1 Motivation

Despite the challenges involved, acquisition of seismic data in Arctic environments is important in order to understand the geology and dynamics of the earth in these environments (Johansen et al., 2011). In addition, much of the world's undiscovered hydrocarbons are located in the Arctic. A 2008 United States Geological Survey estimates that as much as 90 billion barrels of undiscovered, technically recoverable oil and 44 billion barrels of natural gas may be located north of the Arctic Circle. This amounts to 22 percent of the world's undiscovered, technically recoverable resources in the world (United States Geological Survey - Circum-Arctic Resource Appraisal Assessment Team, 2008). Thus, although oil and gas exploration in Arctic environments currently is as much a political as a technical issue, an understanding of the science and challenges behind Arctic seismic exploration remains highly relevant.

Challenges involved in the processing of seismic data obtained in Arctic environments include, but are not limited to, static problems due to varying thickness of near-surface layers, rapid spatial variation of velocity due to localized perennial water bodies or lakes, rapidly changing thickness of ice layers or permafrost layers, seasonal changes in ice dynamics, subsurface dips and irregular source and/or receiver spacing (Trupp et al., 2009). In addition, noise from flexural ice waves usually occurs on seismic data acquired on ice sheets in the so-called transition zone between the shoreline and out to deep sea (Lansley, Eilert, & Nyland, 1984).

The flexural ice waves were first studied extensively in a series of papers published in the 1930s and 1950s (e.g.Ewing, Crary, and Thorne Jr (1934), Ewing and Crary (1934), Press and Ewing (1951a), Press and Ewing (1951b)). Flexural waves are highly dispersive - meaning that the phase velocity changes with frequency. Thus, flexural ice waves manifest themselves as a broad fan of noise on the seismic data, often having an order of magnitude 40-60 dB higher than reflected signals (Rovetta, Mazzucchelli, Del Molino, & Sandroni, 2009). An example of flexural wave noise is given in figure 1.1 where the presence of noise on a real dataset obtained outside Sveagruva, Svalbard in 2013 can be seen (this dataset will be processed later in the thesis).

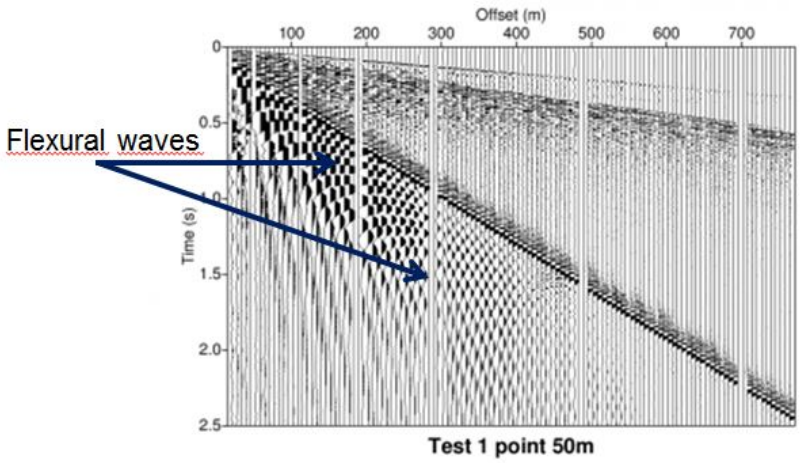

Figure 1.1: Flexural wave noise on seismic data obtained near Sveagruva, Svalbard, 2013.

In addition to the high magnitude of the flexural waves, the frequency spectrum of flexural ice waves frequently overlaps with reflected signals, and due the low velocities of the flexural waves, spatial aliasing commonly occurs. Thus, conventional processing techniques

often fail to remove the flexural wave noise in a satisfactory way while at the same time keeping reflected signals intact.

Although several processing methods have been proposed for removing flexural wave noise, several of which will be presented in this thesis, a standardized procedure has, as of yet, not been developed as the best approach is highly dependent on acquisition parameters and data quality. As such, research into flexural wave noise dispersion issue is still relevant, and it is within this context that this thesis will hopefully bring some insight.

1.2 Objectives

The aim of this thesis is first to model synthetic flexural waves using a fluid-loaded thin plate modelling approach outlined in Yang and Yates (1995) so that a better understanding of the dispersion relation of the waves may be achieved. Using theory outlined in Langleben and Pounder (1963), Cox and Weeks (1974), Cox and Weeks (1983), and Timco and Weeks (2010), it will further be shown how factors such as salinity, ice thickness and temperature affect the dispersion relation of the flexural waves. If an accurate dispersion relation can be modelled, better care can be taken when deciding upon which strategy to use during processing.

Next, the results of applying three different processing techniques on several synthetic and real datasets will be illustrated. The processing methods include conventional $f-k$ filtering, $\tau-p$ filtering, and RT (radial trace) transform filtering.

$f-k$ processing involves transforming the dataset from the offset-time $(x-t)$ domain to the frequency-wave number $(f-k)$ domain via a 2-D Fourier transform. This results in a plane-wave decomposition of the wavefield into harmonic waves, and filtering may now be performed to remove unwanted noise. An inverse 2-D Fourier transform is then applied to transform the dataset back to the $x-t$ domain again.

The $\tau-p$ transform is a method which transforms the data from the $x-t$ domain to the so-called $\tau-p$ domain, where τ represents the time intercept in the $x-t$ domain, and p represents the slowness parameter (in s/m). This method, commonly referred to as slant-stack processing (e.g. Gardner and Lu (1991), Sacchi (2002), Mæland (2005)),

may also allow for a separation of signal and noise in the transformed domain through decomposition of the wavefield into plane waves in the time domain. The noise may then be removed through filtering, and an inverse transform is performed back to the $x - t$ domain.

The RT transform method has been outlined in several articles and conference abstracts by David C. Henley (e.g. Henley (2003), Henley (2004), Henley (2006), Henley (2009)). The method is based on the fact that when sampling along specific velocity trajectories in the $x - t$ domain, one particular frequency component of the flexural wave should be captured along each trajectory. Through spectral clipping in the Fourier domain of each radial trace, the flexural waves may then be attenuated (Henley, 2006). The RT method may be visualized as having an array of receivers moving at different velocities away from the source.

Other methods for flexural wave processing will be briefly discussed, but in order to keep the research within the scope of a master thesis, these methods were not used during processing. Often, however, a combination of the three methods outlined above were used on the various datasets in order to find an optimal work flow to remove the flexural waves.

By comparing the different processing techniques, and evaluating the quality of the modelling and processing strategies, I hope to better illustrate how various parameters may influence the quality of the output of the seismic processing.

1.3 Outline

This thesis is organized as follows:

Chapter 1 outlines the motivations and objectives of the thesis.

Chapter 2 outlines relevant theory for understanding flexural waves and flexural wave dispersion in ice sheets.

Chapter 3 outlines various techniques for seismic processing of flexural ice waves.

Chapter 4 outlines the MATLAB programs used to perform modelling and processing

work as well as the datasets used in the thesis.

Chapter 5 outlines the results of the modelling and processing work.

Chapter 6 features a general discussion on the results achieved, as well as the main conclusions.

Chapter 2

Flexural waves in ice sheets

This chapter will introduce the theory behind flexural waves. First, general theory regarding wave dispersion will be discussed as this theory is fundamental for understanding flexural waves. Next, a summary of the results obtained by Ewing, Crary and Pratt in the 1930s and 1950s (e.g. Ewing et al. (1934), Ewing and Crary (1934), Press and Ewing (1951a), Press and Ewing (1951b)) will be covered as this represents the first detailed studies of flexural waves and flexural wave dispersion in sea ice. Following this, a derivation of the flexural wave dispersion as outlined by Yang and Yates based on fluid-loaded thin plate theory as presented in Yang and Yates (1995) will be outlined as this theory has been used as the basis for the modelling part of this thesis. Finally, there will also be a discussion regarding the theory of how various parameters such as ice temperature, ice salinity and ice thickness influence the wave dispersion based on studies conducted by Langleben and Pounder (1963), Cox and Weeks (1974), Cox and Weeks (1983) and Weeks and Assur (2009).

2.1 Wave dispersion

A common relationship for studying wave motion is given by:

$$c = f\lambda, \tag{2.1}$$

where c is wave velocity (m/s), f is frequency (Hz), and λ is wavelength (m). The frequency is defined as cycles per second, or as:

$$f = \frac{1}{T}, \tag{2.2}$$

where T is the period of the wave in time, or the time it takes for the wave to travel one cycle. Further, the frequency is often defined in terms of angular frequency,

$$\omega = 2\pi f, \tag{2.3}$$

where ω is radians per second.

A wave is a function of coordinates in space and time. If we measure a wave at a specific moment in time, the distance between two similar points on the wave is defined as the wavelength, or λ, as defined above. In this case, we can define the spatial frequency, or wave number, k, as:

$$k = \frac{2\pi}{\lambda}. \tag{2.4}$$

From combining equations 2.1, 2.3 and 2.4 we obtain the relation:

$$\omega = ck. \tag{2.5}$$

This equation is usually referred to as the *dispersion relation* of a wave. Thus, the dispersion relation relates the phase velocity of the wave to the angular frequency.

The same result can also be obtained from the 1-D scalar wave equation. Given:

$$\frac{\partial^2 \psi}{\partial t^2} = c^2 \frac{\partial^2 \psi}{\partial x^2}, \tag{2.6}$$

where ψ represents particle displacement. Now assume that we have a particle displacement defined by $\psi(x,t) = Ae^{i(kx-\omega t)}$ where A is the amplitude of the wave. Inserting this into the 1-D scalar wave equation, we obtain:

$$\omega^2 = c^2 k^2 \Rightarrow \omega = ck, \tag{2.7}$$

which is equivalent to 2.5.

If the frequency of a wave is independent of velocity, then the wave is said to be *nondispersive*. With flexural waves, however, the frequency is not independent of velocity. The waves are then defined as *dispersive*. In order to better understand the features of a dispersive wave, we first have to introduce the concepts of *phase velocity* and *group velocity*.

2.2 Phase velocity and group velocity

To define phase and group velocity we follow Pujol (2003):

Consider an arbitrary wave $f(x,t)$ to be an infinite superposition of plane waves:

$$f(x,t) = \frac{1}{2\pi}\int_{-\infty}^{\infty} A(k)e^{i[\omega(k)t-kx]}\mathrm{d}k. \tag{2.8}$$

It is assumed here that we have a dispersive wave in that $\omega = \omega(k)$.

Further, it is assumed that $A(k)$[1] is zero everywhere except in a small interval $(k_0 - \delta k, k_0 + \delta k)$ in the vicinity of $k = k_0$. In other words, we are superimposing an infinite number of waves with very similar wave numbers and arbitrary amplitudes. The resulting wave is then narrow-band in the k-domain. $\omega(k)$ can now be approximated by using the first order Taylor expansion:

$$\omega(k) \approx \omega(k_0) + \left.\frac{\mathrm{d}\omega}{\mathrm{d}k}\right|_{k=k_0}(k-k_0) = \omega_0 + \omega_0'(k-k_0). \tag{2.9}$$

With this approximation and the identity $k \equiv k_0 + (k - k_0)$, the phase in equation 2.8 can be written as

$$\omega t - kx = \omega_0 t - k_0 x + (\omega_0' t - x)(k - k_0). \tag{2.10}$$

And because k_0 and ω_0 are constants, $f(x,t)$ can be written as

$$f(x,t) = f_0(\omega_0' t - x)e^{i(\omega_0 t - k_0 x)}, \tag{2.11}$$

[1]In Pujol (2003), $\omega(k)$ is written here instead of $A(k)$, but as this would mean that only a small window of the dispersion relation is non-zero, and since $A(k)$ is typically used in this derivation, this might be a typo in the text.

where

$$f_0(\omega_0' t - x) = \frac{1}{2\pi} \int_{k_0-\delta k}^{k_0+\delta k} A(k) e^{i(k-k_0)(\omega_0' t - x)} \mathrm{d}k. \tag{2.12}$$

From this we see that the result of the superposition is equal to the product of a common harmonic wave propagating with velocity $c = \omega_0/k_0$ and a modulating factor given by $f_0(\omega_0' t - x)$. The wave propagating with velocity c is known as the carrier wave, and c is defined as the *phase velocity*. This is the velocity of propagation of a surface with constant phase, because if we have that

$$\omega_0 t - k_0 x = \text{constant}, \tag{2.13}$$

then, differentiating gives:

$$\frac{\mathrm{d}x}{\mathrm{d}t} = \frac{\omega_0}{k_0} = c. \tag{2.14}$$

Further, as ω_0 and k_0 are arbitrary, we can write, in general

$$c = \frac{\omega}{k}, \tag{2.15}$$

which is the definition of phase velocity.

If we now look closer at the modulating factor, we can see that this has a constant phase when

$$\omega_0' t - x = \text{constant}. \tag{2.16}$$

And from this we find that

$$\frac{\mathrm{d}x}{\mathrm{d}t} = \omega_0' = \left.\frac{\mathrm{d}\omega}{\mathrm{d}k}\right|_{k=k_0} = c + k\frac{\mathrm{d}c}{\mathrm{d}k} = U. \tag{2.17}$$

The wave with velocity U varies more slowly than the carrier wave and thus modulates it. The portion of the carrier wave between two consecutive zeros of the modulation wave, or envelope, constitutes a group and, thus, U is known as *group velocity* (Pujol, 2003). For an illustration of the difference between phase and group velocity, see figure 2.1.

In summary, waves are dispersive if there is a difference between phase velocity and group velocity, or, in other words, when $\mathrm{d}c/\mathrm{d}k \neq 0$. Dispersive waves will appear as trains of waves where waves of different frequencies arrive at different times. Waves featuring a

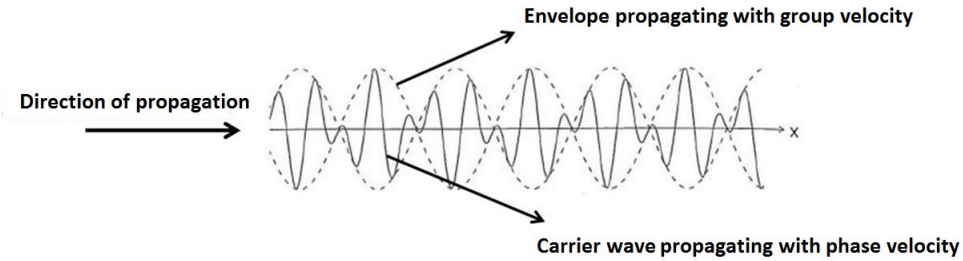

Figure 2.1: Illustration of phase and group velocity.

large frequency band will thus manifest themselves as broad fans on seismic data. The relation between frequency and velocity is usually displayed in a *dispersion curve* which shows how phase and group velocity changes with frequency.

2.3 Flexural waves in elastic plates

The theory of flexural waves in ice sheets follows to a large extent the theory of flexural waves valid for elastic plates in general. This theory was in large part developed by Horace Lamb in the late 19th century and the early 20th century. In 1889, Horace Lamb published a paper on the flexure of plane elastic plates consisting of uniform isotropic substance (Lamb, 1889). This paper was followed by another paper in 1917 which dealt specifically with wave propagation in infinite elastic plates in vacuum (Lamb, 1917), leading to the definition of so-called Lamb waves, which manifest themselves as surface waves in both symmetric and anti-symmetric solutions. The symmetric modes are usually termed the *longitudinal* modes because the average displacement is in the longitudinal direction, whereas for the antisymmetric modes, the average displacement is in the transverse direction, and these modes are generally termed *flexural* modes (Achenbach, 1984). For an illustration of the two modes, see figure 2.2.

The Lamb wave equations were derived by Lamb on the assumption of a sinusoidal wave with motion taking place in two dimensions x,y, the origin being taken in the median plane, and the axis of y normal to this (Lamb, 1917). Next we assume that the thickness of the plate is denoted by $2h$ and that the component of stress in the y direction at $y = \pm h$ is zero. By introducing the variable $\kappa = c_L/c_T$ where c_L represents longitudinal velocity

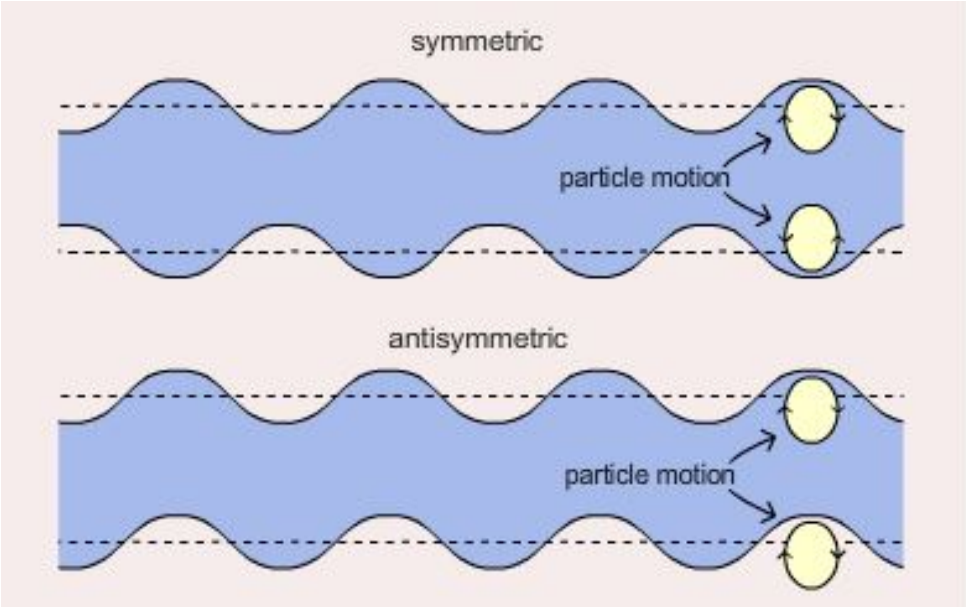

Figure 2.2: Symmetric and antisymmetric Lamb wave modes. It should be noted that for the symmetrical mode the particle displacement is primarily horizontal and for the antisymmetrical mode primarily vertical when the wavelength is small compared to plate thickness (which is the case for the flexural ice waves studied in this thesis).

and c_T represents transverse velocity, as well as introducing the dimensionless frequency Ω and the dimensionless wave number ξ by (Achenbach, 1984):

$$\Omega = \frac{2h\omega}{\pi c_\tau}, \quad \xi = \frac{2kh}{\pi}, \tag{2.18}$$

respectively, the longitudinal modes are described by (Achenbach, 1984):

$$\frac{\tan[\frac{1}{2}\pi(\Omega^2-\xi^2)^{1/2}]}{\tan[\frac{1}{2}\pi(\Omega^2/\kappa^2-\xi^2)^{1/2}]} = -\frac{4\xi^2(\Omega^2/\kappa^2-\xi^2)^{1/2}(\Omega^2-\xi^2)^{1/2}}{(\Omega^2-2\xi^2)^2}, \tag{2.19}$$

while the flexural modes are given by (Achenbach, 1984):

$$\frac{\tan[\frac{1}{2}\pi(\Omega^2-\xi^2)^{1/2}]}{\tan[\frac{1}{2}\pi(\Omega^2/\kappa^2-\xi^2)^{1/2}]} = -\frac{(\Omega^2-2\xi^2)^2}{4\xi^2(\Omega^2/\kappa^2-\xi^2)^{1/2}(\Omega^2-\xi^2)^{1/2}}. \tag{2.20}$$

These equations closely resemble the equations valid for wave modes in ice, and we will now investigate closer the flexural waves in ice sheets.

2.4 Flexural waves in ice sheets

In 1934 two articles regarding the propagation of elastic waves in ice were published (Ewing & Crary, 1934; Ewing et al., 1934). The first article is a study of the velocity of sound vibrations in ice as measured both by direct and resonance methods in the laboratory and on Saylor's Lake in Pennsylvania, USA. Through these experiments, P-velocities for longitudinal waves in a thin rod, a thin plate, and an infinitely extended solid were studied (Ewing et al., 1934). For a thin plate (which is assumed in the fluid-loaded thin plate theory which will be discussed later), the longitudinal wave velocity was found to be (Ewing et al., 1934):

$$v_L = \sqrt{\frac{Y}{\rho(1-\sigma^2)}}, \tag{2.21}$$

where Y is Young's Modulus, ρ is material density, and σ is the Poisson's ratio.

The second article deals specifically with the flexural waves registered on the seismograms from Saylor's Lake, and formulae for phase velocity and group velocity were derived based on thin plate theory as well as an empirical formula for group velocity:

$$V_g = 221(en)^{1/2}, \tag{2.22}$$

where e is thickness of the ice in feet, and n is frequency in Hz. Using the equations of motion of a thin plate and taking into account of gravity and depth of water to a rigid bottom (Oliver, Crary, & Cotell, 1954), Ewing and Crary (1934) found, for the phase velocity:

$$V_p^2 = (F/\lambda^2 + G\lambda^2)/(\rho + (D\lambda/\alpha)\coth(H\alpha/\lambda)),, \tag{2.23}$$

and for the group velocity:

$$U = c\left[1 + \frac{2(F - G\lambda^4)c_w^2\alpha^3\sinh^2(H\alpha/\lambda) + Dc^2c_w^2\lambda^3\alpha^2\sinh(H\alpha/\lambda)\cosh(H\alpha/\lambda) + H\alpha/\lambda}{2(F + G\lambda^4)c_w^2\alpha^3\sinh^2(H\alpha/\lambda) + Dc^4\lambda^3\sinh(H\alpha/\lambda)\cosh(H\alpha/\lambda) + H\alpha/\lambda}\right], \tag{2.24}$$

where

$F = \frac{1}{3}\pi^2e^2\rho V_p^2$

$G = g\rho_1/4\pi^2e$

$\alpha = (1 - c^2/c_w^2)^{1/2}$

$D = \rho_1/2\pi e$

$H = 2\pi h$

λ = wavelength in ice (in feet)

e = thickness of ice (in feet)

h = depth of water below the ice (in feet)

c_w = velocity of compressional waves in water (ft/s)

g = acceleration of gravity (ft/s^2)

ρ = density of ice

ρ_1 = density of water.

Press and Ewing (1951a) gives a more detailed and complete derivation of the phase and group velocity for large, intermediate, and small wavelengths compared to ice thickness. The derivations are for ice sheets floating on a body of water, and are based on Lamb (1917) and Osborne and Hart (1945) considering a plate in a liquid of infinite extent and considerably lower sound velocity than the compressional and shear waves in the plate. Press and Ewing (1951a) showed that flexural waves only occur when wavelengths are large compared to ice thickness. For wavelengths that are small compared to the thickness of the plate the symmetric and antisymmetric solutions reduce to Rayleigh waves which are transmitted along the surfaces.

As the solutions for large wavelengths derived in Press and Ewing (1951a) represents an intuitive understanding of the physics behind flexural waves in ice, as well as representing the classical derivation of the characteristic equations, the derivation is presented in its entirety in Appendix A. The period equation, based on the boundary conditions and initial conditions outlined in Appendix A, becomes

$$P[Q + \delta \cosh(\xi H)\cosh(\eta H) + Q[P + \delta \sinh(\xi H)\sinh(\eta H)] = 0, \tag{2.25}$$

where

$$\begin{aligned} \delta &= \rho_2 v_2^2(\eta^2 - k^2)(\zeta^2 - k^2)\xi/\rho_1\beta_1^2, \\ Q &= (\eta^2 + k^2)^2 \sinh(\xi H)\cosh(\eta H) - 4\xi\eta k^2 \cosh(\xi H)\sinh(\eta H), \\ P &= (\eta^2 + k^2)\cosh(\xi H)\sinh(\eta H) - 4\xi\eta k^2 \sinh(\xi H)\cosh(\eta H),, \end{aligned} \tag{2.26}$$

and

$$\begin{aligned} \xi^2 &= k^2(1 - c^2/\alpha_1^2), \\ \eta^2 &= k^2(1 - c^2/\beta_1^2,) \\ \zeta^2 &= k^2(1 - c^2/v_2^2). \end{aligned} \tag{2.27}$$

Here $2H$ is the ice thickness, ρ_1 is the density of the ice sheet, α_1 is the compressional velocity in the ice sheet, β_1 is the shear velocity in the ice sheet, ρ_2 is the water density, v_2 is the compressional wave velocity in water and $c = \omega/k$ as defined in equation 2.5.

If we now compare these equations to the characteristic Lamb equations (see 2.19 and 2.20), it can be seen that $P = 0$ and $Q = 0$ represents the symmetric and antisymmetric solutions for a plate in vacuum (Press & Ewing, 1951a). For a plate in a liquid, Osborne and Hart (1945) obtained the results $P + \delta \sinh(\xi H) \sinh(\eta H) = 0$ and $Q + \delta \cosh(\xi H) \cosh(\eta H) = 0$ for respectively the symmetric and antisymmetric solutions. Thus, we see that although the characteristic equations for the flexural waves in ice sheets overlying water are very similar to Lamb's equations, they can not be reduced to purely symmetric and antisymmetric modes.

2.5 Air-coupled flexural waves

In the equations reviewed in the previous section, it was assumed that the ice sheet is bounded by an infinite deep body of water below, and vacuum above. Press and Ewing (1951b) showed, however, that the presence of air above the ice sheet will, in the event of an explosion (such as a seismic source) in the air or on the ice sheet surface, generate a train of flexural waves with constant frequency preceeding the air wave (Hunkins, 1995). This wave train is referred to as *air-coupled flexural waves* (Press & Ewing, 1951b). The frequency of this train corresponds to the flexural wave frequency with phase velocity equal to the velocity of sound in the air. If a seismic source is used below the ice, however, the contribution from the air is negligible, and the wave train does not occur. The wave train preceeds the air wave and arrives over the time interval $\Delta t = x(1/v_g - 1/v_a)$ where x is distance to receiver, v_a is the velocity of sound in the air as well as the phase velocity of the frequency of the air-coupled flexural wave, and v_g is the corresponding group velocity (Oliver et al., 1954).

An example of how the air-coupled flexural waves appear in a seismogram obtained from Lansley et al. (1984) is included in figure 2.3

Due to the inherent mathematical complexity involved in modelling air-coupled flexural waves, no modelling of such waves has been attempted for this thesis. However, when

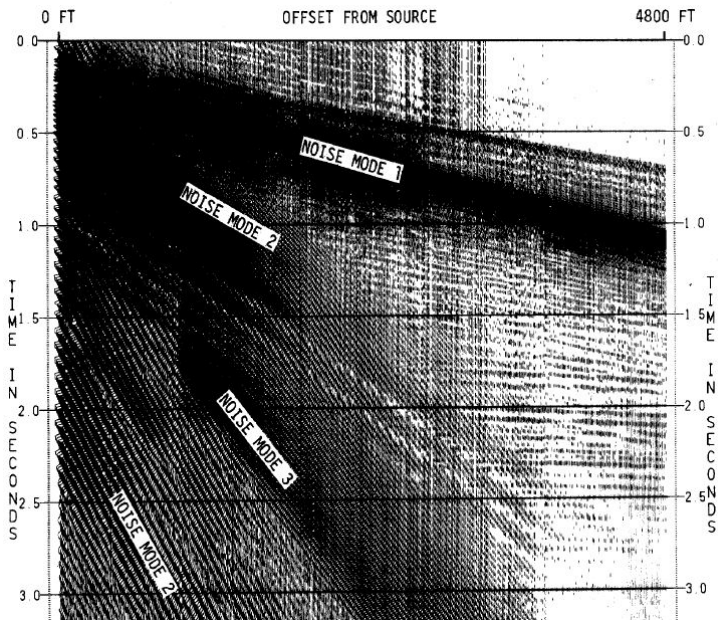

Figure 2.3: An example of flexural wave noise and air-coupled flexural waves obtained from Lansley et al. (1984). Here, noise mode 1 represents shear waves, noise mode 2 represents flexural waves, and noise mode 3 represents air-coupled flexural waves.

performing full waveform modelling, or when working on real seismic data, the presence of air-coupled flexural waves should be considered.

2.6 Flexural waves and fluid-loaded thin plate theory

Modelling of flexural wave dispersion based on fluid-loaded thin plate theory is presented in Yang and Giellis (1994) and Yang and Yates (1995). The first article is a thorough study of the dispersion relation, and the processing of, a real dataset obtained on Greeland during the spring of 1988 using a hammer blow as source (Yang & Giellis, 1994). The second article presents a derivation of the flexural particle displacement in the frequency domain, which can then easily be transformed to the $x-t$ domain via a 1-D inverse Fourier transform. As this procedure is easier to implement mathematically than the derivation outlined by Press and Ewing (1951a), and since the particle displacement in the $x-t$ domain can be calculated as well, this procedure was used in the modelling part of this thesis. In addition, unlike the derivation outlined by Press and Ewing (1951a) where a fixed Poisson's ratio of $\sigma = 0.25$ is assumed (see Appendix A), the procedure outlined

by Yang and Yates (1995) does not require such an assumption. Thus, this procedure allows for more accurate modelling in regards to how Poisson's ratio may change with temperature in the ice. As this procedure will be referred to frequently, it will now be outlined in its entirety. All material in the rest of this section is therefore obtained from Yang and Yates (1995).

A sketch showing the relevant wave displacement and boundary conditions for the fluid-loaded thin plate theory is included in figure 2.4. The principle behind thin plate the-

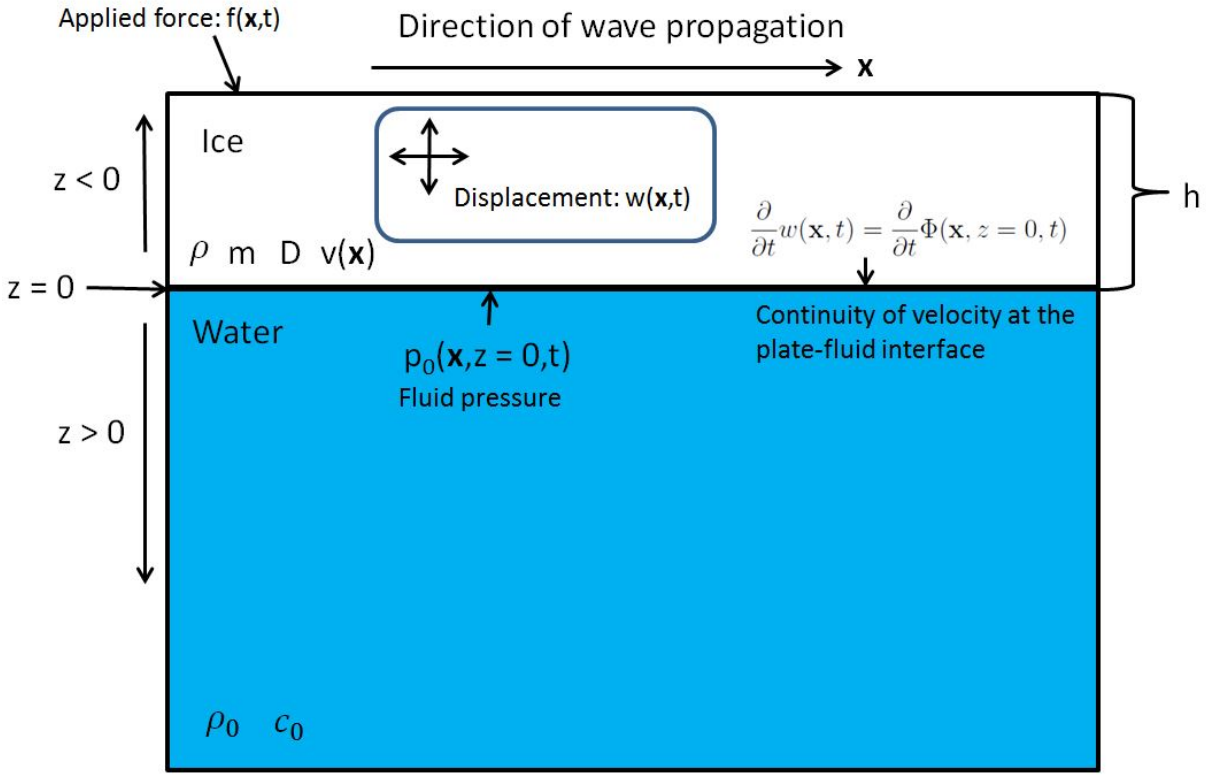

Figure 2.4: Sketch of the relevant displacements and boundary conditions for the procedure outlined in Yang and Yates (1995).

ory is that we consider a thin elastic plate (in our case the ice) with plate thickness $h <$wavelength at depth $z = 0$ lying over a compressible fluid with density ρ_0 and sound speed c_0 occupying the region $z > 0$ (in our case water). The plate then has a specific mass m and a bending stiffness D defined by

$$m = \rho h, \tag{2.28}$$

and

$$D = \frac{Yh^3}{12(1-\sigma^2)}. \tag{2.29}$$

The equation of motion when using a thin plate approximation is expressed as

$$D\nabla^4 w(\mathbf{x},t) + m\frac{\partial}{\partial t^2}w(\mathbf{x},t) = f(\mathbf{x},t) - p_0(\mathbf{x},z=0,t), \tag{2.30}$$

where w is plate deflection into the fluid. p_0 represents pressure in the fluid which satisfies the normal Helmholtz equation[2], f represents impulse type force, and $\mathbf{x}$ denotes the horizontal coordinates of the plate.

The boundary conditions take into account continuity of the velocity at the plate-fluid interface

$$\frac{\partial}{\partial t}w(\mathbf{x},t) = \frac{\partial}{\partial t}\Phi(\mathbf{x},z=0,t), \tag{2.31}$$

where Φ is the vertical displacement in the fluid, evaluated at the fluid-plate interface. Given an impulse force f, we further assume that the plate sits at rest before the force is applied, thus imposing the initial condition

$$w(\mathbf{x},t=0) = \frac{\partial}{\partial t}w(\mathbf{x},t=0) = 0. \tag{2.32}$$

In order to model flexural ice waves, we begin by solving the equation of motion in the frequency domain and then later perform an inverse Fourier transform to obtain the wave displacement in the time domain. Thus, first we express displacement, force, and pressure in terms of their Fourier components defined by:

$$\begin{aligned} w(\mathbf{x},t) &= \int e^{-i\omega t}W(\mathbf{x},\omega)\mathrm{d}\omega \\ f(\mathbf{x},t) &= \int e^{-i\omega t}F(\omega)\delta(\mathbf{x})\mathrm{d}\omega \\ p_0(\mathbf{x},z=0,t) &= \int e^{-i\omega t}P(\mathbf{x},z=0,\omega)\mathrm{d}\omega, \end{aligned} \tag{2.33}$$

where $\delta(\mathbf{x}) = \delta(x)$ for a line force at $x = 0$ and $\delta(\mathbf{x}) = \delta(r)/2\pi r$ for a point source at the origin where r denotes radial distance from the origin.

Assuming geophones which respond to particle velocity, the solution to the equation of

[2]The Helmholtz equation is defined as $\nabla^2 F + k^2 F = 0$ where $k = \omega/c$ (Pujol, 2003)

motion will also be expressed in terms of velocity which, at a fixed frequency, is related to the plate displacement by $v(\mathbf{x},\omega) = -i\omega w(\mathbf{x},\omega)$ (see equation 2.6). By substituting equation 2.33 into equation 2.30, we obtain the equation of motion:

$$D\nabla^4 v - m\omega^2 v = -i\omega[F(\omega)\delta(\mathbf{x}) - P(\mathbf{x}, z = 0)], \tag{2.34}$$

where the pressure field $P(\mathbf{x}, z)$ satisfies

$$\nabla^2 P + \frac{\partial^2}{\partial z^2} P + k_0^2 P = 0, \tag{2.35}$$

where $k_0 = \omega/c_0$ is the acoustic wave number for the water wave.

Further, the plate velocity is coupled to the surface pressure $P(\mathbf{x}, 0)$ by the boundary condition

$$v(\mathbf{x}) = \frac{1}{i\rho_0\omega}\frac{\partial P}{\partial z}(\mathbf{x}, 0), \tag{2.36}$$

where the right-hand side is the vertical velocity in the fluid at the surface expressed in terms of the pressure in the fluid and ρ_0 is the density of the fluid.

Equations 2.34 and 2.35 can be solved in the wave number domain, but a full derivation of this would be too comprehensive. The reader is referred to the references provided in Yang and Yates (1995) for more details. In order to obtain the spatial response of the plate as a function of frequency, the wave number solution is inverse Fourier transformed. This yields

$$v(x) = \frac{-i\omega F(\omega)}{2\pi D}\int \frac{\gamma e^{ikx}}{(k^4 - k_f^4)\gamma - \mu k_f^4} dk, \tag{2.37}$$

for a line force, and

$$v(r) = \frac{-i\omega F(\omega)}{2\pi D}\int \frac{\gamma J_0(kr)}{(k^4 - k_f^4)\gamma - \mu k_f^4} k dk, \tag{2.38}$$

for a point source. Here $J_0(kr)$ represents the Bessel function of zero order, k denotes the horizontal wave number, γ is defined by:

$$\begin{aligned} \gamma &= (k^2 - k_0^2)^{1/2}, \quad |k| > k_0 \\ \gamma &= -i(k_0^2 - k^2)^{1/2}, \quad |k| < k_0, \end{aligned} \tag{2.39}$$

and

$$\mu = \rho_0/m, \quad k_f = (m\omega^2/D)^{1/4}, \tag{2.40}$$

where k_f is the wave number for the flexural wave in a plate in vacuum.

For a line force the plate displacement is now given by the contour integral:

$$W(x) = \frac{F(\omega)}{2\pi D} \int_c \frac{\gamma e^{ikx}}{(k^4 - k_f^4)\gamma - \mu k_f^4} dk. \tag{2.41}$$

This expression yields the so-called free-wave and force-wave solutions. Free-wave solutions include standard sinusoidal waves, whereas forced waves are damped sinusoidal waves, such as external damping forces acting on the medium (Yang & Yates, 1995). In this case, only the free-wave solution is considered. The free-wave solution is obtained if the above integral is evaluated at the pole $k = k_1$, which corresponds to the real root of the denominator. One then obtains the relatively straight forward solution

$$W^0(x) = \frac{iF(\omega)}{D} \frac{\gamma}{d/dk[(k^4 - k_f^4)\gamma - \mu k_f^4]_{k=k_1}} e^{ik_1 x}, \tag{2.42}$$

which is a sinusoidal wave with wave number k_1. To obtain the flexural wave displacement in the $x-t$ domain, all one needs to do now is to insert the solution obtained by equation 2.42 into equation 2.33.

For a vertical point force, the plate response becomes

$$W(r) = \frac{F(\omega)}{2\pi D} \int \frac{\gamma H_0^{(1)}(kr)}{(k^4 - k_f^4)\gamma - \mu k_f^4} k dk, \tag{2.43}$$

where $H_0^1(kr)$ is the zeroth order Hankel function of the first kind. From this, one then obtains the free-wave solution

$$W^0(x) = \frac{iF(\omega)}{D} \frac{\gamma H_0^{(1)}(k_1 r)}{d/dk[(k^4 - k_f^4)\gamma - \mu k_f^4]_{k=k_1}}, \tag{2.44}$$

which is evaluated at the pole of the integral, $k = k_1$. As with the line source solution, the flexural wave displacement in the $x - t$ domain can now be found by inserting the solution of the above equation into equation 2.33.

More details regarding the implementation of these equations in the modelling is discussed in chapter 4. In addition, Appendix B presents an analytical derivation of formulae for

estimating the dispersion relation based on the equations presented above. As can be seen from the above derivation, this procedure for modelling flexural wave displacement has the great advantage of allowing us to model how dispersion and displacement changes with ice thickness and elastic parameters. Thus, in order to round off this chapter, a brief discussion regarding the theory behind how physical parameters such as ice temperature, ice salinity and ice thickness affect elastic parameters will be presented. This theory will then be utilized later in order to model several dispersion curves for flexural waves in ice sheets.

2.7 Physical parameters affecting dispersion relation of flexural waves in ice sheets

As can be seen from equations 2.28 and 2.29, important inputs for estimating the dispersion relation include the specific mass m and the bending stiffness, D. Both of these parameters are dependent on ice thickness, h, and the bending stiffness is also dependent on Young's Modulus, Y, and Poisson's ratio, σ, of the plate. Thus, it is clear that ice thickness and elastic parameters may influence the dispersion relation.

Cox and Weeks (1983) derive the following relationship:

$$\frac{V_b}{V} = \frac{\rho S_i}{F_1(T)}, \tag{2.45}$$

where V_b is the brine volume of a sample of sea ice, V is the bulk volume of the sample, ρ is the bulk density in $\mathrm{Mg/m^3}$, S_i is the salinity of the ice in parts per thousand, and $F_1(T)$ is a temperature dependent function defined as:

$$F_1(T) = \rho_b S_b (1 + k), \tag{2.46}$$

where ρ_b is the density of brine present, S_b is the salinity of brine present, and k is the ratio of the mass of salt in the solid and the mass of salt in the brine. All of these parameters are temperature dependent. The mass of the gas in the ice is assumed to be negligible (Cox & Weeks, 1983). Based on these relations, Cox and Weeks (1983) then estimate values values for $F_1(T)$ for a range of temperatures ranging from $-2°$ to $-30°$.

These values are presented in Table 2.1.

Cox and Weeks (1974) further estimates the following empirical relationship between ice salinity (in parts per thousand) and ice thickness based on several real-world surveys at various places in North America:

$$\begin{aligned} S_i &= 14.24 - 19.39h, \quad h \leq 0.4 \text{ m} \\ S_i &= 7.88 - 1.59h, \quad h > 0.4 \text{ m}, \end{aligned} \tag{2.47}$$

where h represents ice thickness. For a given input thickness, the corresponding salinity value may then be estimated and used as input in equation 2.45.

Based on a least-squares analysis of empirical observations from data collected at Greenland, Langleben and Pounder (1963) also estimates that Young's Modulus is related to the volume fraction of brine content in first-year sea ice through the relationship:

$$Y = 10 - 0.0351 v_b \quad (\text{GPa}), \tag{2.48}$$

where v_b represents the volume fraction of brine content in parts per thousand. From this, for a given temperature, we can use table 2.1 to estimate $F_1(T)$ (using simple interpolation if the temperature falls between two temperature values in the table). We can then, for a given salinity and bulk density, calculate how the fraction of brine content changes with temperature, and from this we can estimate Young's Modulus via equation 2.48. Finally, we can use this value as input in equations 2.29 to predict how the dispersion relation is affected through equations 2.42 and 2.44.

Furthermore, Weeks and Assur (2009) proposes the following empirical equation for how Poisson's ratio varies with sea ice temperature:

$$\sigma = 0.333 + 0.06105 \exp(T/5.48), \tag{2.49}$$

where T is given in °C. Thus, using this relation, we can also estimate the Poisson's ratio used as input in equation 2.29 for any given temperature.

Another empirical formula may also be used to calculate ice density as a function of

T(°C)	F_1(T)(Mg/m^3)
-2	38.731
-4	74.662
-6	107.876
-8	139.441
-10	167.865
-12	192.378
-14	214.143
-16	234.033
-18	253.588
-20	274.074
-22	294.496
-24	412.236
-26	638.433
-28	852.171
-30	1032.102

Table 2.1: Values for $F_1(T)$ at different temperatures (from Cox and Weeks (1983))

temperature (Pounder, 1965):

$$\rho_{ice}(\mathrm{Mg/m^3}) = 0.917 - 1.403 \cdot 10^{-4}\mathrm{T(^\circ C)}. \tag{2.50}$$

It should, finally, be noted that the temperature effects on Poisson's ratio are quite small. Studies of seismic data acquired from ice sheets on Greenland and Antarctica, for instance, found no apparent relationship between Poisson's ratio and temperature for temperatures below -10°C (Kohnen, 1974). As such, the use of empirical relations always carries a certain degree of uncertainty.

In addition to the sources referred to in this section, more information on ice mechanics may be found in Mellor (1983) and Timco and Weeks (2010).

This concludes the presentation of the theory behind dispersive waves and flexural ice wave dispersion. More details regarding the actual implementation of the theory will be presented in later chapters.

2.8 Summary: flexural waves in ice sheets

In this chapter a general overview of wave dispersion and the relevant characteristic equations for the antisymmetric flexural ice waves has been presented. As this chapter has illustrated, flexural ice wave dispersion may be modelled via different approaches, but the fluid-loaded thin plate theory as outlined in Yang and Yates (1995) provides a solid framework for estimating both flexural wave dispersion as well as wave displacement in the time domain. Finally, this chapter has outlined how physical parameters such as ice temperature, ice salinity and ice thickness may affect flexural wave dispersion via various, primarily empirical, relations.

Chapter 3

Processing flexural ice waves

As mentioned in the Introduction chapter, flexural wave noise is a common problem on seismic data acquired on ice sheets in the transition-zone between ice frozen to the ground and deep sea. There are various operational procedures which may reduce the problem. For instance, flexural waves tend to be greatly reduced if a seismic source submerged below the ice is used to generate source signatures, or if OBS receivers are used instead of conventional geophones located on the top of the ice sheet (Rendleman & Levin, 1990). Another procedure which works to lessen the flexural wave noise involves reducing the physical rigidity of the ice sheet itself, as it is expressed through equation 2.29. Proubasta (1985) outlines how a so-called Ice Saw may be used for this purpose. The Ice Saw features a huge saw mounted on a vehicle which is then used to cut large fractures in the sea ice. However, from an operational standpoint, both of these procedures involve higher costs and more time-consuming labour. The Ice Saw approach also involves several challenges from a Health, Safety and Environment (HSE) perspective. As a result, methods for successful processing of flexural wave noise that keep signals intact are greatly desired.

This chapter presents the theory behind three main techniques that are used for reducing flexural wave noise. A brief review of alternative methods will be given as well.

3.1 The $f-k$ transform

Combining the temporal and spatial Fourier transform into a 2-D Fourier transform allows us to map a signal, or a seismic image, as a function of both frequency and wave number. This is referred to the $f-k$ transform, and, mathematically it is defined as follows for a

given input signal, $f(x,t)$ (Mæland, 2005):

$$F(k_x,\omega) = \int\int_{-\infty}^{\infty} f(x,t)e^{-i(\omega t - xk_x)}dtdx, \quad f(x,t) = \frac{1}{4\pi}\int\int_{-\infty}^{\infty} F(k_x,\omega)e^{i(\omega t - xk_x)}d\omega dk_x. \tag{3.1}$$

From this equation it can be derived that straight lines in the $x-t$ domain transform into straight lines in the $f-k$ domain (Austegard & Rondenay, 2013). To illustrate: a plane wave with wavelength λ approaching the surface with angle of incidence α will appear to be propagating along the surface with the wavelength $\lambda_x = \lambda/\sin\alpha$ (Figure 3.1). From this it follows that the apparent velocity of the plane wave at the surface is

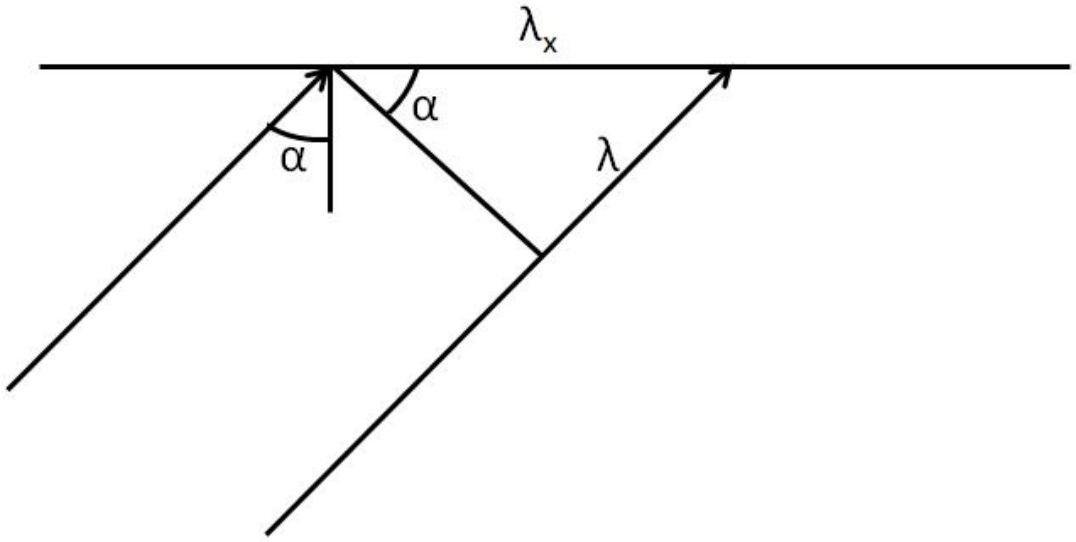

Figure 3.1: Apparent wavelength λ_x for a plane wave approaching a surface with angle of incidence α. Figure is based on illustration in Austegard and Rondenay (2013).

given by $c_x = \lambda_x f$. Applying the $f-k$ transform, we see that a straight line in the $x-t$ domain has a slope $1/c_x = k_x/f$, where $k_x = 1/\lambda_x$. Thus, all lines with slope $1/c_x$ in the $x-t$ domain will map as lines $f = c_x k_x$ with slope c_x in the $f-k$ domain (Austegard & Rondenay, 2013). As such, the $f-k$ domain can be very efficient in filtering linear coherent noise. The process involves taking the $f-k$ transform of a seismogram, remove linear coherent noise in the $f-k$ domain, and then apply a reverse $f-k$ transform back to the $x-t$ domain. This procedure is illustrated in figure 3.2. It should at this point be noted that as the flexural wave noise is dispersive, velocity is dependent on frequency, and, thus, the dispersion relation will not be linear in the $f-k$ domain for dispersive waves. Several examples of this will be presented later.

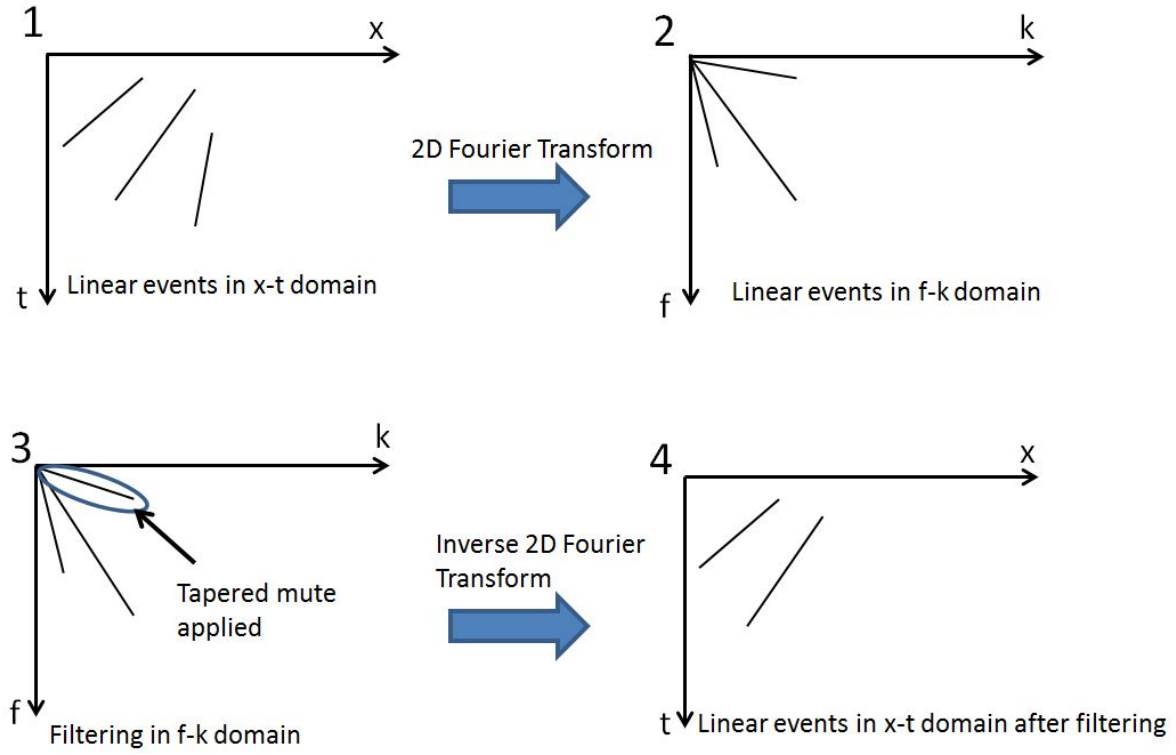

Figure 3.2: Illustration of filtering in the $f-k$ domain. Linear events in the $x-t$ domain (1) are mapped to linear events in the $f-k$ domain (2). One of the linear events is muted (3) and after transforming the data back to the $x-t$ domain, the event has been removed (4).

For a real-world example of successful removal of flexural wave noise via the $f-k$ transform, see Sunwall, Speece, and Pekar (2012).

3.1.1 Aliasing in the $f-k$ domain

As a signal is transformed in both time and space when an $f-k$ transform is applied, the signal may be subject to both temporal and spatial aliasing. Aliasing occurs when a frequency component exceeds the temporal and/or spatial Nyquist frequencies, and it is spatial aliasing which, in particular, tends to be a problem in $f-k$ filtering.

In order to illustrate when spatial aliasing occurs, we can use a derivation outlined in Yilmaz (2001). We consider a dipping reflector with dip angle θ. Next, we consider a normal-incidence plane wave with a dominant period of T recorded at the surface with trace separation Δx. This is the zero-offset case where Δx represents CMP trace interval. An illustration of this is presented in Figure 3.3.

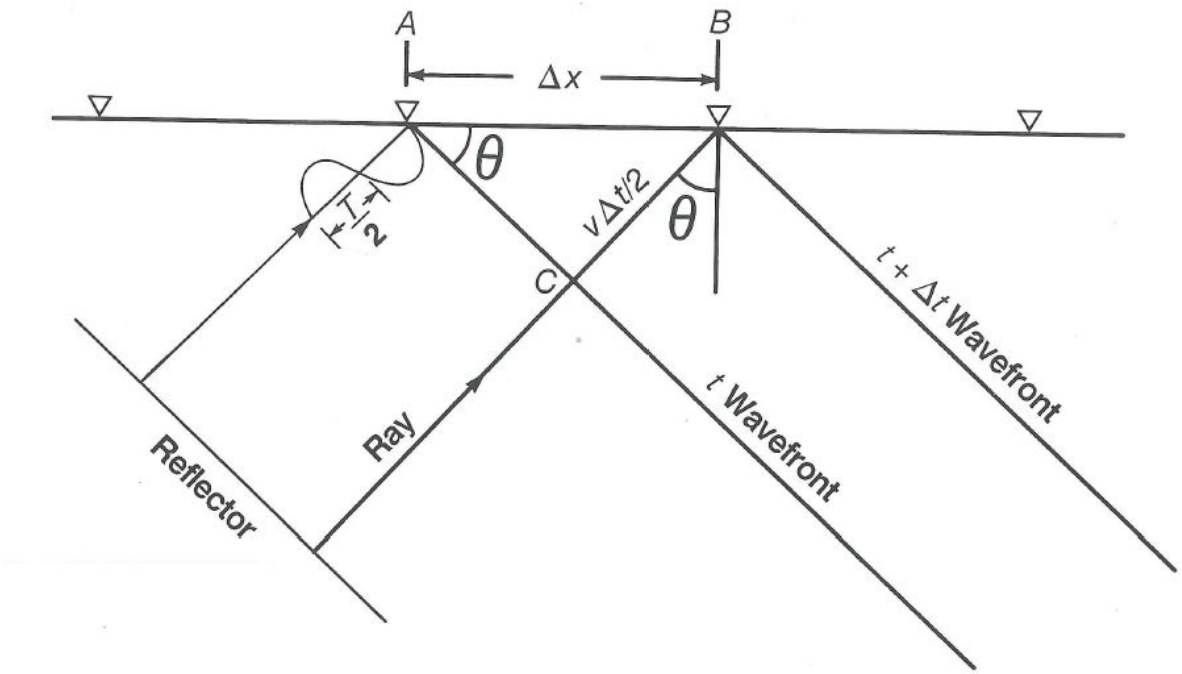

Figure 3.3: A plane wave reflecting at normal incidence from a dipping reflector with dip angle θ arriving at two consecutive receiver locations A and B at the surface with a separation equal to Δx. Illustration is obtained from Yilmaz (2001).

From the geometry of the scenario in figure 3.3, we see that we have

$$\sin\theta = \frac{v\Delta t}{2\Delta x}, \tag{3.2}$$

where Δt is the two-way time separation between the arrival times of the wave at receiver locations A and B, and v is the medium velocity (Yilmaz, 2001). Spatial aliasing occurs when the wavefront separation in time Δt is equal to half the dominant period T. If we view the geometrical figure in terms of wavefront distance, rather than reflector distance, and replace $v\Delta t/2$ (where t is two-way traveltime) with $v\Delta t$, we obtain, for $f_{max} = 1/T$:

$$f_{max} = \frac{v}{2\Delta x \sin\theta}. \tag{3.3}$$

Any frequency component higher than f_{max} will be aliased and folded back to a lower frequency. As flexural waves often propagate with low velocities, f_{max} may be quite low, and, thus, spatial aliasing is a common problem when attempting to use $f-k$ filtering on seismic data containing a broad fan of flexural wave noise. In addition, the Nyquist wave number, given by $k_{max} = 1/(2\Delta x)$, also puts an upper limit on the permissible wave numbers, as any wave number component higher than this value will be aliased as well.

3.2 The $\tau - p$ transform

The $\tau - p$, or slant-stack, transform involves a mapping from the $x - t$ domain to the so-called $\tau - p$-domain. τ is defined as the t-intercept time, or through the linear moveout correction

$$\tau = t - px, \tag{3.4}$$

where p is the ray parameter, or horizontal slowness, defined by $p = \sin\theta/v$, x is the offset, t is the two-way traveltime, and v is medium velocity (Yilmaz, 2001). After applying equation 3.4 to the data, the data are summed over the offset axis by:

$$s(p, \tau) = \sum_x p(x, \tau + px), \tag{3.5}$$

where $p(x, t)$ represents the input seismic dataset. By repeating the linear moveout correction defined in equation 3.4 for a range of p values and performing the summation defined in equation 3.5, a complete $\tau - p$, or slant-stack, gather is constructed (Yilmaz, 2001). The inverse $\tau - p$ transform is similarly done by first defining the inverse linear moveout correction

$$t = \tau + px, \tag{3.6}$$

followed by a summation in the $\tau - p$ domain over the ray parameter p axis to obtain:

$$p(x, t) = \sum_p s(p, t - px). \tag{3.7}$$

Either the forward or inverse transform must also be convolved with a so-called $\rho-$ filter in order to retrieve the initial waveform. Alternatively, one may perform a plane wave decomposition in the frequency domain where each amplitude component is estimated via a least-squares method. Mathematically this alternative approach involves multiplying the data with a generalized inverse matrix which replaces the $\rho-$ filter operation. For a continuous signal, such a filter may be applied to the reverse transform through the following equation (Turner, 1990):

$$p(x, t) = \frac{1}{2\pi}\frac{\mathrm{d}}{\mathrm{d}t} H_t \left[\int_{-\infty}^{\infty} s(p, t - px)\mathrm{d}p \right], \tag{3.8}$$

where H_t is the Hilbert transform.

Through equation 3.5 it can be shown that a hyperbola in a CMP gather will map to an ellipse in the $\tau - p$ domain, while a linear event in the CMP gather will map to a point in the $\tau - p$ domain. Thus, various events may separate in the $\tau - p$ domain so that effective filtering may be performed. Multiples in a horizontally layered medium will, for instance, plot at the same p-value, but the τ-values will change for each multiple. An example of how filtering may be performed in the $\tau - p$ domain is included in Figure 3.4.

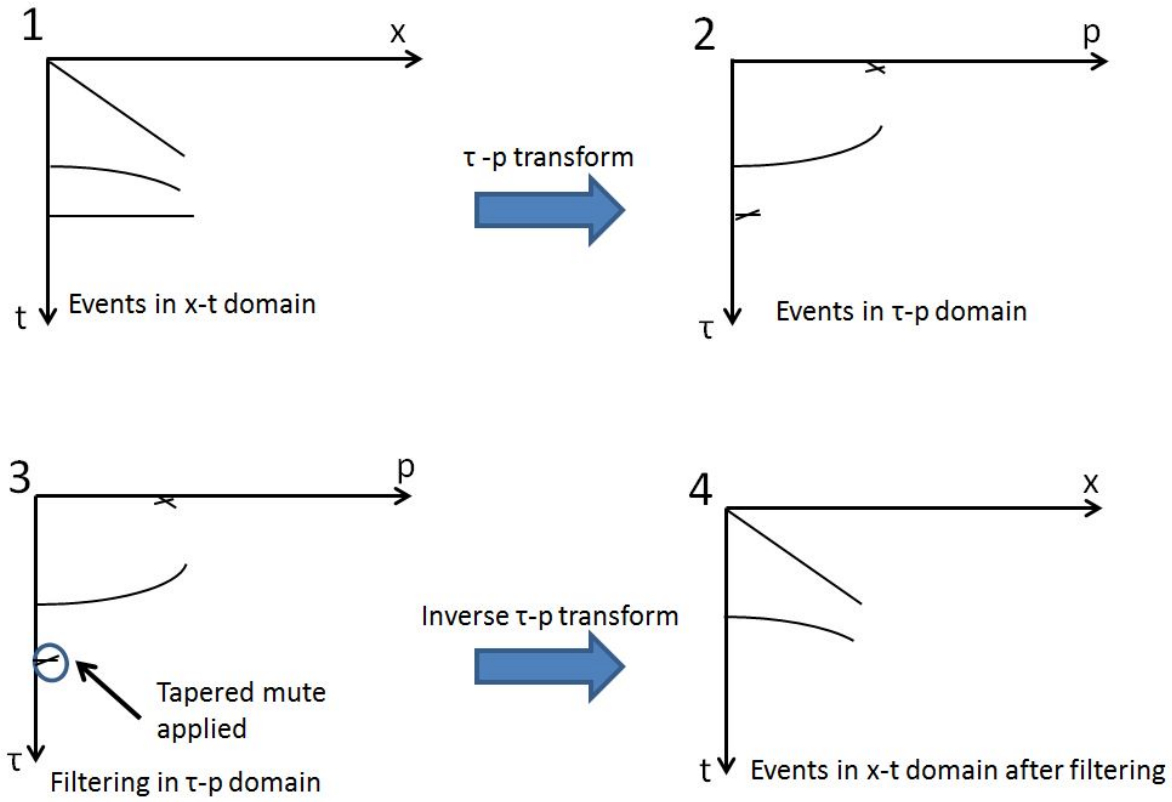

Figure 3.4: Illustration of filtering in the $\tau - p$ domain. Events in the $x - t$ domain (1) are mapped to the $\tau - p$ domain (2). One of the linear events from the $x - t$ domain is muted (3) and after transforming the data back to the $x - t$ domain, the event has been removed (4).

From this we can infer that if we know the velocity interval of the flexural ice waves, we can effectively mute the waves by removing all events within the related slowness interval in the $\tau - p$ domain as long as reflected events fall outside the interval. This approach is also described in Turner (1990) where it is stated that it is common to reject all data $|p| > |p\prime|$ where $|p\prime|$ is a p value smaller than that of the rejected noise. The $\tau - p$ transform, although computationally intensive, has also been proven successful in processing 3-D

datasets (see for instance Basak, Rana, Rao, Gangaiah, and Chandrasekaran (2012)) due to its efficiency in separating events located in separate slowness intervals. If reflected signals and flexural ice wave noise both fall within the same slowness intervals, however, filtering becomes more challenging and more care has to be done in order to identify signal and noise in the $\tau - p$ domain.

One final point to be made is that the $\tau - p$ transform, and it inverse, may also be calculated via the frequency-domain. Such an approach was used to perform $\tau - p$ transforms on datasets used in this thesis. Appendix C outlines the mathematics behind this approach.

3.2.1 Aliasing in the $\tau - p$ domain

One of the biggest challenges involved in $\tau - p$ filtering involves aliasing effects due to undersampling of p-values. In order to derive an appropriate sampling interval, we can use an example from Gardner and Lu (1991).

We assume the seismic data to be a single frequency sinusoid with frequency f Hz and no dip. Then $p(x,t) = \exp(2\pi i f t)$. Let x range from $-N\Delta x$ to $N\Delta x$. We then have $2N+1$ identical traces separated with spacing Δx. From equation 3.5 we then obtain

$$s(p,\tau) = \sum_{\alpha=-N}^{N} \exp[2\pi i f(\tau + p\Delta x\alpha)], \tag{3.9}$$

which can be analytically found to be

$$s(p,\tau) = \frac{\sin(2N+1)[\pi f p \Delta x]}{\sin[\pi f p \Delta x]} \exp[2\pi i f \tau]. \tag{3.10}$$

If we assume that we sample p at equal increments given by

$$dp = \frac{1}{(2N+1) f \Delta x}, \tag{3.11}$$

beginning with $p = 0$, then $S(p,\tau)$ is zero for all p except when both sine terms in equation 3.10 vanish, i.e., when

$$p = 0, \pm\frac{1}{f\Delta x}, \pm\frac{2}{f\Delta x}, \cdots \tag{3.12}$$

From this we see that if the data is regarded as a single-frequency horizontal "line", then

the $\tau - p$ transform is a single-frequency "point" at $p = 0$ with repetitions at multiples of $1/(f\Delta x)$. Thus, in order to recover the original data it is enough to use the $\tau - p$ transform around $p = 0$ and omit the repetitions. At frequency f we should therefore ideally restrict the range of p to less than $1/(f\Delta x)$, and from this we also see that in order to ensure proper sampling, the sampling increment, dp, should satisfy the inequality

$$dp < \frac{1}{f_{max}(2N+1)\Delta x}. \tag{3.13}$$

Since only one dp is used, the highest frequency in a given signal should therefore be used to evaluate dp (Gardner & Lu, 1991).

Further, spatial aliasing may also occur if there is insufficient sampling in the $x-t$ domain. From the Nyquist wave number, $k_{max} = 1/(2\Delta x)$, we see that in order to avoid spatial aliasing we must have:

$$\Delta x \leq 1/(2p_{max}f_{max}). \tag{3.14}$$

Often, however, this inequality will yield a very small geophone interval which is not practical in real-world surveys. Accordingly, spatial aliasing is often unavoidable, but this aliasing may be damped through the use of carefully designed notch-filters in the $f - p$ domain (Turner, 1990).

A final aliasing effect is caused by the fact that only finite regions of $\tau - p$ space is used, and the effect of this is to smear data in the $x-t$ domain after the inverse $\tau-p$ transform is performed (Turner, 1990).

3.3 The RT (radial trace) transform

The RT (radial trace) transform was first introduced to the field of seismic processing in Claerbout (1975). The transform has since been covered extensively by David C. Henley in a series of articles and conference abstracts (e.g. Henley (2003), Henley (2004), Henley (2006), Henley (2009)). Although the transform is rather simple from a mathematical point of view, it nevertheless remains an unconventional method, and it is not included in most seismic processing software packages (Henley, 2009). The method has, however, been proven quite successful in flexural wave noise processing (Henley, 2006), although

its efficiency is quite reduced on ice sheets with variable ice thickness (Del Molino et al., 2008).

The idea behind the RT transform is to map wavefield amplitudes to coordinates of velocity and traveltime. In other words, the transform involves a mapping along radial, or linear, traces in the $x-t$ domain to the $v-t$ domain, where v represents velocity (Henley, 2003). Noise events, in particular linear events, may then be isolated and attenuated with respect to the rest of the wavefield by applying simple single-trace operations in the RT-domain such as frequency-dependent filtering (low-pass, high-pass, band-pass) or relative time scaling. Mathematically, the method involves mapping the amplitudes of seismic traces $p(x,t)$, to the new coordinates, apparent velocity v and shifted two-way-traveltime t', via the transform:

$$\mathbf{R}[p(x,t)] = p'(v,t'), \tag{3.15}$$

with the inverse given by

$$\mathbf{R}^{-1}[p'(v,t')] = p(x,t), \tag{3.16}$$

where

$$t' = t - t_0, \quad v = \frac{x - x_0}{t - t_0}. \tag{3.17}$$

Here x_0 and t_0 are the coordinates of the RT transform origin which may or may not be set equal to the $x-t$ domain origin. An illustration of the mapping is included in Figure 3.5.

When trajectories are selected in the $x-t$ domain such that these encounter linear events in the domain, the trajectories are very nearly parallel to the linear event wavefronts. Thus, these events become low-frequency events in the corresponding RT-domain. Whether or not an event becomes stretched or compressed in the RT-domain depends upon the angle between the event wavefront on the $x-t$ panel and the intersecting RT-trajectory (Henley, 2003).

Regarding the use of the RT transform for removal of flexural wave noise, a procedure outlined in Henley (2006) has been proven quite successful. The idea is first to sample along a large fan of trajectories in the $x-t$ domain where flexural wave noise is present. The next step then is to take the Fourier transform of each RT domain trace. As each radial trace corresponds to one velocity value, one specific frequency component of the flexural ice wave noise will be captured along each trace due to the dispersive nature of

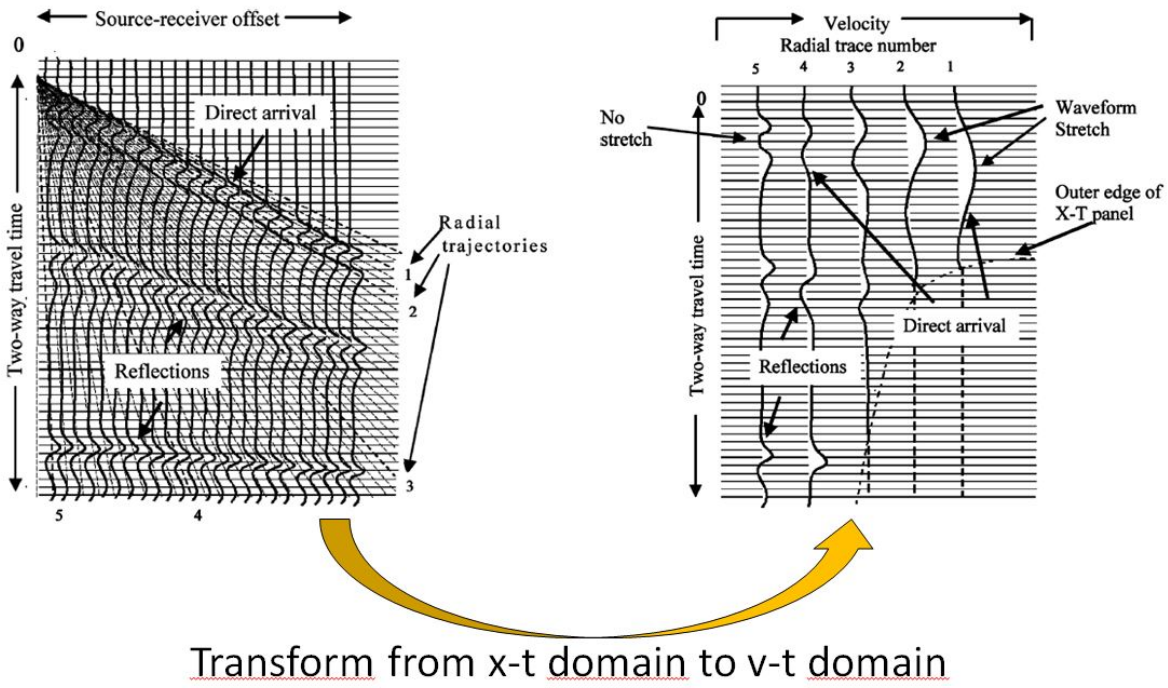

Figure 3.5: Example of RT transform. Five radial trajectories in the $x - t$ domain are mapped to the $v - t$, or RT, domain. We see from this that for instance radial trace 1, which encounters the linear, direct arrival in the $x - t$ domain nearly parallel to the wavefront, becomes a low-frequency event in the $v - t$ domain. Illustration is obtained from Henley (2003).

the flexural wave. As the flexural wave noise tends to have a larger magnitude than any signal captured along the trace, the Fourier spectrum of each radial trace will consist of the broad spectrum due to reflection energy as well as a few very narrow, high-amplitude peaks corresponding to the fundamental and harmonic flexural wave frequencies for that particular velocity. When sampling flexural wave noise along linear traces, the frequency component corresponding to the captured group velocity will be captured. A simple spectral clipping of these peaks may then be performed to edit away the flexural wave noise component. Finally, an inverse Fourier transform is performed followed by an inverse RT transform so that the signal is transformed back to the $x - t$ domain again (Henley, 2006). This procedure was applied to several datasets, and the results will be presented in Chapter 5. An illustration of the procedure is presented in Figure 3.6.

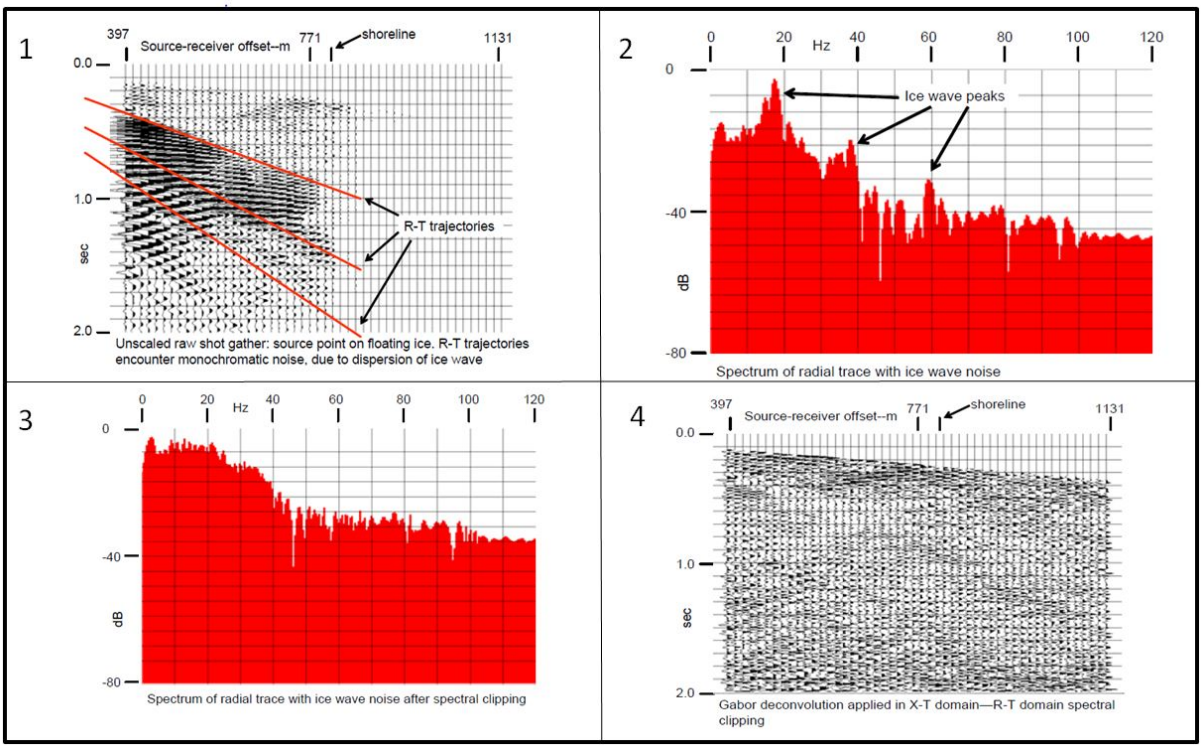

Figure 3.6: Procedure for flexural ice wave removal through use of the RT transform. The seismic data is first sampled along radial lines in the $x-t$ domain (1). Next, the Fourier transform is applied to the radial traces in the RT domain where the flexural ice wave is manifested as narrow peaks (2). Spectral clipping is then performed to remove the ice wave peaks (3). Finally, the data are transformed back to the $x-t$ domain where other processing techniques, such as deconvolution, may be performed to enhance the signal (4). Illustration is obtained from Henley (2006)

3.3.1 Aliasing in the RT domain

Aliasing can be a problem when performing the RT transform as the evenly spaced discrete sample points of a wavefield in one domain will map to unevenly spaced points in the other domain. Thus, in order to ensure a uniformly sampled RT wavefield, it is necessary to interpolate the corresponding uniformly sampled $x-t$ wavefield and vice versa in order to minimize aliasing (Henley, 2003).

As the radial trace trajectories diverge from a common origin in the $x-t$ plane, the wavefield tends to be oversampled in the $x-t$ domain near the RT origin while it tends to be undersampled at greater distances from the origin (Henley, 2003). As the time sample interval remains the same in both domains, temporal aliasing is not an issue. However, the RT domain velocity sample increment Δv controls spatial aliasing resulting from the transform. Thus, in order to avoid undersampling, every sample in the $x-t$ domain must

be represented by at least one sample in the $v-t$ domain (Henley, 2006).

Various interpolation methods may be used to achieve dense enough sampling in the $x-t$ domain, but the most common implementation is a simple one-dimensional interpolation along constant t-rows of the original dataset in the $x-t$ domain. This method only involves the two traces nearest the desired interpolation sample (Henley, 2009) As such, this interpolation algorithm is quite easy to implement, and a simple linear interpolation algorithm was also used for the RT transforms performed on the datasets processed in this study.

3.4 Other methods for flexural wave noise processing

A brief summary of other methods used for flexural wave noise processing will now be presented even though these methods have not been applied.

3.4.1 The Flexfil method

Beresford-Smith and Rango (1988) proposed a method for removing dispersive noise in the $x-t$ space referred to as the Flexfil method. The method is a prestack process involving three steps: (1) Trace-by-trace compression to collapse the noise to a narrow fan in $t-x$ space; (2) Muting of the noise in this narrow fan; (3) Inverse compression to recompress the reflection signals. The actual compression operator for the trace is based on spectral warping, which is a procedure involving a nonlinear scaling of the frequency axis defined mathematically by a compression of the spectrum of the trace with a function closely related to the dispersion characteristic of the noise:

$$W_t(\omega) = S_1[\Omega_1(\omega)]\Omega'(\omega). \tag{3.18}$$

Here $\Omega_1(\omega)$ is a scaled and translated version of the dispersion characteristic which is defined by $\omega = \Omega(k)$, where ω is angular frequency and k is the wave number. The phase velocity is given by $v_p = \Omega_1(\omega)/\omega$ and the group velocity is given by $v_g = \Omega_1'(\omega)$. Wavelet spreading, and not velocity spreading, is the criterion for noise discrimination as a seismic wavelet which propagates in a dispersive medium will increase in duration, and, hence, its

envelope will broaden. S_1 refers to the 1-D Fourier transform of a function, $s(x,t)$, with respect to t, where $s(x,t)$ represents a 1-D wave propagating with dispersion but without the effect of inelastic attenuation (Beresford-Smith & Rango, 1988).

The Flexfil method was efficient in increasing the signal-to-noise ratio with approximately 20 dB. For more details about the efficiency of the method, as well as the derivation of the mathematics behind it, the reader is referred to Beresford-Smith and Rango (1988).

3.4.2 Attenuation of flexural noise using geophones and hydrophones

Another method for flexural wave noise removal involves the use of geophones placed on top of the ice sheet and hydrophones located below the ice sheet. The method is outlined in Barr, Nyland, and Sitton (1993).

When the flexural ice wave passes a geophone and hydrophone pair, the ice layer will move in the vertical direction. The geophone then generates a voltage proportional to the velocity of the surface of the ice:

$$v(t) \propto \frac{\mathrm{d}z}{\mathrm{d}t}. \tag{3.19}$$

Here we assume that the geophone generates a positive voltage for v in the $+z$-direction, which represents vertical movement.

Because of the rigidity of the ice, the movement of the top and bottom of the ice sheet is identical. As such, the force applied to the water below causes the hydrostatic pressure in the water to vary about its steady-state value. As the force and resultant pressure applied by the ice to the water is proportional to mass times acceleration, the voltage generated by the hydrophone becomes:

$$p(t) \propto -\frac{\mathrm{d}^2 z}{\mathrm{d}t^2}. \tag{3.20}$$

Here, acceleration of the ice in the $-z$ direction causes an increase of hydrostatic pressure. The hydrophone is assumed to generate a positive voltage in response to that increase (Barr et al., 1993).

From equations 3.19 and 3.20 we obtain:

$$p(t) \propto -\frac{\mathrm{d}v(t)}{\mathrm{d}t}, \tag{3.21}$$

for the flexural ice wave.

For the reflection wave, however, the phase spectra of the hydrophone and geophone response show that the phase spectrum of the hydrophone signal leads that of the geophone signal by 90 degrees. Thus, the relationship between the two types of detection responses to a reflection can be expressed as:

$$p(t) \propto \frac{\mathrm{d}v(t)}{\mathrm{d}t}. \tag{3.22}$$

From this we see that the reflection wavelets from the two detectors can be made identical in both wave form and polarity by either differentiating the recorded geophone signal or integrating the hydrophone signal through the application of the Hilbert transform. Further, by doing this, the flexural wave noise will have the same wave form, but opposite polarity on the two resulting signals. Thus, if the resulting traces can be properly scaled and added, the reflection wavelets will add and the flexural wave noise will cancel (Barr et al., 1993).

The combination of geophones and hydrophones for flexural wave noise attenuation caused a 37 dB attenuation of the flexural ice wave. For more details about the efficiency of the method, the reader is referred to Barr et al. (1993). Implementation of this procedure is also discussed in Jensen (2015).

3.4.3 Flexural wave noise removal through seismic interferometry

Seismic interferometry estimates the detailed properties of the Earth through analyzing the interference patterns of seismic waves. The patterns are constructed through correlating and summing pairs of seismic traces with another to accurately image the elastic properties of the Earth (Schuster, 2010). The cross-correlation of the responses at two receivers will give the Green's function, or the Earth response, of the wave between these

receivers (Wapenaar, Dragaonv, Snieder, Campman, & Verdel, 2010).

To illustrate in a simple way how this method can be used for flexural ice wave processing, we consider a survey set up as shown in Figure 3.7. We assume that a seismic source is located on top of a floating ice sheet. Further, we assume that we have an OBS receiver located on the sea bottom, as well as a geophone placed on top of the ice. By cross-correlating the seismic traces obtained by the OBS receiver and the geophone, we obtain a new seismic trace where the apparent source position will be shifted to the OBS receiver. Thus, any signal and noise events occurring prior to the wave reaching the OBS receiver, including flexural ice wave noise, will be greatly reduced. Although very simplified here, this is nevertheless the principle concept behind seismic interferometry processing. Sampling issues, both temporal and spatial, as well as other processing techniques such as deconvolution, gain, etc., must, of course, also be considered in a more complicated real-world example. The example also illustrates that the method is difficult to implement if a combination of source and/or receiver locations is not possible when a survey is set up.

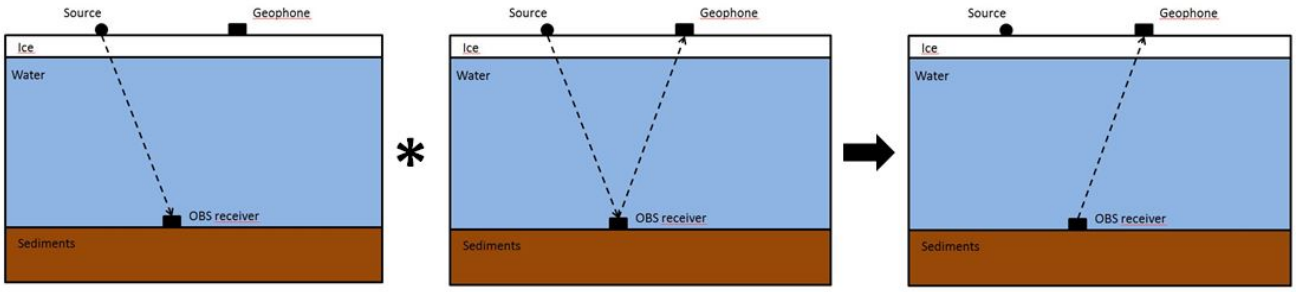

Figure 3.7: Simple example of the principle behind seismic interferometry. The trace obtained at the OBS receiver is cross-correlated with the trace obtained by the surface geophone. The resulting trace redatums the source location to the OBS receiver.

The seismic interferometry method was implemented in combination with singular value decomposition (SVD) dispersion analysis by Del Molino et al. (2011) for attenuating flexural ice wave noise. Seismic interferometry processing was applied to real seismic data obtained in Alaska, and significant improvement in the reflection signals resulted. For more details about the efficiency of the method, the reader is referred to Del Molino et al. (2011).

3.4.4 Brief mention of other processing methods

Other algorithms for flexural wave processing have been proposed in Soubaras (2001) and Del Molino et al. (2008). Since these do not contain detailed information, they will only be briefly mentioned below.

Soubaras (2001) outlines a method for dispersive noise attenuation for $P-S$ converted data. The method involves the extraction of noise in the $t-x$ region followed by the computation of a 2-D dispersive noise error filter. This filter is then applied in the $f-k$ domain to identify regions of dispersion noise. An optional deterministic attenuation of a signal $f-k$ region to be preserved may also be included. Finally, the dispersive noise is extracted from the data. The reader is referred to Soubaras (2001) for more details.

Del Molino et al. (2008) outlines how to solve for the characteristic equation of flexural ice waves analytically which yields the dispersion relation by using as a starting point the Lamb wave equations outlined in Viktorov (1967). Based on this, an algorithm which exploits the separability of correlated noise and signal with different bases in multiple domains is presented, although specific details about the algorithm is not included (Del Molino et al., 2008). In a follow-up article, Rovetta et al. (2009) outlines a more accurate characteristic equation for flexural ice waves which takes into account the specific interface model air/ice/water, and where complex transmission coefficients for P waves at the interfaces ice/air and ice/water as given by Müller (1985) are included.

3.5 Summary of flexural ice wave processing techniques

This chapter has outlined in detail the three main processing techniques utilized on the datasets relevant for this thesis. The $f-k$ and $\tau-p$ methods are both quite conventional methods, and all modern processing software contain functions for implementing these methods. The RT method, despite being quite simple to implement mathematically, remains a more unconventional method, but the method has been proven to be efficient in attenuating flexural ice wave noise on ice sheets with relatively constant ice thickness.

Of the other processing methods outlined in this chapter, only the seismic interferometry method can be considered to be conventionally applied. The other methods, although proven to work on various datasets, are not used to a great extent in seismic processing.

Chapter 4

Methods and datasets

This chapter presents the methods and datasets used for the modelling and processing work. The results will be presented in the subsequent chapter. All MATLAB programs not obtained from downloadable packages are listed in Appendix D.

4.1 Implementation of flexural ice wave modelling

Several of the real dataset used have been supplemented with synthetic flexural ice wave noise. Flexural ice waves were modelled based on the fluid-loaded thin plate theory of Yang and Yates (1995) as outlined in Section 2.6. Particular focus is on changes in the dispersion relation with varying ice temperature and ice thickness based on the theory outlined in Section 2.7.

MATLAB programs for modelling flexural ice waves generated by both a line source and a point source were developed. The program estimating line source generated flexural wave noise is based on equation 2.42 whereas the program estimating point source generated flexural ice wave noise is based on equation 2.44, which both are the frequency-domain solutions for the wave displacement.

In both cases, elastic parameters needed for equation 2.29 are first defined. A Young's Modulus of $Y = 8.7 \cdot 10^9$ Pa, which is a fairly common value for ice (*Appendix B - Useful quantities*, n.d.) [1], is assumed. Further, a Poisson's ratio of $\sigma = 0.31$, an ice density of 931 kg/m^3, and a water density of 1000 kg/m^3 are assumed. The user may input a desired

[1] This is not an Appendix for this thesis, but, rather, the title of a website from which the information was obtained. See References for more information.

ice thickness, and from this the specific mass (equation 2.28) is found. From the specific mass value we can further calculate the μ value in equation 2.40. Finally, the speed of sound in water is defined as $c_0 = 1482$ m/s.

In addition to ice thickness, the user may also input a receiver array (in meters), sampling time, T, and sampling interval, Δt - both in seconds. From this, frequency increments in the frequency domain as well as the Nyquist frequency may be calculated.

Next, a Ricker wavelet with a peak frequency equal to 50 Hz, as illustrated in figure 4.1, is by default assumed as source signature, although the user may input a different peak frequency when running the programs. The wavelet is generated via the program 'ricker.m', which is available on Mathwork's website [2]. Regarding the phase spectrum, we see that the phase is linear, but that slightly before 200 Hz, the gradient changes drastically. The reason for this is that the magnitude becomes negligibly small around this frequency, as can be seen from the amplitude spectrum. The Fourier transform of a signal is generally a complex function of the form $F(\omega) = G(\omega) + iH(\omega)$, where $G(\omega)$ is a sum of cosine functions, and $H(\omega)$ is a sum of sine functions. The phase is defined as $\phi = \tan^{-1}\left(\frac{G(\omega)}{H(\omega)}\right)$. Thus, as the magnitude becomes very small, $\frac{G(\omega)}{H(\omega)} \approx \frac{0}{0}$, and the phase starts behaving erratically (Smith, 2003).

Further, in order to accurately obtain a realistic time-domain displacement field, the geophone response must also be taken into account. A frequency-domain geophone response may be defined by (Brincker, Lagö, Andersen, and Ventura (2007)):

$$H = \frac{\omega^2}{\omega_0^2 + 2i\omega_0\omega\zeta - \omega^2}, \tag{4.1}$$

where ω is the angular frequency of the seismic input signal, ω_0 is the natural frequency of the geophone sensor, and ζ is the damping ratio. In this case, a natural frequency of 10 Hz and a damping ratio of 0.7 are assumed.

A 4th order Butterworth low-pass filter with a cut-off frequency of 100 Hz is then by default applied to the geophone response in order to remove unwanted high frequencies. The user may set a different cut-off frequency when running the programs. An illustration of the amplitude spectrum, phase spectrum, and time domain geophone response, when

[2]See http://www.mathworks.com/matlabcentral/fileexchange/30585-large-data-in-matlab–a-seismic-data-processing-case-study/content/migration/ricker.m

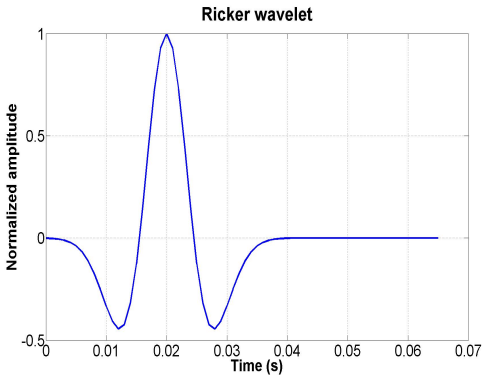

(a) Ricker wavelet

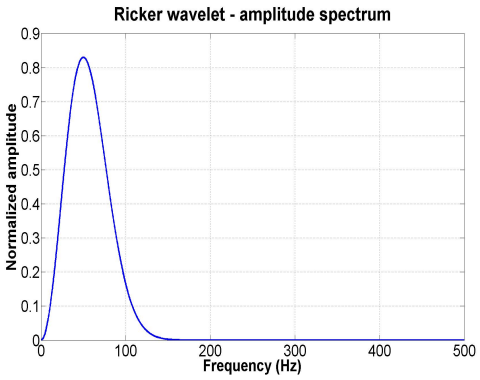

(b) Amplitude spectrum

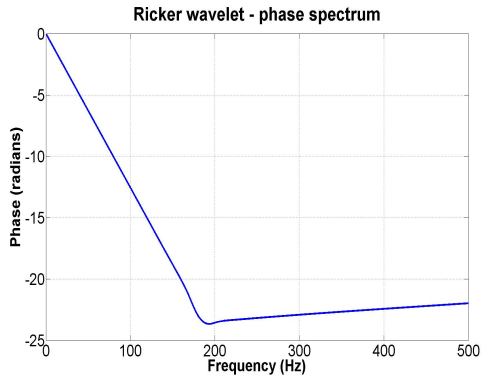

(c) Phase spectrum

Figure 4.1: Ricker wavelet used for modelling flexural ice waves.

a cut-off frequency of 100 Hz is applied, is presented in figure 4.2.

In order to implement equation 2.42 for a line source and equation 2.44 for a point source, we first have to find the real root of the denominator in equation 2.41. This was done analytically, and from the solution it is possible to generate the dispersion relation for both phase and group velocity as well as the frequency domain solution for the particle displacement (equations 2.42 and 2.44). Appendix B outlines the derivation of the analytical solution.

The term $F(\omega)$ in equations 2.42 and 2.44 is found through a simple multiplication of the amplitude spectrum of the source signature (see figure 4.1b) with the amplitude spectrum of the geophone response (see figure 4.2a). To calculate the zeroth order Hankel function of the first kind as it is needed in equation 2.44, MATLAB's in-built function 'besselh' is applied.

Finally, in order to obtain the wave displacement in the time-domain, solutions to equations 2.42 and 2.44 are subjected to inverse Fourier transforms as shown in equation 2.33.

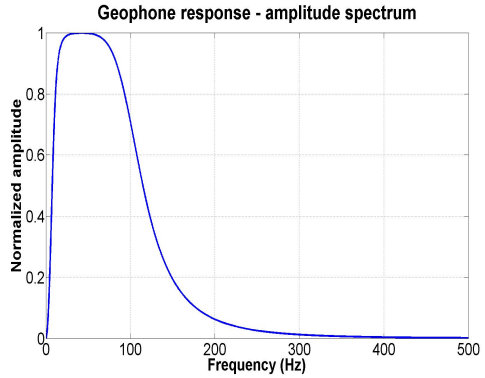

(a) Amplitude spectrum of geophone response

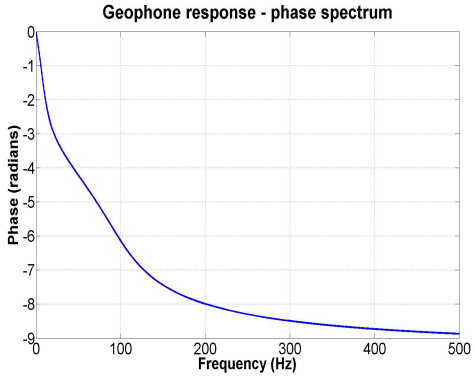

(b) Phase spectrum of geophone response.

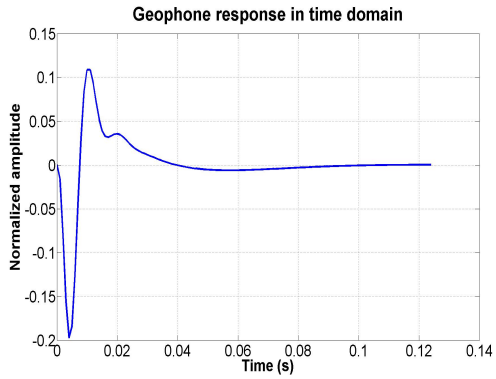

(c) Geophone response in time domain.

Figure 4.2: Response of geophone subjected to a 4th order Butterworth low-pass filter with cut-off frequency equal to 100 Hz.

In order to account for how dispersion changes with salinity, ice temperature and ice thickness, as outlined in Section 2.7, just small program modifications were needed. The program which estimates how dispersion changes with ice temperature plots how the dispersion relation of the flexural ice waves changes as the temperature decreases from -2°C to -30°C in increments of -2°C when the ice thickness is kept constant. First, when implementing equation 2.45 we fix a bulk mass of $M = 10^6$ Kg. Ice salinity is calculated via equation 2.47 based on the input ice thickness. In the event that we obtain a negative value for ice salinity, the salinity is set equal to 0 ppt. Rearranging equation 2.45 we obtain

$$V_b = \frac{MS_i}{F_1(T)}, \tag{4.2}$$

and using the information in table 2.1, we can now calculate V_b, the brine volume, as temperature varies from -2°C to -30°C.

Young's Modulus may next be calculated through equation 2.48, and this can now be used as input to equation 2.29. Further, via equation 2.49, we can calculate how Poisson's ratio changes with ice temperature, and via equation 2.50, we can calculate how ice density

changes with ice temperature.

In order to model how the dispersion relation changes with ice thickness, a separate program was written in which we assume a constant temperature of T = -2°C, and calculate Young's Modulus, Poisson's ratio and the density of ice using the formulae outlined above. Next, we assume that the ice thickness changes from 1 meter to 10 meters in increments of 1 meter. This is then used as input in equation 2.29, and we can then estimate how the dispersion relation is affected by changes in ice thickness.

The results of the modelling attempts are presented in the first part of Chapter 5.

4.2 Implementation of processing techniques

This section will present how various processing techniques relevant for this thesis were implemented in MATLAB.

For general reading and writing of SEG-Y files as well as plotting of seismograms, functions from the seismic processing package SeisLab 3.01 were used. This package is available for free download several places on the Internet, including `mathworks.com`.

In order to implement the classical $f-k$ transform, A MATLAB program, with subfunctions, was written. From the input parameters, the program transforms the data to the $f-k$ domain by performing a 2-D Fourier transform (equation 3.1). Next, the user may interactively select parts of the $f-k$ domain to mute. A subfunction then applies a tapering function along the edges of the specified mutes. This has been done through the use of a Blackmann-Harris window where the user may specify the length of the tapering window. Finally, once the user has muted selected parts of the image, an inverse 2-D Fourier transform is performed on the dataset so that it is transformed back to the $x-t$ domain, and the $f-k$ filtered seismogram is displayed. Amplitude and phase spectra prior to, and subsequent to, filtering are also plotted.

Implementation of the $\tau-p$ transform was also done via a MATLAB function developed for this thesis. Here the user may specify the slowness interval as part of the data input. The program calls upon a subfunction which performs a forward $\tau-p$ transform via the frequency domain (see Appendix C). This subfunction was initially obtained from Sacchi

(2002), but has been modified by Ruud(Senior Engineer, Department of Earth Science, University of Bergen) to allow for more flexibility in deciding upon the dp interval. Once transformed to the $\tau - p$ domain, the user may choose to perform spiking deconvolution of the data [3]. The spiking deconvolution is also done via the frequency domain as it is illustrated in Gonzalez, Woods, and Eddins (2004). Next, the user may mute parts of the $\tau - p$ spectrum, and, just as when muting is performed in the $f - k$-domain, a subfuction is called upon to taper along the edges of the selected mutes with a Blackmann-Harris window. Once muting has been performed, a reverse $\tau - p$ transform back to the $x - t$ domain is performed via another subfunction initially obtained from Sacchi (2002) and then later modified by Ruud. Amplitude and phase spectra prior to, and subsequent to, filtering are also plotted.

A final point to be made regarding the implementation of the $\tau - p$ transform is that the main program and its subfuctions take quite some time to run. Thus, the dp interval is, by default, set equal to $(p_{max} - p_{min})/N$ where N is the number of traces in the input data, even though this causes aliasing when inequality 3.13 is not fulfilled. This trade-off between potential aliasing effects and shorter computing time was justified in regards to the processing work performed for this thesis as it turned out that the aliasing effects were not severe enough to cause any major processing problems on most of the datasets.

For implementation of the RT transform, yet another MATLAB function was written. In addition to the input seismic data, time array, receiver array and dt, the user will also here input a velocity array containing a fan of radial traces that will be filtered. The origin of the radial traces is set equal to the origin of the seismogram. A simple linear interpolation of amplitude values is performed when a sample falls between two traces during radial trace sampling. Next, spectral clipping is performed as outlined in Henley (2006) and illustrated in figure 3.6. The threshold above which spectral clipping occurs is specified by the user as an input, and is equal to the input value times the median value

[3] As the $\tau - p$ transform is basically a plane-wave decomposition of the wavefield (Treitel, Gutowski, & Wagner, 1982), spiking deconvolution for source signature compression is usually more efficient in the $\tau - p$ domain than in the $x - t$ domain. It should, however, be noted that the $\tau - p$ transform performed in this program is a *conventional slant stack* which only yields an exact plane-wave decomposition when we deal with line sources. A so-called *proper slant stack* must be performed for an exact plane-wave decomposition of a point source (Yilmaz, 2001). A filter operator must then be convolved with the linear moveout applied wavefield before summation via equation 3.7. The operator will correct for 3-D effects by converting a points source generated wavefield into a line source generated wavefield. In terms of kinematics, however, the two slant stacking processes are equivalent. They differ only in their treatment of amplitudes (Yilmaz, 2001).

of the amplitude spectrum for any given trace. Amplitude values above this threshold are damped and set equal to the median value for the spectrum. An inverse RT transform is then performed back to the $x - t$ domain. Amplitude and phase spectra prior to, and subsequent to, filtering in both the $x - t$ domain and RT domain are also plotted. A note to be made in this case is that the spectral clipping technique applied here is rather crude, and that a future point of improvement could be to smooth the clipping to create a more continuous amplitude spectrum as illustrated in figure 3.6, image 3.

In the $x - t$ domain, several other programs were used to perform standard processing operations. One program may be used to obtain the power spectrum as a function of frequency and velocity. Even though the dispersion relation technically is defined as an equation, this spectrum may be used to interpret the dispersion. The program transforms the data to the $\tau - p$ domain so that interpolation in time is not necessary. The velocity array is found by simply taking the inverse of the slowness array, and a Fourier transform is then applied to each trace to obtain the power spectrum. For more information about procedures for interpreting the dispersion relation through such methods, see Tran, Nguyen, Sacchi, and Le (2014).

Another program was written to perform simple muting of unwanted events in the $x - t$ domain, and, as in the other muting-programs described above, a subfuncton is called upon to taper the edges of the muted parts with a Blackmann-Harris window.

For scaling in the $x - t$ domain, two separate programs were used. One program, written specifically for this thesis, compensates for energy loss due to geometrical spreading by multiplying each trace with the square root of the trace offset. In addition, to compensate for attenuation, each trace is multiplied by the factor $e^{0.001x}$, where x, again, is trace offset. The other program, which performs AGC-scaling, was obtained from the SeismicLab package developed by University of Alberta which can be downloaded at `http://seismic-lab.physics.ualberta.ca/`.

Predictive deconvolution for multiple removal was performed via another program obtained from the SeismicLab package. A small separate program was written to accommodate the SeismicLab program as the downloadable program only works for a single trace input. The program written specifically for the thesis enforces a loop which ensures that all seismic traces in a dataset are subjected to predictive deconvolution. In addition, all

NaN values are replaced with zero values.

Finally, velocity analysis, NMO-correction and stacking were performed by using the programs obtained from the SeismicLab package.

All MATLAB programs not obtained from the SeisLab 3.01 and SeismicLab packages are, as noted in the introduction to this chapter, listed in Appendix D.

4.3 Datasets

The datasets used in this thesis are all single shot gathers generated either synthetically or obtained from real surveys. Survey parameters for all shot gathers is presented in table 4.1 which lists minimum receiver offset, receiver interval, maximum receiver offset, recording time and sampling interval.

Dataset	Min. offset (m)	Interval (m)	Max. offset (m)	Rec. time (s)	Samp. interval (ms)
1	5	5	1500	4	1
2	5	5	1500	4	2
3	100	12.5	3087.5	4	2
4	25	6.25	768.75	0.5	1
5	21.25	6.25	765	8	1

Table 4.1: Overview of all shot gathers subjected to processing.

A brief presentation of all shot gathers will now be given.

4.3.1 Dataset 1: Simple synthetic shot gather with three reflectors

The first attempts of processing were performed on a very simple synthetic shot gather consisting of a model with three horizontal reflectors. We assume a 4-layer model defined through the thicknesses, velocities and densities presented in table 4.2.

The source signature is assumed to be a Ricker wavelet with peak frequency equal to 50 Hz. The wavelet and its amplitude and phase spectra are illustrated in figure 4.1.

Reflectors were modelled using seismic forward modelling based on the ray theory outlined

Layer	Thickness (m)	P-velocity (m/s)	S-velocity (m/s)	Density (kg/m^3)
1	300	1400	1000	2100
2	400	1700	1100	2200
3	500	2100	1400	2500
4	200	2400	1800	2600

Table 4.2: A simple 4-layer model assumed for Dataset 1.

in Krebes (2004). The reflection coefficients at each interface were calculated through the Zoeppritz equations as outlined in Auld (1990). To obtain the final seismogram, the reflection series calculated via the Zoeppritz equations were convolved with the seismic Ricker wavelet. The seismogram is presented in figure 4.3.

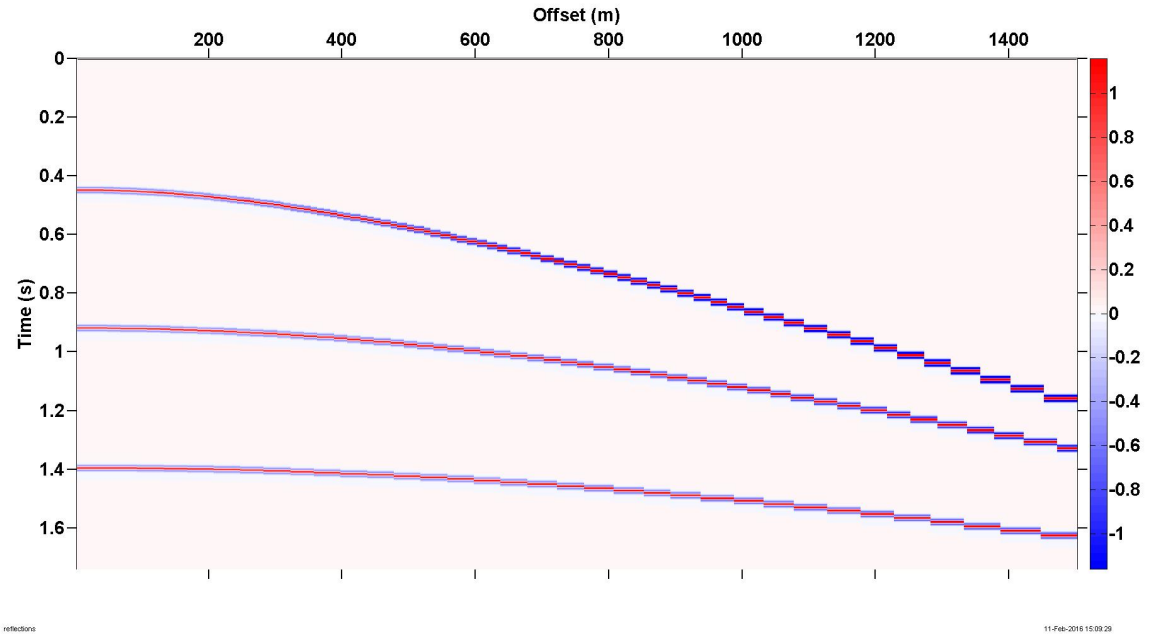

Figure 4.3: Seismogram - Dataset 1.

Note that in this case no correction for geometrical spreading or attenuation has been applied. Also, we notice that at far offsets, the seismogram does not appear very realistic in that the reflectors take the shape of steps rather than as continuous lines. This is probably due to inaccuracies when rounding off various numerical computations in the program. However, for the purposes of this seismogram, these inaccuracies are not very relevant as the purpose of the seismogram merely was to perform simple tests of how efficient the various processing techniques outlined in the previous chapter were at removing flexural ice wave noise while keeping the signals intact. Thus, flexural ice wave noise was

synthetically added to this seismogram from the procedure outlined in the previous section, and attempts were subsequently made to remove the flexural wave noise in order to retrieve the original signal. The scaled seismogram with added and flexural wave noise as generated by a line source is shown in figure 4.4. The efficiency of the various processing techniques in removing the flexural ice wave noise added to the dataset will be discussed further in Chapter 5. This dataset will from now on be referred to as **Dataset 1**.

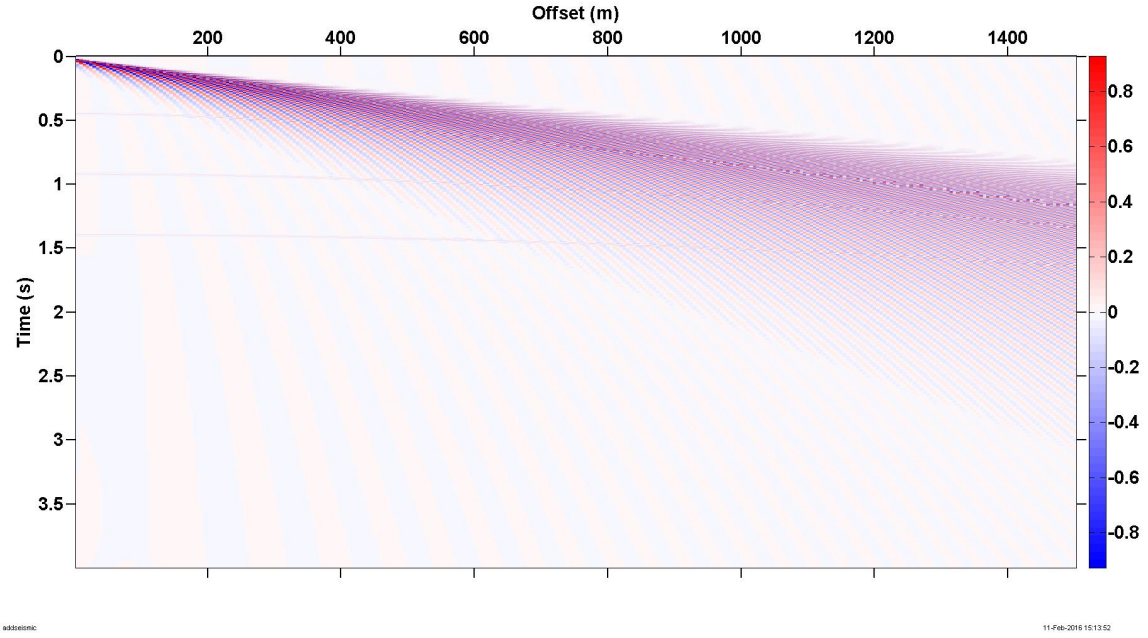

Figure 4.4: Dataset1: scaled seismogram featuring added synthetic flexural ice wave noise generated by a line source.

4.3.2 Dataset 2: Synthetic shot gather based on real marine survey at Van Mijenfjorden, Svalbard

The second shot gather subjected to processing is a full-waveform synthetic marine dataset with added synthetic flexural ice wave noise. The dataset has been generated with the software Nucleus (from PGS) through the use of the propagating matrix method as outlined in Krebes (2004), and is based on a real shot gather obtained at Van Mijenfjorden, Svalbard (the real dataset will be descried in the next subsection). The dataset is based on the subsurface model outlined in table 4.3. Survey parameters are presented in table 4.1.

Layer	Thickness (m)	P-velocity (m/s)	S-velocity (m/s)	Density (kg/m^3)
1	50	1480	0	1000
2	20	1750	500	1500
3	300	4000	2000	2500
4	500	4500	2250	2550
5	Infinite half space	5000	2500	2600

Table 4.3: Synthetic marine shot gather based on real survey at Van Mijenfjorden, Svalbard

A section of the seismogram, subjected to normalization, is presented in figure 4.5. From the figure we can identify reflectors, and we also notice the presence of several multiples. The same dataset with added synthetic flexural ice wave noise as generated by a point source is presented in figure 4.6. Processing of this dataset will be illustrated in Chapter 5. This dataset will from now on be referred to as **Dataset 2**.

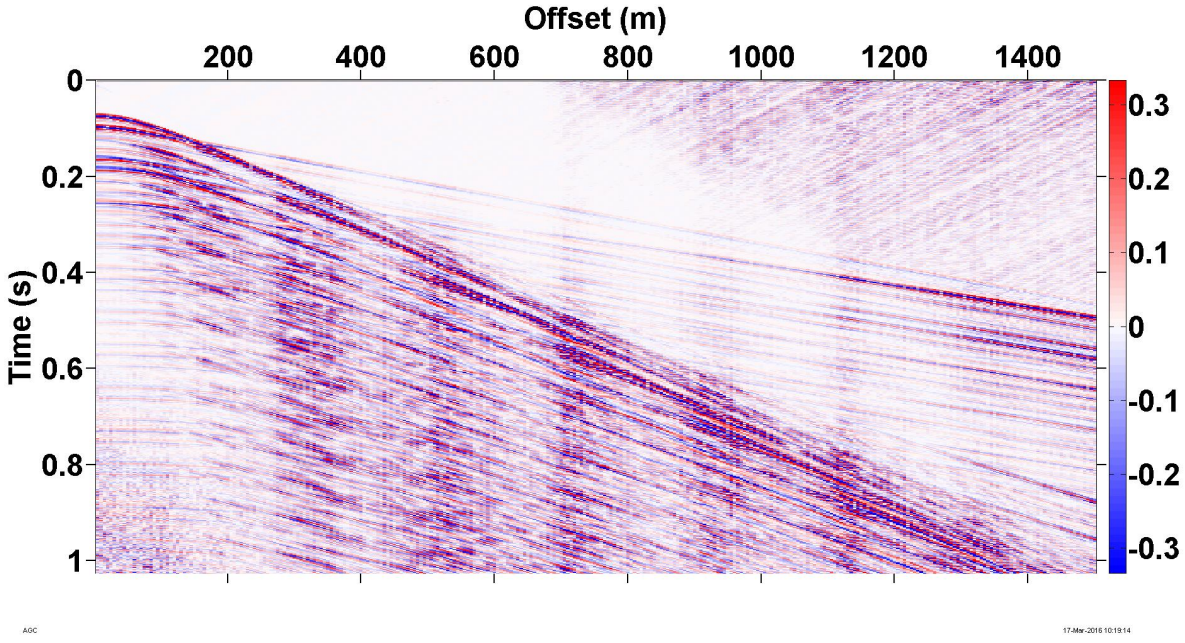

Figure 4.5: Section of full-waveform synthetic, normalized, shot gather generated from marine survey at Van Mijenfjorden, Svalbard.

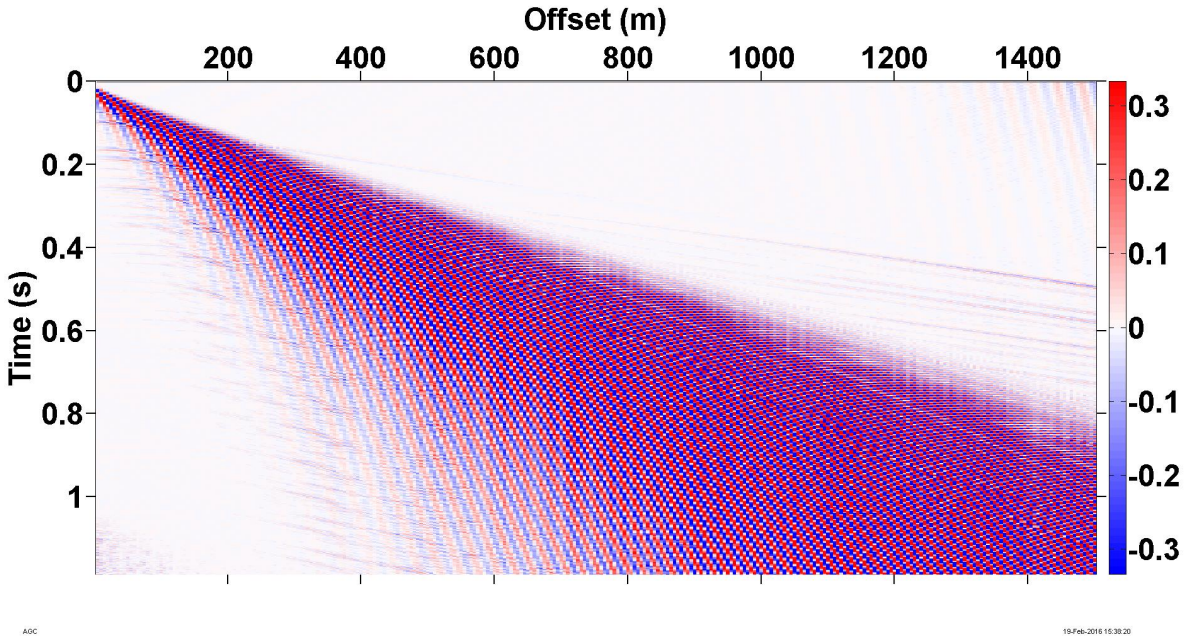

Figure 4.6: Section of full-waveform synthetic, normalized, shot gather generated from marine survey at Van Mijenfjorden, Svalbard with added synthetic flexural ice wave noise as generated by a point source.

4.3.3 Dataset 3: Real shot gather obtained from marine survey at Van Mijenfjorden, Svalbard

The third shot gather subjected to processing is a real dataset obtained during the Svalex course in 2012 at Van Mijenfjorden, Svalbard. This shot gather served as the model for the synthetic shot gather outlined in the previous subsection. The shot gather is obtained from shot 3421 from line VM-09-09 which is an airgun array shot consisting of four air guns deployed perpendicularly to the line direction. Survey parameters are presented in table 4.1. A map showing the source location and receiver line is presented in figure 4.7. A normalized section of the seismogram is presented in figure 4.8.

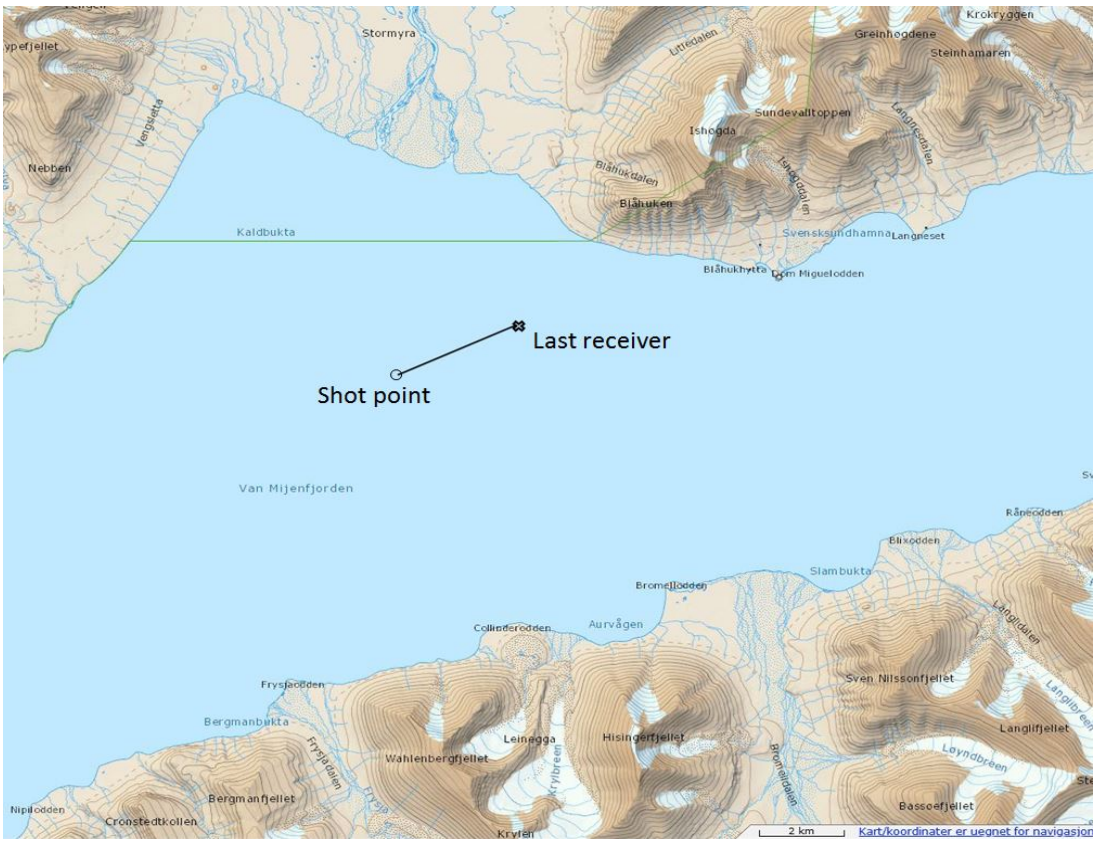

Figure 4.7: Map showing the location of shot point and receiver line for shot 3421 performed during Svalex 2012.

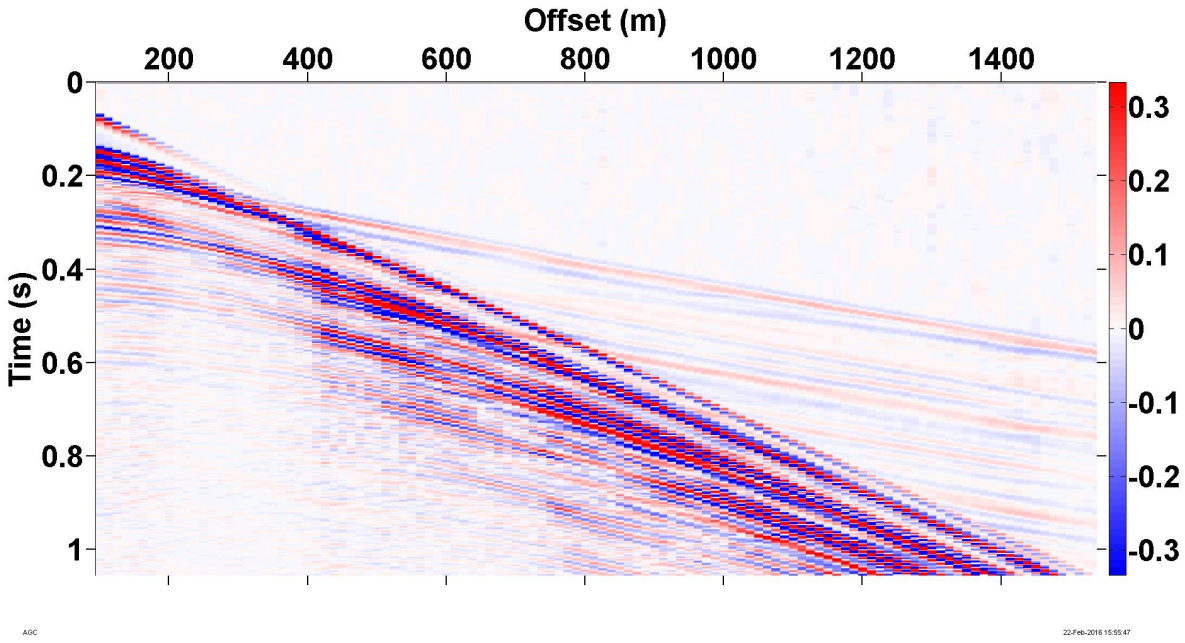

Figure 4.8: Section of real, normalized, shot gather retrieved from shot 3421 performed during Svalex 2012.

Being marine data, no flexural wave noise is present on the shot gather. Thus, in order to test the efficiency of processing methods in removing flexural ice wave noise, synthetic noise as simulated from a point source was added. The shot gather with added synthetic flexural ice wave noise is presented in figure 4.9. Processing of this dataset will be illustrated in Chapter 5. This dataset will from now on be referred to as **Dataset 3**.

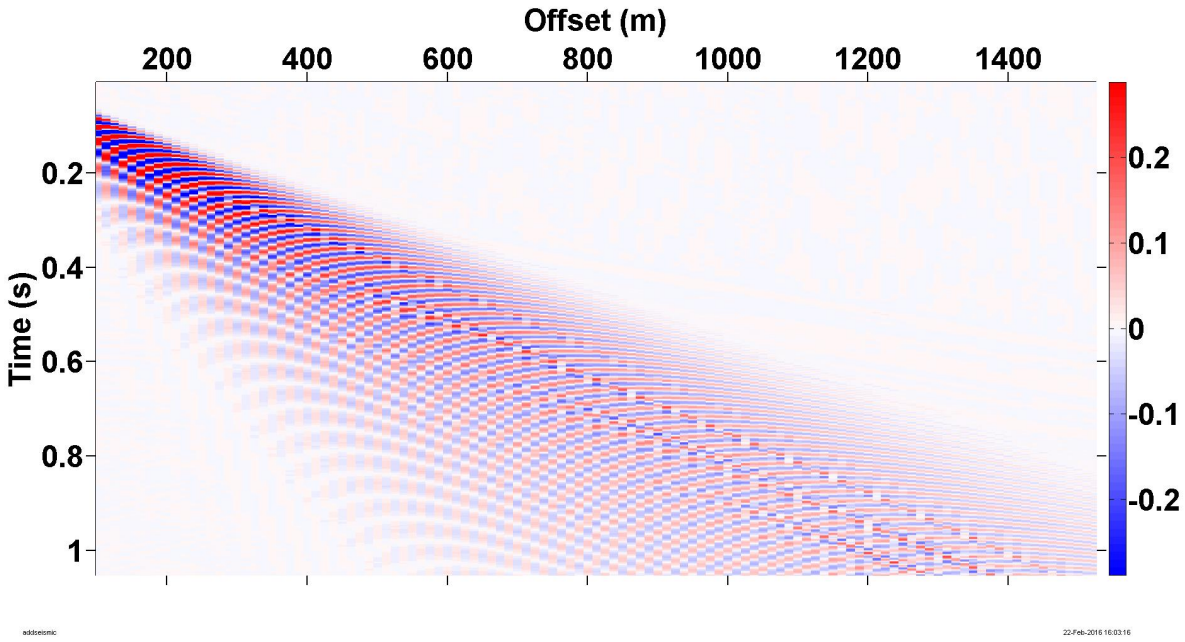

Figure 4.9: Section of real, normalized, shot gather retrieved from shot 3421 performed during Svalex 2012 with added synthetic flexural ice wave noise as modelled from a point source.

4.3.4 Dataset 4: Synthetic shot gather based on real survey on sea ice near Sveagruva, Svalbard

The fourth shot gather subjected to processing was generated by Postdoctoral researcher Martin Landschulze, Department of Earth Science, University of Bergen, based on a real survey performed in 2013 on sea ice near Sveagruva, Svalbard (the real dataset will be descried in the next subsection). The full-waveform synthetic dataset was generated through viscoelastic modelling solving the relevant differential equations with the finite-element method. At the upper and lower ice layer boundaries, a transition from the viscoelastic to the acoustic domain was assumed in order to simulate flexural-, air- and water-waves. In addition, a transition from the acoustic to the elastic domain was assumed

between the water and the seafloor. Outer boundary damping of waves leaving the model space helped avoiding unwanted simulation reflections. In the acoustic domain, plane wave radiation damping and cylindrical wave radiation damping were included, and in the viscoelastic domain plan radiation damping was included. Finally, the rigidity of the ice was included in order to simulate how movement of the ice sheet caused by the flexural waves will affect the water. Survey parameters are presented in table 4.1.

The seismogram, subjected to normalization, is presented in figure 4.10. Note the presence of flexural ice wave noise at low velocities. Processing of the dataset will be presented in Chapter 5. This dataset will from now on be referred to as **Dataset 4**.

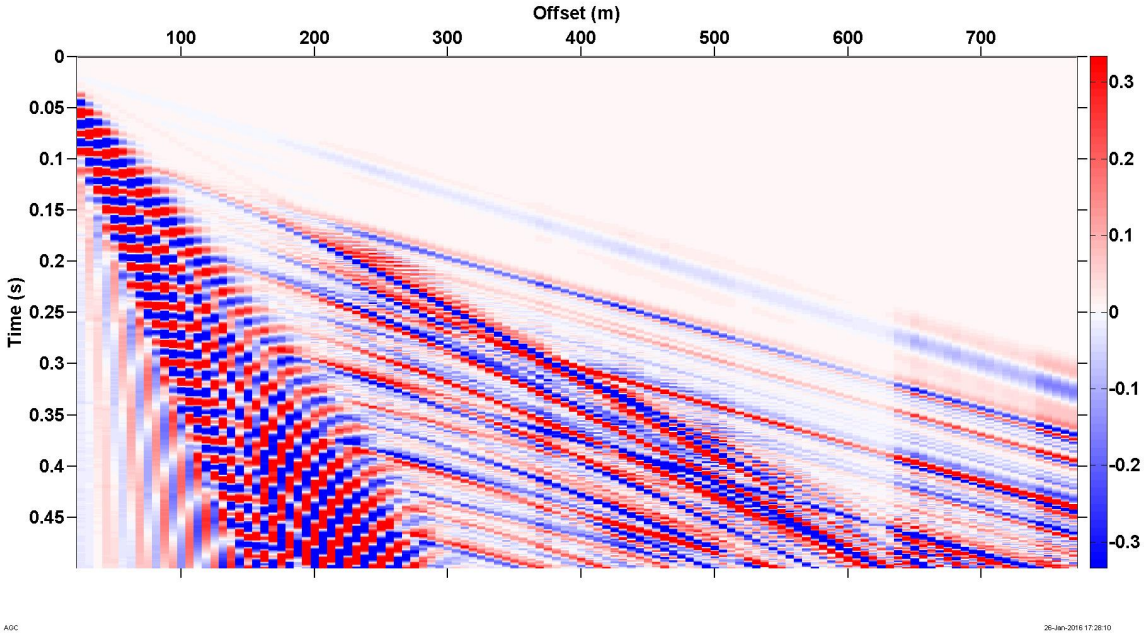

Figure 4.10: A full-waveform synthetic, normalized, shot gather modelled from a sea ice survey near Sveagruva, Svalbard. Flexural ice wave noise is present at low velocities.

4.3.5 Dataset 5: Real shot gather from survey on sea ice near Sveagruva, Svalbard

The fifth, and final, shot gather subjected to processing is the real shot gather obtained during a 2013 survey near Sveagruva, Svalbard which served as the model for the synthetic dataset described in the previous subsection. A detonating cord was used to generate the source signal, and survey parameters are presented in table 4.1. A map showing the

survey lines is presented in figure 4.11. The actual shot gather used was obtained from the East-West line.

Figure 4.11: Map of the 2013 seismic survey performed on sea ice near Sveagruva, Svalbard.

A normalized section of the seismogram is presented in figure 4.12. Notice the presence of flexural ice wave noise at low velocities. We see, however, that if we compare this shot gather to the synthetic shot gather presented in figure 4.10, that the flexural waves arrive earlier in the synthetic gather than in the real gather. This is probably a result of several factors such as different source signatures, scaling factors, ice properties and the fact that the synthetic dataset is only based on a 2-D model. Also, note the presence of some receiver intervals with no data present in figure 4.12. This is probably due to malfunctioning geophones. Processing of the dataset will be presented in Chapter 5. This dataset will from now on be referred to as **Dataset 5**.

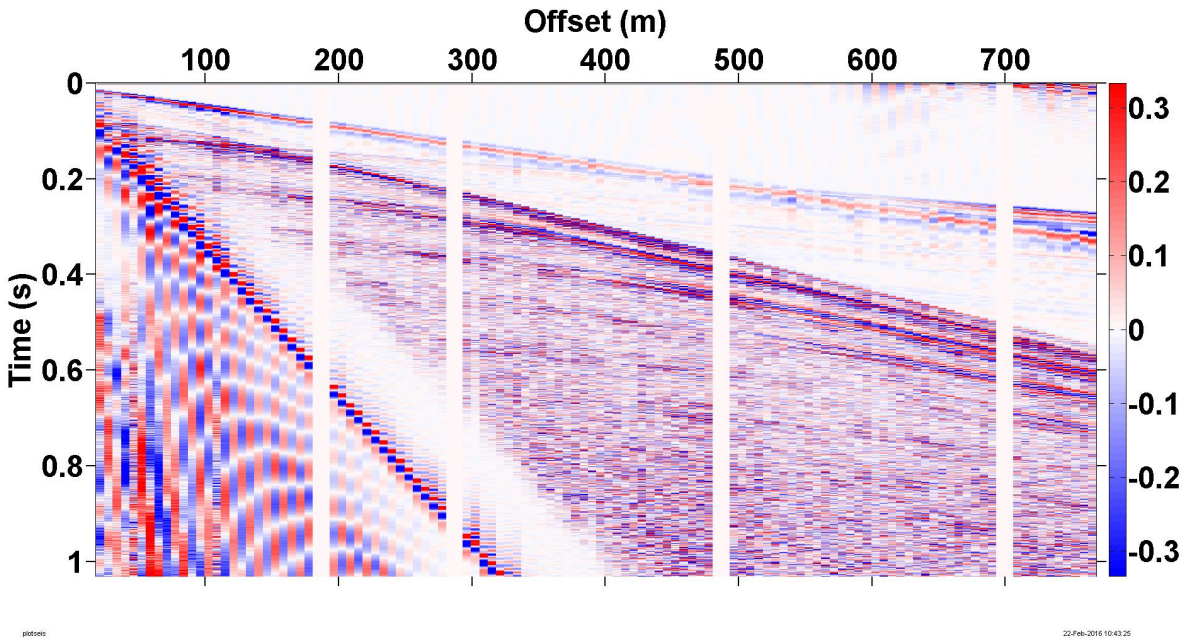

Figure 4.12: Real, normalized, shot gather from survey on sea ice performed near Sveagruva, Svalbard in 2013. Flexural ice wave noise is present at low velocities.

4.4 Summary: methods and datasets

This chapter has provided an overview of procedures, MATLAB programs and datasets used for the modelling and processing work in this thesis. By including a variety of shot gathers, both synthetic and real, the objective has been to accurately assess the efficiency of various processing techniques for flexural wave noise removal on several different types of seismic data. Modelling of flexural ice wave noise has been performed both in order to understand the dispersive nature of the flexural waves, and also so that synthetic flexural waves may be easily generated and added to various shot gathers. The results of the modelling and processing work will now be presented.

Chapter 5

Results of modelling and processing work

As outlined in the previous chapter, flexural ice waves were modelled through an implementation of the theory outlined in Yang and Yates (1995), supplemented by the theory outlined in section 2.7 in order to investigate how dispersion changes with ice temperature and ice thickness. Processing was then performed on the five seismic shot gathers. As will be shown, different seismic processing approaches must be designed for different datasets for optimal results. Dataset 1, which simply consists of three synthetic reflectors, was used to investigate the exact effects and attributes of the three main processing techniques. As such, it is only for this dataset that a full investigation of all three techniques and their effects will be discussed. For the the remaining four datasets, only the most successful processing approach, which often involves a combination of these three methods, will be presented in detail as the inclusion of every single processing approach on all five datasets would be far too exhaustive.

5.1 Results of flexural ice wave noise modelling

Flexural wave noise generated by a line source and point source were modelled using the input parameters presented in table 5.1. The given input yields a Nyquist frequency of 500 Hz.

Parameter	Value
First receiver	5 m
Receiver spacing	5 m
Last receiver	1500 m
Recording length	4 s
Sample interval	1 ms
Ice thickness	2 m

Table 5.1: Input parameters for modelled flexural waves.

The seismogram generated when running the modelling program for a line source is presented in figure 5.1. This is the seismogram generated by the program prior to any AGC-scaling.

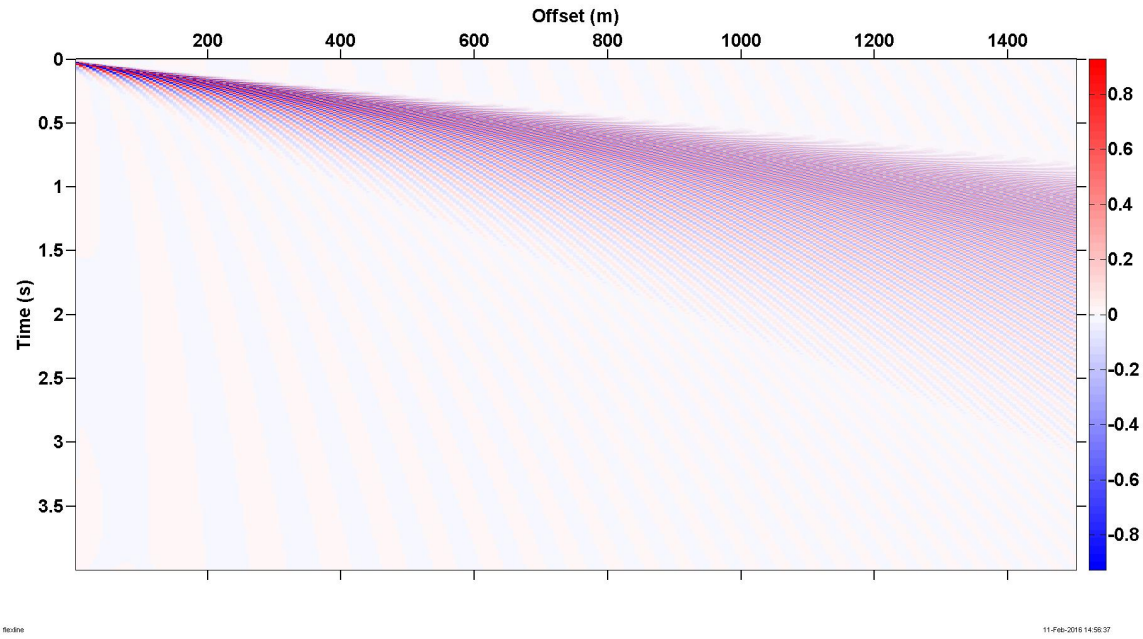

Figure 5.1: Seismogram with modelled flexural ice wave noise generated from a line source using the parameters defined in table 5.1.

From this we see the broad fan of dispersive noise generated. We can also look at a single receiver response to see this better. The geophone located 750 meters from the shot point has the response shown in figure 5.2. From this figure we can see how the high frequency components of the flexural wave arrive earlier than the low frequency components. This

shows the dispersive nature of the wave and is in accordance with the dispersion relation curve generated by the program and presented in figure 5.3. We see from the curve that as the frequency increases, the phase velocity approaches the P-velocity of the water wave (1482 m/s). At this point we see from equation 2.17 that $\mathrm{d}c/\mathrm{d}k = 0$, and phase velocity will then be equal to group velocity. In other words, there is no dispersion beyond the frequency value where this occurs. A likely explanation for this is that the longitudinal ice waves will lose energy to the water when they propagate with phase velocity larger than the water waves. This creates body waves which transport the energy into the water, thus causing attenuation, and the longitudinal mode is therefore referred to as a "leaking mode". Thus, when the flexural wave mode approaches this velocity, wave energy will leak into the water.

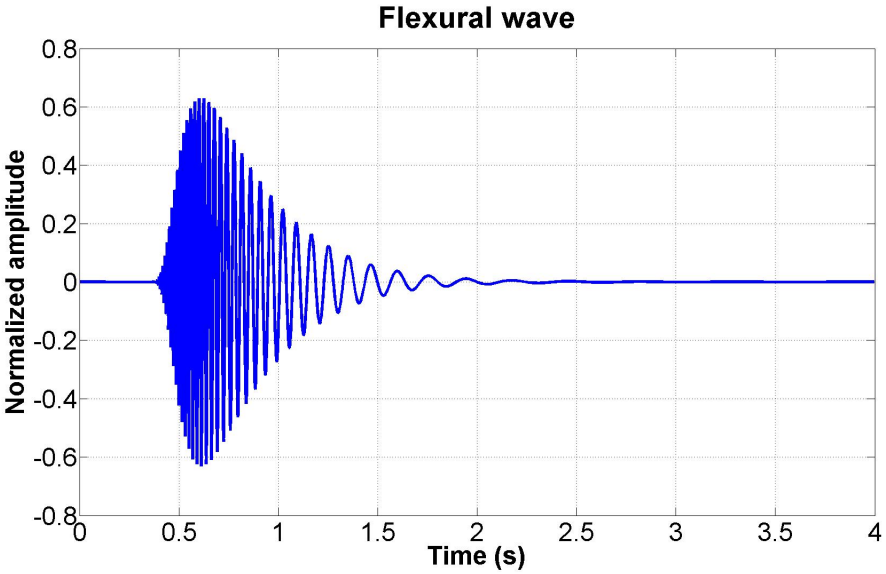

Figure 5.2: Geophone response of the receiver located 750 meters from the shot point when flexural wave noise as modelled from a line source is generated using the parameters defined in table 5.1.

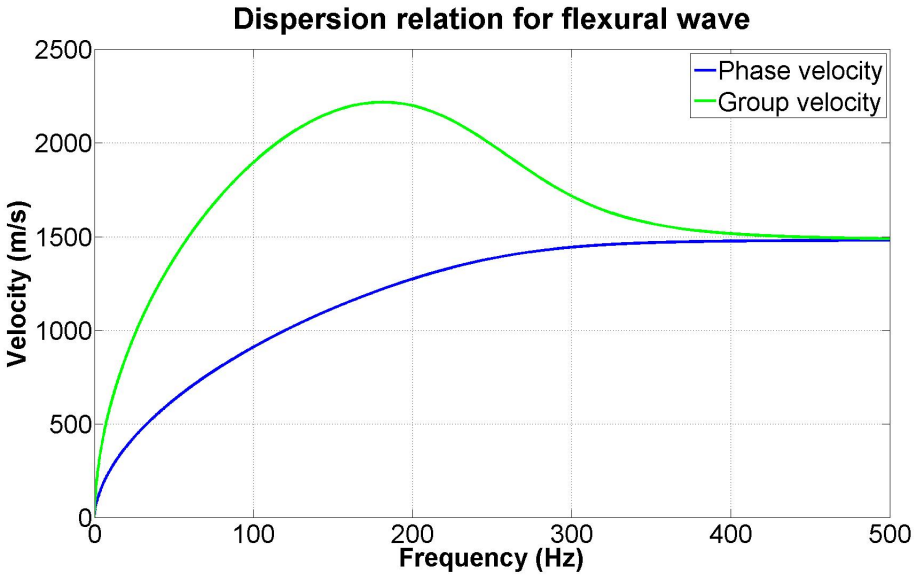

Figure 5.3: Dispersion relation for the modelled flexural wave generated by a line source using the input parameters defined in table 5.1.

For comparison, we can look at the power spectrum generated as a function of frequency and velocity as as described in Section 4.2. This is presented in figure 5.4.

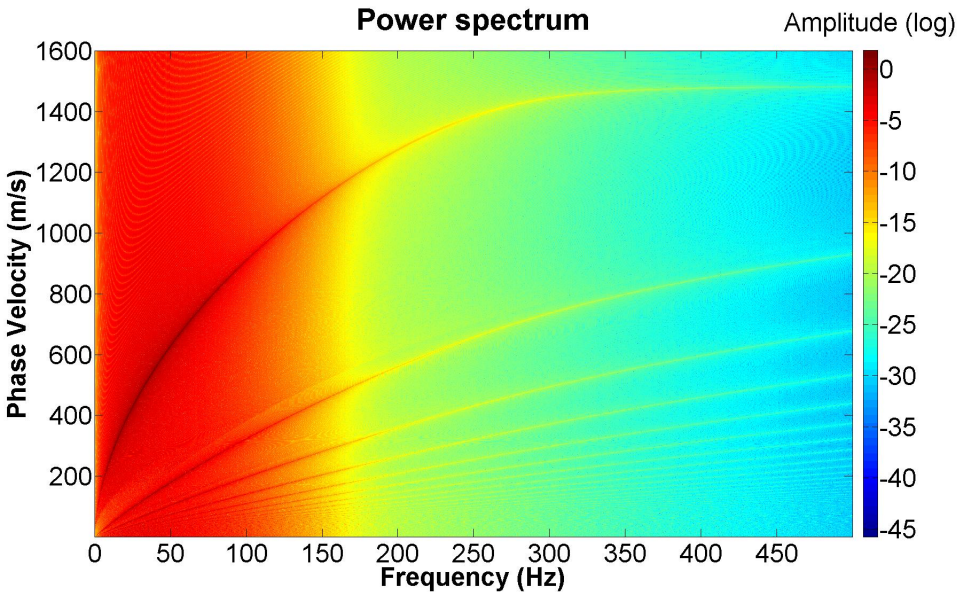

Figure 5.4: Power spectrum for the modelled flexural waves generated by a line source as function of frequency and velocity using the input parameters defined in table 5.1.

This figure is interesting in that there appears to be a set of dispersion curves generated in the power spectrum. We see that the most prominent dispersion curve matches the phase velocity curve in figure 5.3. The other curves represent so-called *side lobes*, or *modes*,

which are generated in an equally spaced receiver array, and which will appear at phase speeds given by (Yang & Giellis, 1994):

$$\frac{1}{v} = \frac{1}{v_0} \pm \frac{m}{f\Delta x}, \tag{5.1}$$

where v is the phase velocity of the side lobe, v_0 is the phase velocity in the primary dispersion curve, m is an integer, f is frequency, and Δx is receiver spacing. For a more thorough discussion of how the receiver geometry results in side lobes, the reader is referred to Chapter 4 in Austegard and Rondenay (2013). In some cases it might be difficult to identify the main lobe from the side lobes (Yang & Giellis, 1994), such as when the receiver spacing is large and many lobes are present, and when several other signals and/or noise events are detected. However, as the MATLAB program used to model flexural ice waves will only plot the dispersion relation of the main lobe (figure 5.3), this program may be used to clearly identify the main lobe. We can see that the main lobe in figure 5.4 corresponds to the dispersion relation curve shown in figure 5.3.

Finally, we can also plot the amplitude and phase spectra for the generated seismogram. These plots are included in figure 5.5. Since we are modelling the flexural waves as generated by a line source, the amplitude spectrum is constant for all offsets.

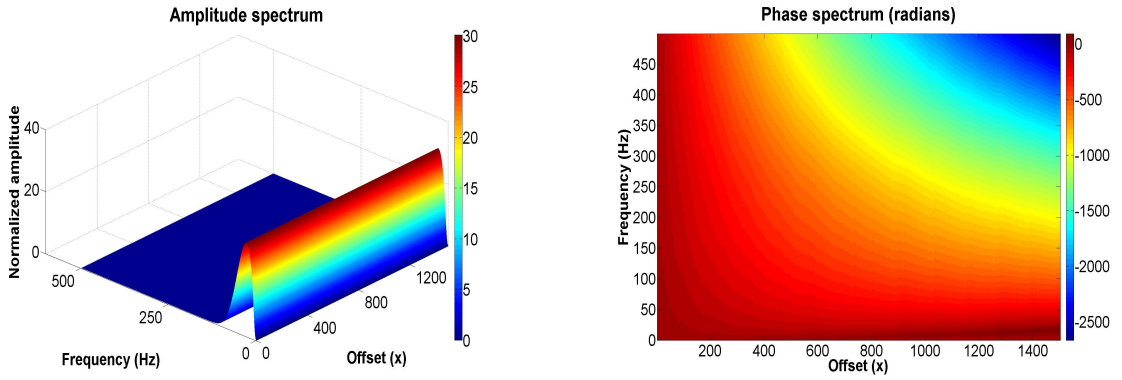

(a) Amplitude spectrum. **(b)** Phase spectrum.

Figure 5.5: Amplitude and phase spectra of modelled flexural waves generated by a line source using the input parameters defined in table 5.1.

We may now, for comparison, use same input parameters and observe how the seismogram generated from a point source differs from the seismogram generated by a line source. The seismogram generated from a point source is shown in figure 5.6, and represents the raw data prior to any AGC-scaling. The power spectrum is presented in figure 5.7. From figure 5.6 we can see that more energy is concentrated near the source point unlike the

line source generated seismogram (figure 5.1) where the energy is constant along the offset line. This is also verified if we plot the amplitude and phase spectra of the seismogram as it is done in figure 5.8.

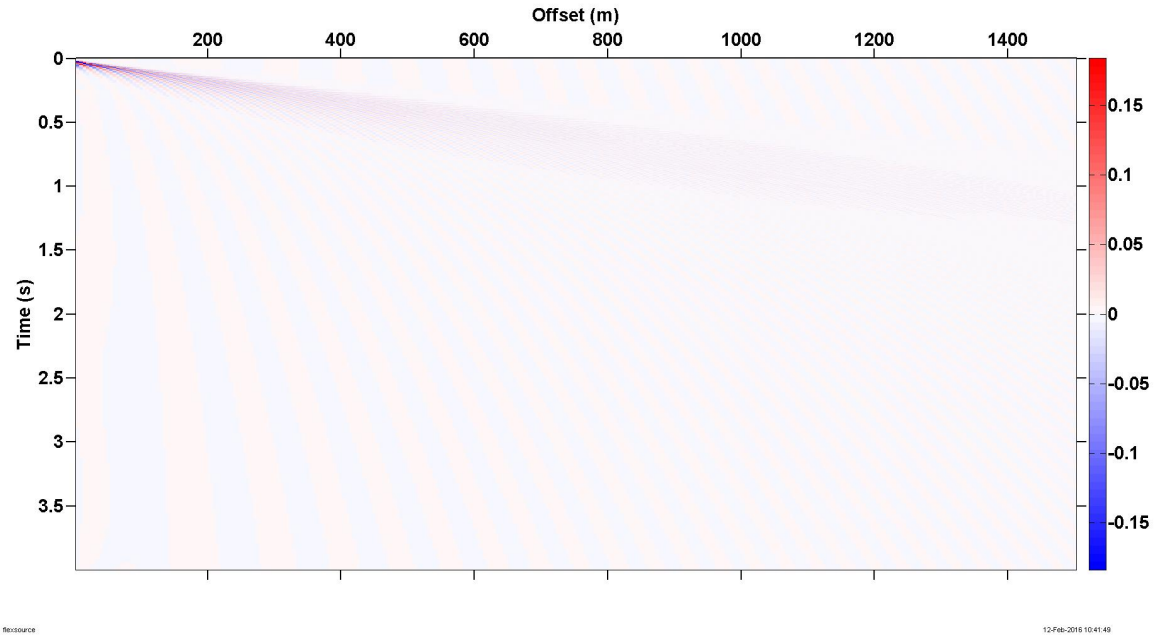

Figure 5.6: Seismogram with flexural ice wave noise as modelled from a point source generated using the parameters defined in table 5.1.

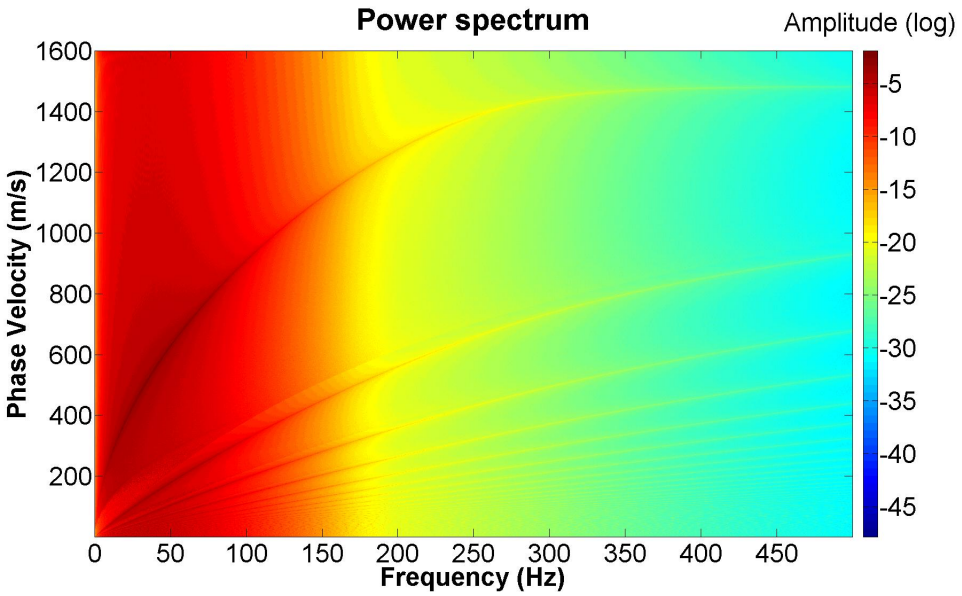

Figure 5.7: Power spectrum for the modelled flexural waves generated by a point source as function of frequency and velocity using the input parameters defined in table 5.1.

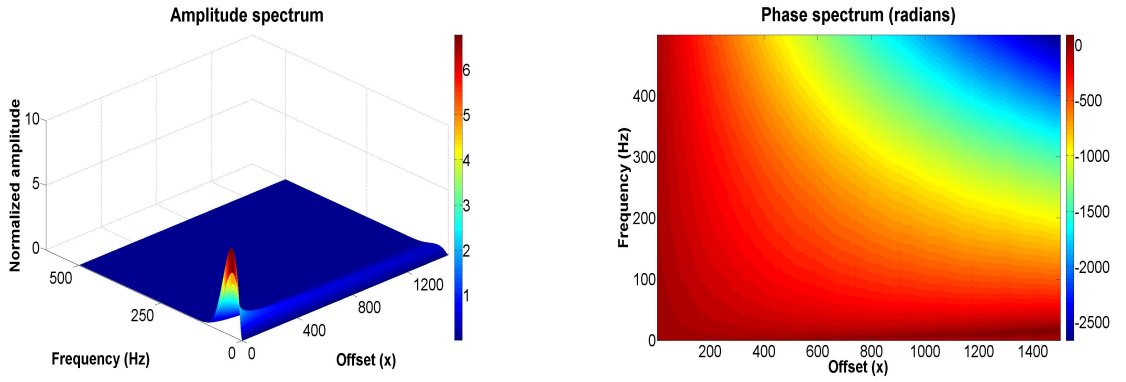

(a) Amplitude spectrum. **(b)** Phase spectrum.

Figure 5.8: Amplitude and phase spectra of seismogram generated by a point source using the input parameters defined in table 5.1.

The next step was to study how the dispersion relation is affected by variations in ice temperature and ice thickness. To observe how temperature affects the dispersion relation, we assume a fixed ice thickness of 2 meters. Utilizes the equations outlined in Section 2.7, we may observe how the dispersion is affected by temperature. The dispersion relation for phase velocity and group velocity as function of temperature is presented in figure 5.9. From the figures we see that velocities increase when the temperature drops from $-2°C$ to $-4°C$. We also see that once the temperature becomes approximately $-6°C$, further temperature decrease will have almost no effect on the velocity dispersion. The obvious reason for this is that as the temperature becomes closer to $0°C$, ice will become more slushy and frozen pore water may start to melt, thus reducing the bulk and shear moduli of the ice.

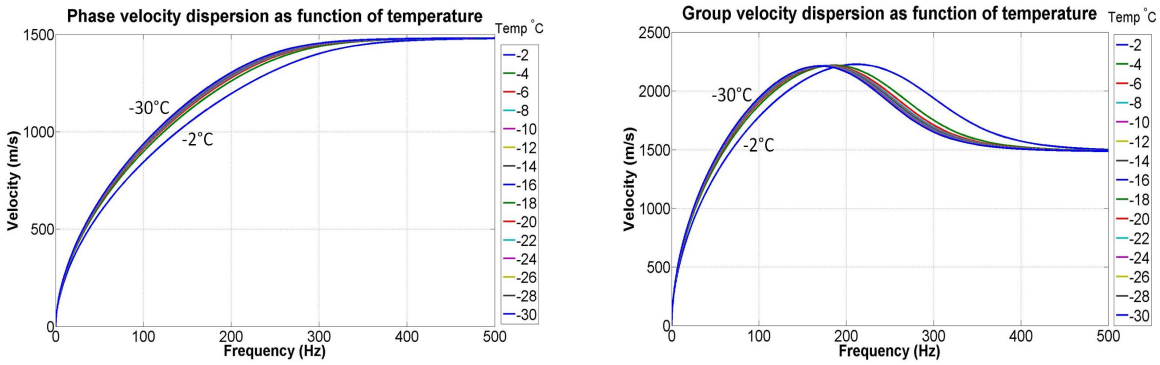

(a) Phase velocity dispersion. **(b)** Group velocity dispersion.

Figure 5.9: Dispersion relation for phase and group velocity as function of temperature with ice thickness equal to 2 meters.

Plotting the phase and group velocities together reveals how the dispersion ceases as the

frequency increases. This is illustrated in figure 5.10. We also see from this plot that at low frequencies, the coldest ice will have the highest group velocity, but at frequencies above approximately 190 Hz, the plot indicates that the group velocity becomes highest in the warmer ice layers as the group velocity dispersion curves for the cold ice layers begin to approach their respective phase velocity curves.

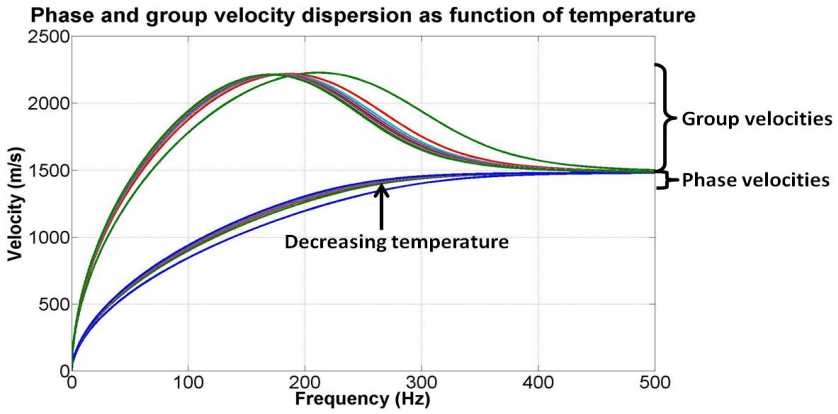

Figure 5.10: Dispersion relation for phase and group velocity as function of temperature plotted together.

The dispersion relation as function of ice temperature may also be plotted in 3-D for smoother interpolation between the temperature values. This is illustrated in figure 5.11.

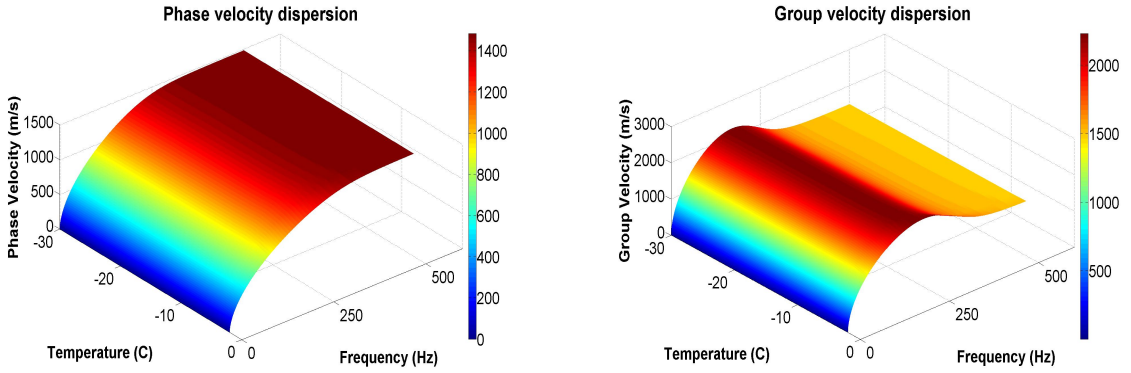

(a) Phase velocity dispersion. **(b)** Group velocity dispersion.

Figure 5.11: Interpolated dispersion relation for phase and group velocity as function of temperature.

It should finally be noted that the the frequency value where the group velocities become higher in the warmer ice layers than in the colder layers is dependent on ice thickness. As an example, if we run the same modelling as above, but with ice thickness set equal to 1 meter, we obtain the group velocity dispersion illustrated in figure 5.12. From this figure

we see that the frequency at which the group velocities become highest in the warmer ice layers is approximately 360 Hz.

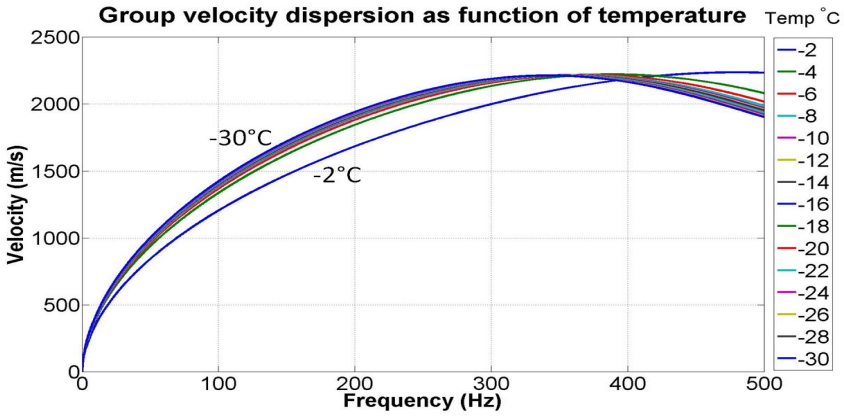

Figure 5.12: Group velocity dispersion with ice thickness equal to 1 meter.

In order to model how the dispersion relation is affected by ice thickness, we first assume a fixed ice temperature of $-2°C$. We may then model the dispersion relation as a function of ice thickness, assuming that ice salinity changes for each thickness according to equation 2.47. If we input an array of thickness values spanning from 1 to 10 meters, in increments of 1 meter, we obtain the results presented in figure 5.13. We see from the figure that phase velocities increase with increased ice thickness until they converge to the P-velocity of water waves. The increase in phase velocity with increasing ice thickness follows from equation 2.29 in that larger ice thickness causes an increase in ice rigidity. From this we also see how group velocities are highest in thick ice sheets at low frequencies, but at frequencies above approximately 50 Hz, thinner ice layers will have the higher group velocities. These results are in agreement with similar results obtained by Shei, Ward, and Veith (1983), Hunkins (1995) and Bakke (2015). A plot of both phase and group velocities is presented in figure 5.14.

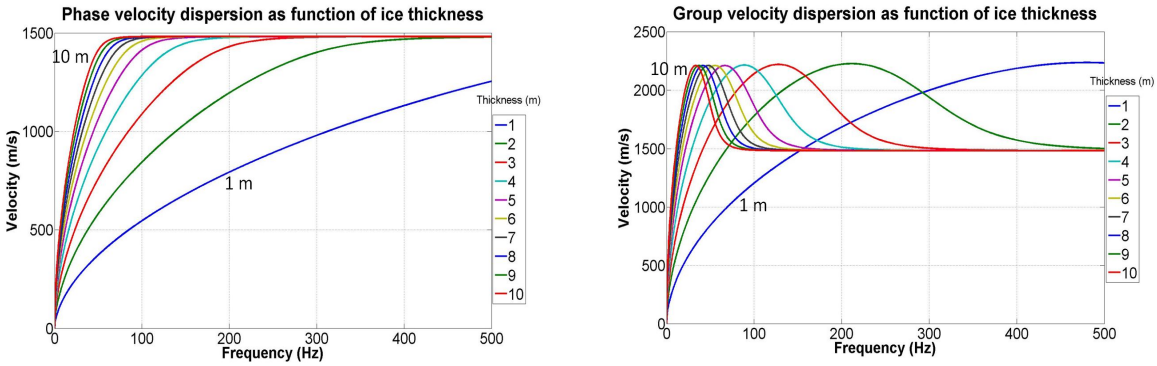

(a) Phase velocity dispersion. **(b)** Group velocity dispersion.

Figure 5.13: Dispersion relation for phase and group velocity as function of ice thickness.

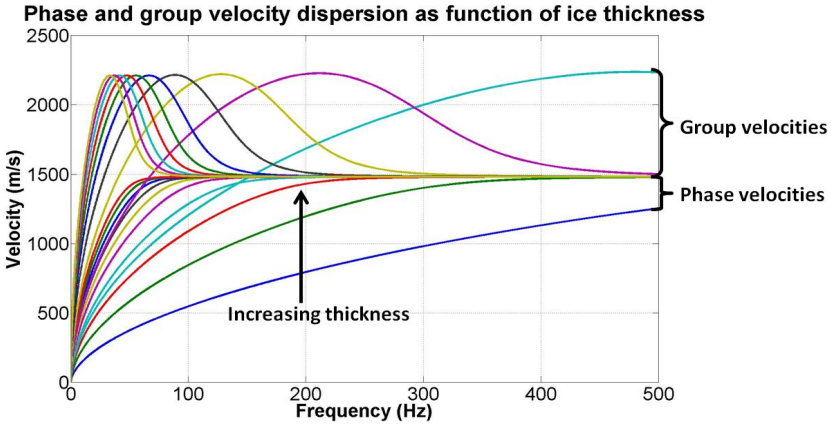

Figure 5.14: Dispersion relation for phase and group velocity as function of ice thickness plotted together.

An interpolated 3-D plot of the dispersion relation as function of ice thickness is presented in figure 5.15.

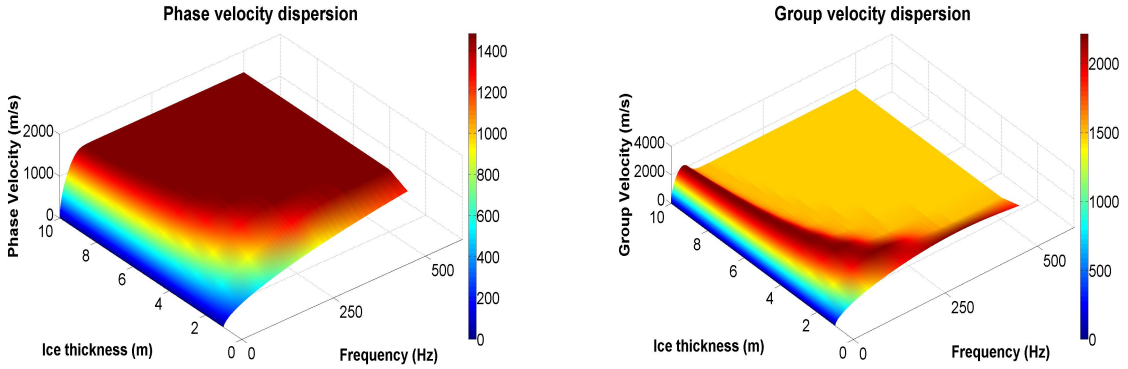

(a) Phase velocity dispersion. **(b)** Group velocity dispersion.

Figure 5.15: Interpolated dispersion relation for phase and group velocity as function of ice thickness.

In summary, we can conclude that the frequency bandwidth in which flexural wave dispersion occurs is dependent on both ice temperature and ice thickness. Colder temperatures and higher ice thickness cause the dispersion to primarily manifest itself at lower frequencies whereas an increase in ice temperature and a decrease in ice thickness will cause the the dispersion to occur over a wider bandwidth.

5.2 Processing of Dataset 1

As outlined in Section 4.3, Dataset 1 is a simple synthetic seismogram consisting of three reflectors with added flexural ice wave noise generated by a line source. The seismogram before and after the addition of flexural noise, as well as their respective dispersion relations as interpreted from their power spectra, are presented in figure 5.16.

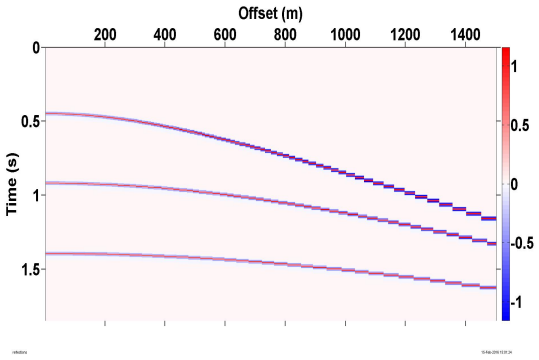

(a) Dataset 1 without flexural noise.

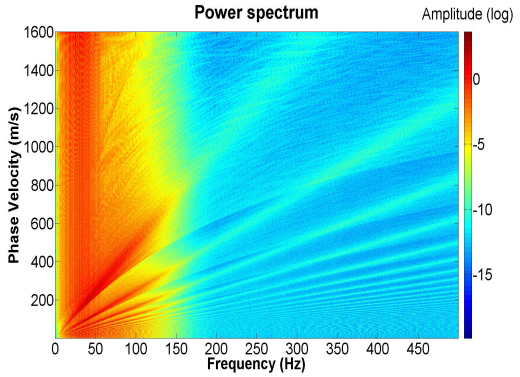

(b) Power spectrum without flexural noise.

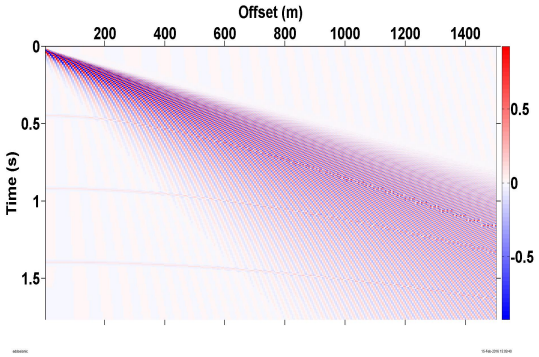

(c) Dataset 1 with flexural noise.

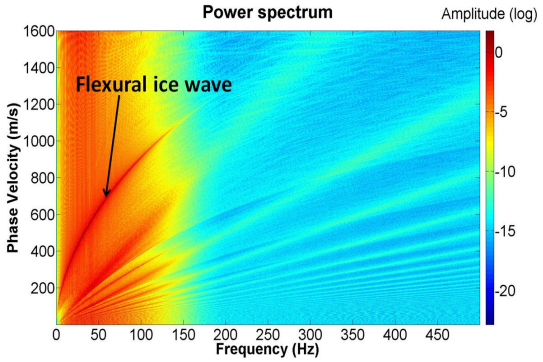

(d) Power spectrum with flexural noise.

Figure 5.16: Dataset 1 before and after added synthetic flexural noise. Note the apparent dispersion relation curve for the flexural waves in subfigure (d).

Processing of the seismogram was performed using the $f-k$ transform, the $\tau-p$ transform and the RT transform in order to compare the efficiency of the various methods. No other

processing techniques such as scaling, deconvolution, etc. were utilized, as the purpose of this seismogram simply was to test the various MATLAB programs developed for the processing techniques as well as to study effects and attributes of the three techniques. Thus, the overall aim was simply to start out with three reflectors, add flexural ice wave noise, and attempt to retrieve the reflectors again.

The processing of Dataset 1 via the $f-k$ transform is presented in figure 5.17. We see that the flexural wave dispersion curve is easily identifiable in the $f-k$ domain, and that no apparent aliasing occurs. This means that frequency components are lower than the value found through equation 3.3. A simple mute was therefore applied in order to remove the flexural wave noise in the $f-k$ domain. Although some flexural wave noise remains after the dataset is transformed back to the $x-t$ domain again, the reflectors are now clearly visible.

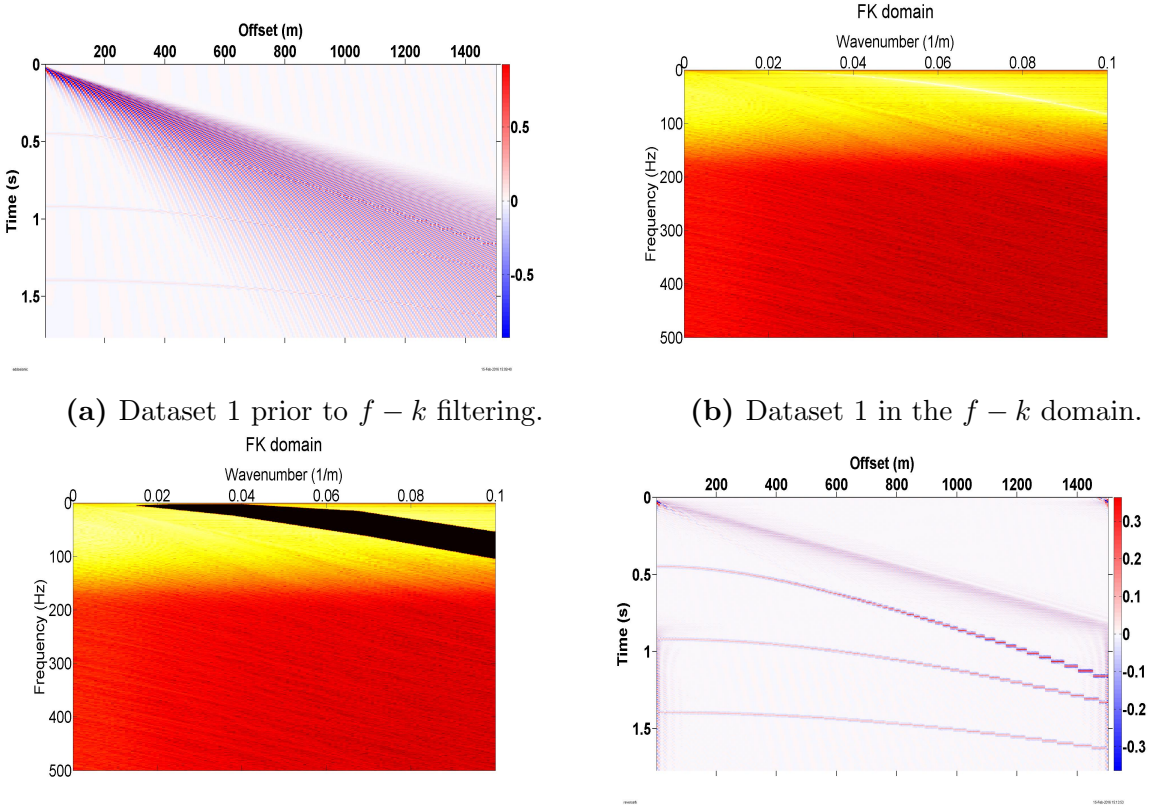

(a) Dataset 1 prior to $f-k$ filtering.

(b) Dataset 1 in the $f-k$ domain.

(c) Muting in the $f-k$ domain.

(d) Dataset 1 after $f-k$ filtering.

Figure 5.17: $f-k$ filtering of Dataset 1.

If we plot the amplitude and phase spectra prior to the adding of synthetic flexural noise, with flexural wave noise added, and subsequent to $f-k$ filtering, we obtain the results presented in figure 5.18. In this case, we see that the amplitude and phase spectra

subsequent to filtering are quite similar to the original data except at small offsets where remnant flexural wave noise still dominates. This is even more evident if we perform velocity picking, NMO-correction and stacking of the data. The results are presented in figure 5.19. We see the presence of noise near $TWT = 0$ seconds. This may, however, easily be removed through applying a simple mute in the NMO-corrected seismogram. The final stacked seismogram with the mute applied, compared with an initial stacked seismogram generated prior to the adding of synthetic flexural noise, and the stacked seismogram with added flexural noise, all using the same velocity picks, is presented in figure 5.20. We can now see that the final NMO-corrected seismogram and stack are almost identical to the NMO-corrected and stacked seismogram obtained prior to the adding of flexural noise. Thus, $f - k$ filtering is quite efficient as long as aliasing is avoided in the $f - k$ domain.

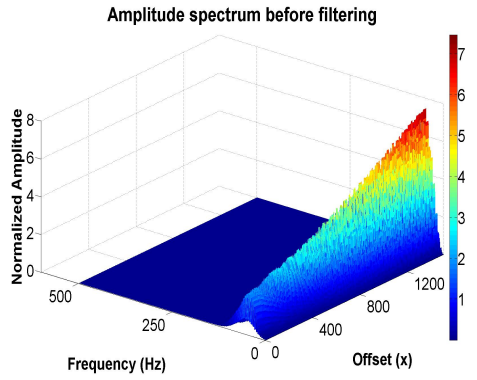

(a) Amplitude spectrum prior to noise addition.

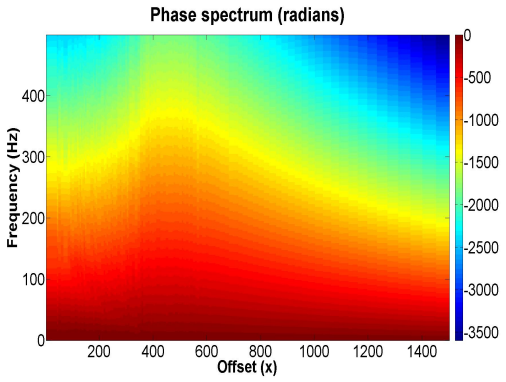

(b) Phase spectrum prior to noise addition.

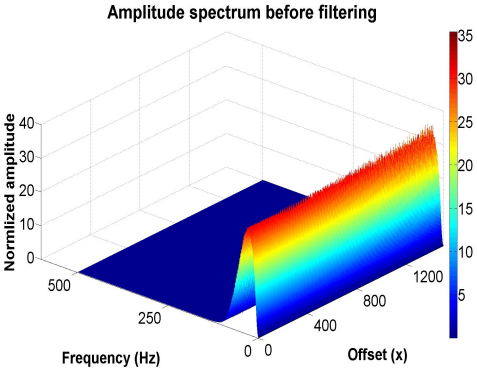

(c) Amplitude spectrum with added noise.

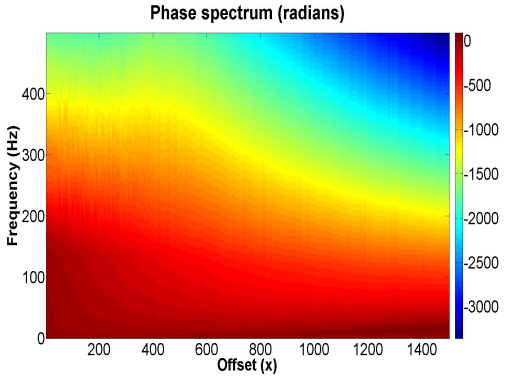

(d) Phase spectrum with added noise.

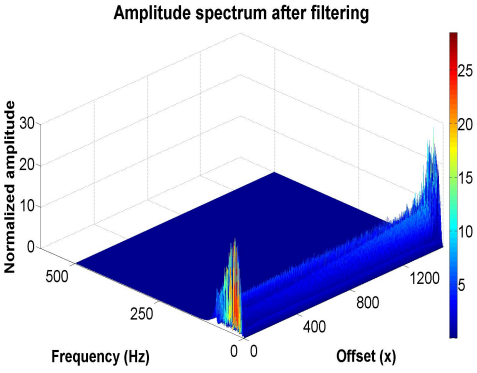

(e) Amplitude spectrum after $f-k$ filtering.

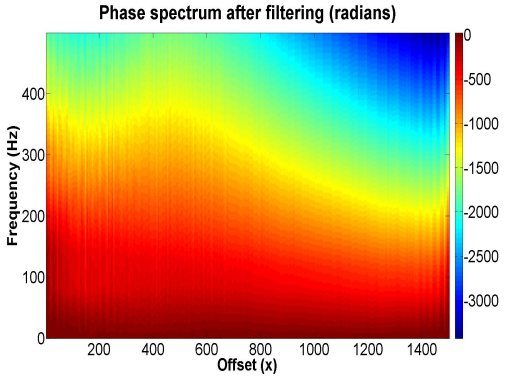

(f) Phase spectrum after $f-k$ filtering.

Figure 5.18: Amplitude and phase spectra of Dataset 1 before and after $f-k$ filtering.

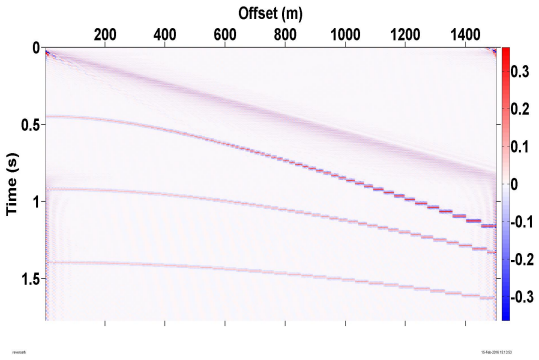

(a) $f - k$ filtered seismogram.

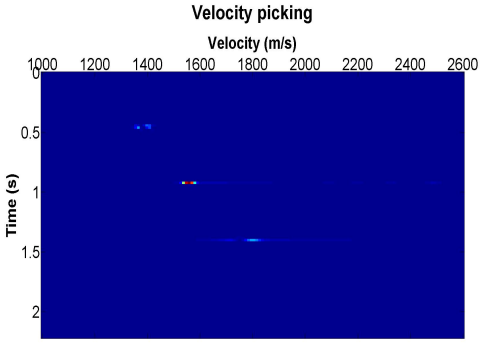

(b) Velocity picking.

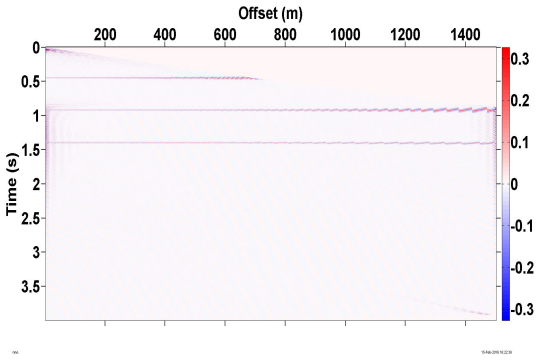

(c) NMO-corrected seismogram.

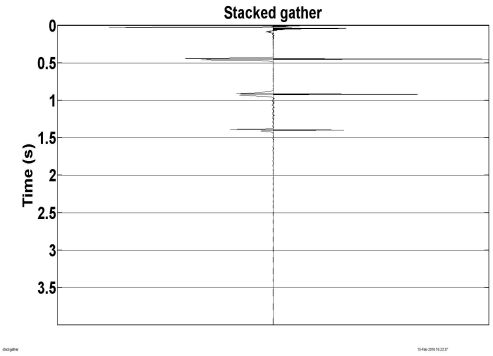

(d) Stacked seismogram.

Figure 5.19: Velocity picking, NMO-correction and stacking of $f - k$ filtered Dataset 1.

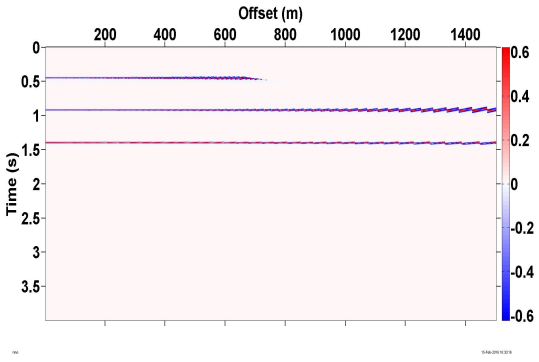

(a) NMO-corrected seismogram prior to noise addition.

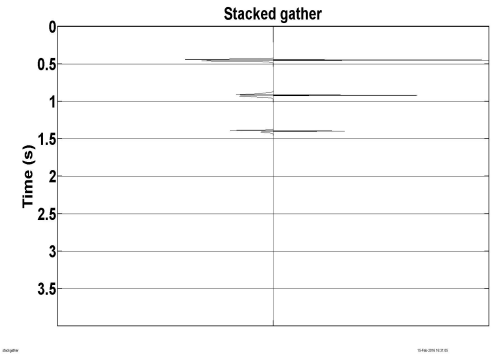

(b) Stacked seismogram prior to noise addition.

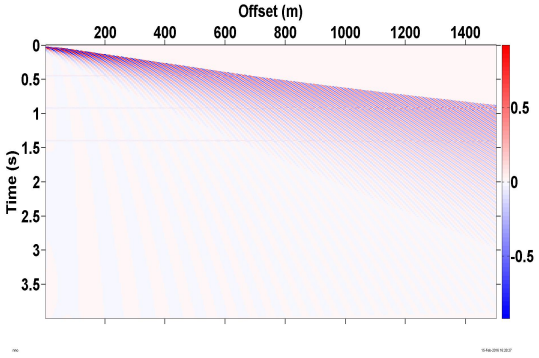

(c) NMO-corrected seismogram after noise addition.

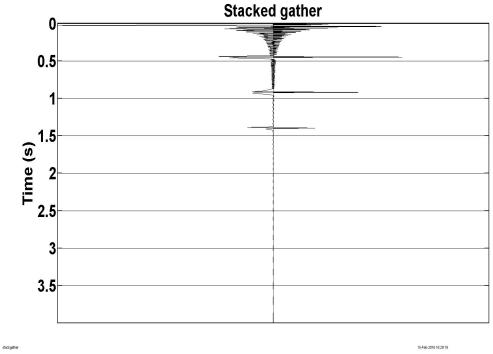

(d) Stacked seismogram after noise addition.

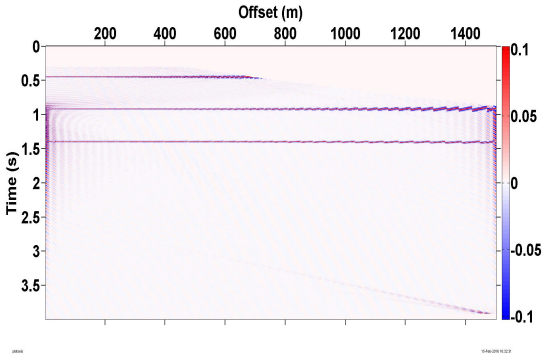

(e) NMO-corrected seismogram after $f-k$ filtering and muting.

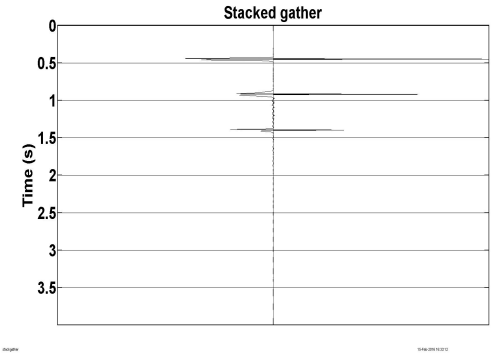

(f) Stacked seismogram after $f-k$ filtering and muting.

Figure 5.20: NMO-correction and stacking of Dataset 1 prior to noise addition, after noise addition, and after $f-k$ filtering and muting.

The processing of Dataset 1 via the $\tau-p$ transform is presented in figure 5.21. A slowness interval was defined as $p \in \{0, 1/1350\}$. This automatically mutes all flexural wave components with phase velocities lower than 1350 m/s. Further, we know from the dispersion analysis that the maximum flexural wave phase velocity is equal to 1482 m/s. This means that only a small fan of flexural wave noise should still be present. Furthermore, we know that the zero-intercept time for the reflectors will have a maximum value slightly below 1.5

seconds, as is evident from figure 5.17a. Thus, we may mute all parts of the $\tau - p$ domain with higher τ-value. This will also effectively remove energy located at large intercept times, including events that have negative intercept-time values originally and which have been subjected to a wrap-around effect, causing them to appear at large intercept times instead.

As noted in Section 4.2, the program used for $\tau - p$ filtering needs quite a lot of computation time, and the slowness sampling interval is therefore set equal to $dp = (p_{max} - p_{min})/N$ where N is the number of traces. This will in most cases result in aliasing effects following inequality 3.13. From the processing illustrated in figure 5.21 we see the aliasing effects in the $\tau - p$ domain, and also in the final seismogram obtained after $\tau - p$ filtering. This is especially evident at far offsets where smearing effects can also be seen. Nevertheless, we see that simple $\tau - p$ filtering still is very efficient in removing flexural wave noise while retaining the underlying signals.

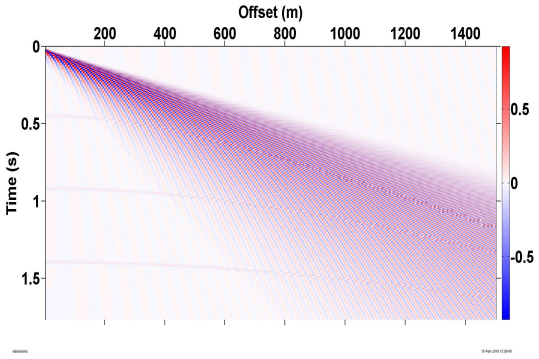

(a) Dataset 1 prior to $\tau - p$ filtering.

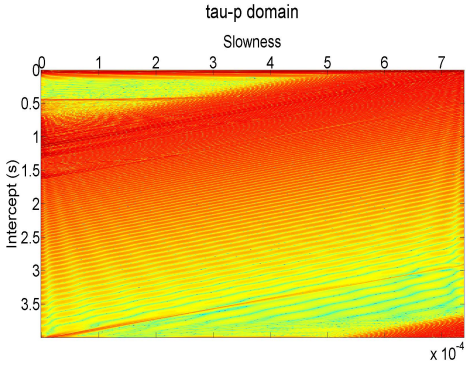

(b) Dataset 1 in the $\tau - p$ domain.

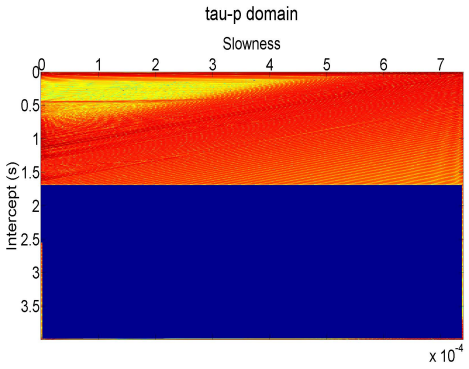

(c) Muting in the $\tau - p$ domain. The blue area is muted.

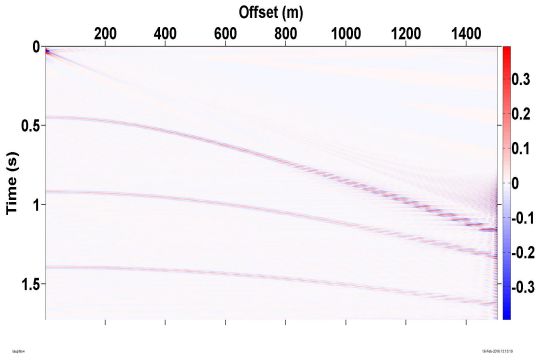

(d) Dataset 1 after $\tau - p$ filtering.

Figure 5.21: $\tau - p$ filtering of Dataset 1.

If we plot the amplitude and phase spectra of the filtered seismogram we obtain the results presented in figure 5.22. We see that the resulting amplitude spectrum is quite similar to

the spectrum obtained after $f-k$ filtering (figure 5.18e) but the phase spectrum is quite noisy in comparison. This is most likely due to aliasing effects caused by undersampling in the $\tau-p$ domain. The problem with phase shifts is that they may cause trouble when performing NMO-correction and stacking as the phases will not align properly. However, by performing NMO-correction and stacking using the same velocity picking results as we obtained in the previous subsection, the results nevertheless are good, but just as with the $f-k$ filtering, much noise is present near $TWT = 0$ seconds. Applying a simple mute on this part of the NMO-corrected dataset yields the best and final result. Results of NMO-correction and stacking, with and without mute, are presented in figure 5.23.

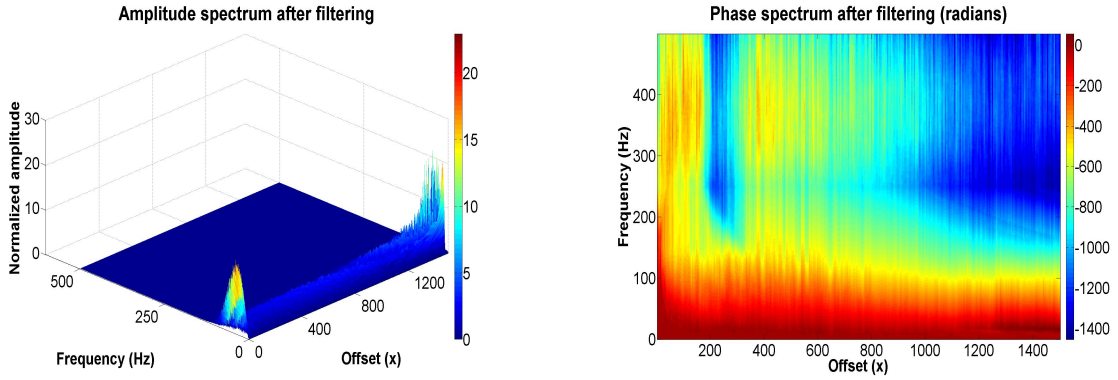

(a) Amplitude spectrum after $\tau-p$ filtering. **(b)** Phase spectrum after $\tau-p$ filtering.

Figure 5.22: Amplitude and phase spectra of Dataset 1 after $\tau-p$ filtering.

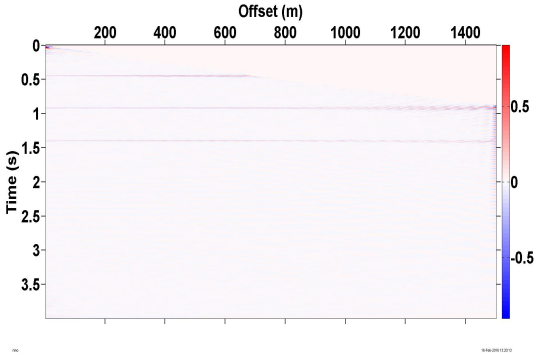

(a) NMO-corrected seismogram after $\tau - p$ filtering.

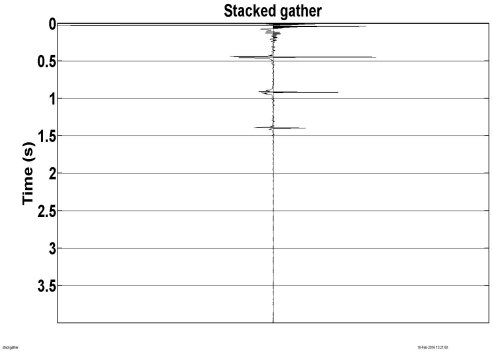

(b) Stacked seismogram after $\tau - p$ filtering.

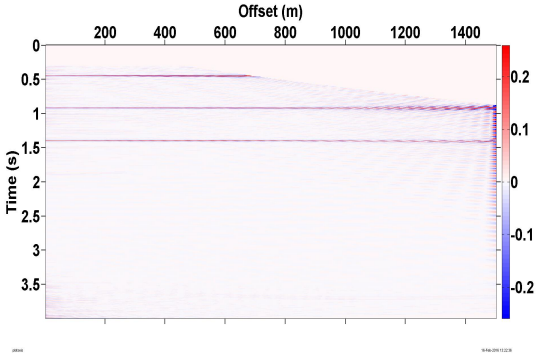

(c) NMO-corrected seismogram after $\tau - p$ filtering and muting.

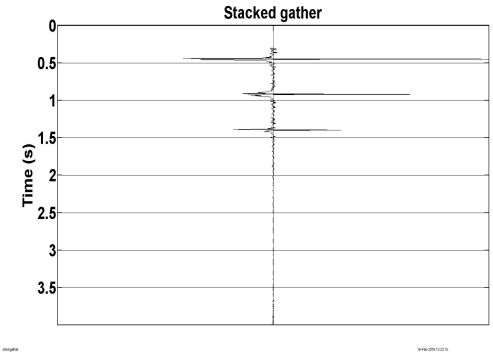

(d) Stacked seismogram after $\tau - p$ filtering and muting.

Figure 5.23: NMO-correction and stacking of Dataset 1 after $\tau - p$ filtering with and without muting in NMO-corrected dataset.

The processing of Dataset 1 via the RT transform is presented in figure 5.24. A velocity interval spanning from $v = 400$ m/s to $v = 2000$ m/s with increments of 1 m/s was used as input to the function as the flexural waves obscure the reflectors the most in this interval, as can be seen from figure 5.24a. The spectral clipping threshold was set at 10 times the median value of each Fourier transformed radial trace. All amplitude values exceeding this value were reduced to the median value of the spectrum. From figure 5.24 we see that the flexural wave noise is greatly reduced, but the reflectors are rather weak and difficult to see properly as no scaling has been applied to the dataset. A good way to compensate for this would also be to remove the high amplitude noise still present at low offset and low two-way-traveltime values. The amplitude and phase spectra obtained after the RT filtering are presented in figure 5.25, and we see that these are in great agreement with the amplitude and phase spectra of the original data (figure 5.18) except at low offsets.

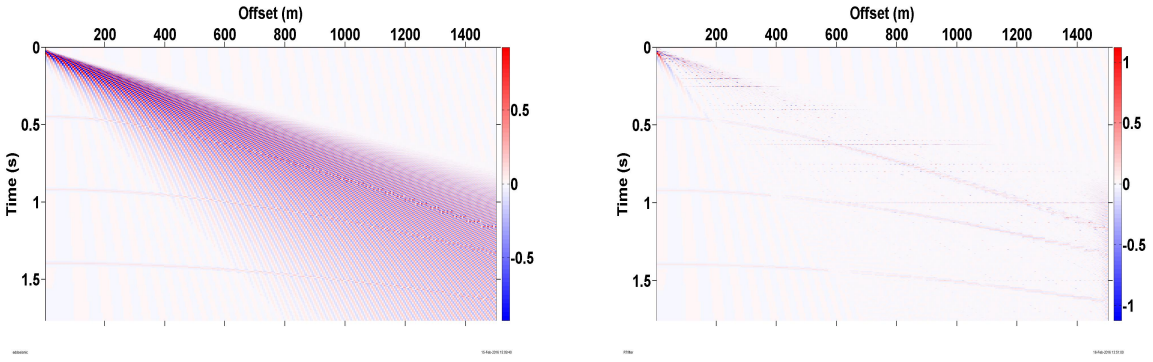

(a) Dataset 1 prior to RT filtering. **(b)** Dataset 1 after RT filtering.

Figure 5.24: RT filtering of Dataset 1.

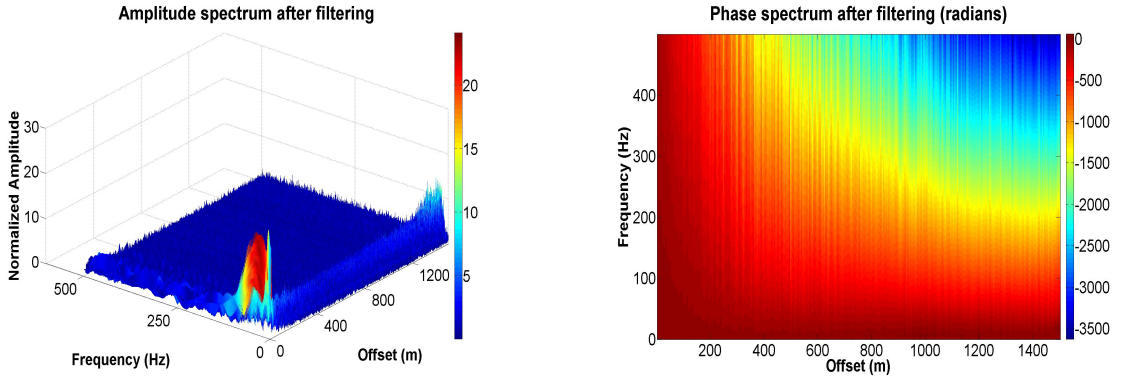

(a) Amplitude spectrum after RT filtering. **(b)** Phase spectrum after RT filtering.

Figure 5.25: Amplitude and phase spectra of Dataset 1 after RT filtering.

Before turning to NMO-correction, however, it may be interesting to analyze the features of the RT transform. Plotting the amplitude and phase spectra in the RT domain prior to, and subsequent to, RT filtering, reveals the properties of the filtering technique. This is presented in 5.26. From the figure we see that the spectral clipping has no effect on the phase spectrum. However in the amplitude spectrum prior to filtering, a clear dispersion relation between velocity and frequency is present in the data. Subsequent to filtering, this high-amplitude noise has been reduced, and we see that the normalized amplitude values are greatly reduced as well. To illustrate this further, we may observe the spectral clipping of a single radial trace. For the velocity $v = 1000$ m/s, the amplitude spectrum before and after filtering is presented in figure 5.27. Notice how the various modes of the flexural wave manifest themselves in the data. After filtering, the normalized amplitude values are greatly reduced for the noise peaks, and, thus, the flexural wave noise is greatly damped when transforming back to the $x - t$ domain again. It is also interesting to observe that the relationship between frequency and velocity in the captured radial trace

corresponds with the group velocity dispersion as presented in figure 5.3.

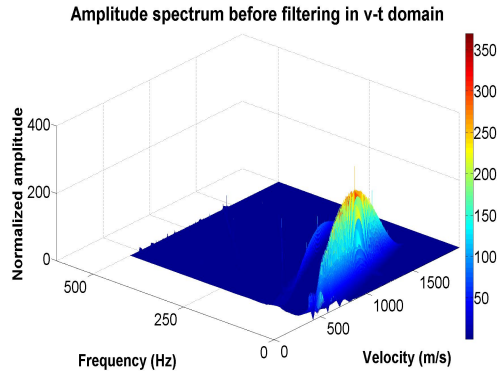

(a) Amplitude spectrum in RT domain prior to filtering.

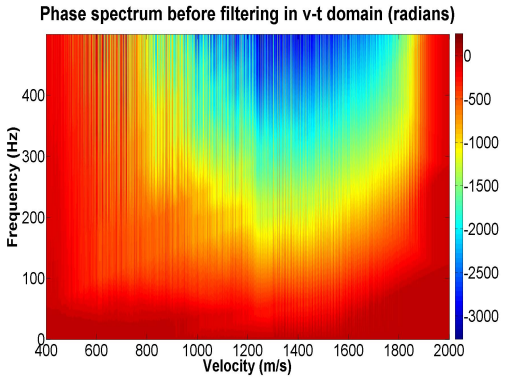

(b) Phase spectrum in RT domain prior to filtering.

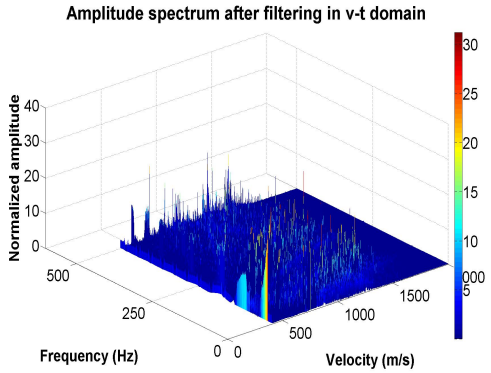

(c) Amplitude spectrum in RT domain after filtering.

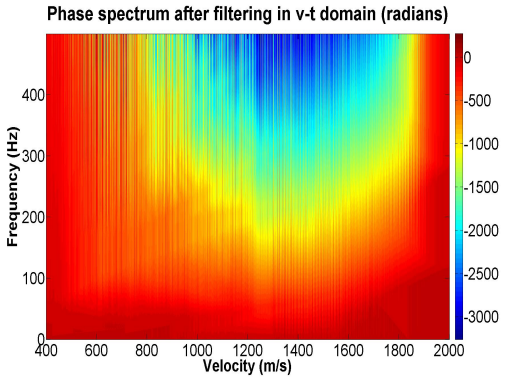

(d) Phase spectrum in RT domain after filtering.

Figure 5.26: Amplitude and phase spectra of Dataset 1 in RT domain before and after filtering.

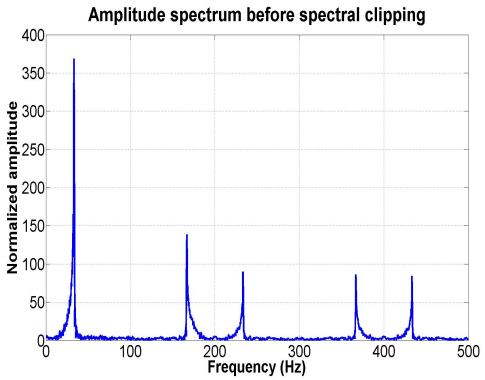

(a) Amplitude spectrum before filtering.

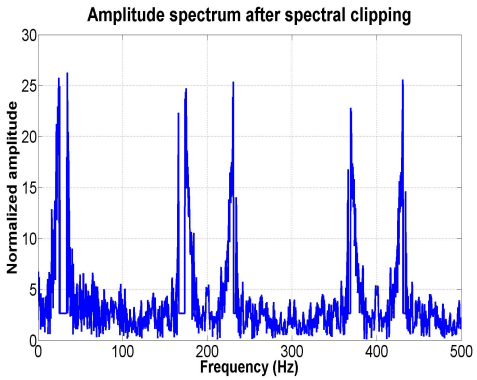

(b) Amplitude spectrum after filtering.

Figure 5.27: Amplitude spectrum for the radial trace $v = 1000$ m/s before and after RT filtering.

Turning now to NMO-correction and stacking, figure 5.28 illustrates that through muting the near-offset noise, we obtain a much better stack. However, more noise remains subsequent to RT filtering than through the other methods. This is most likely due to the

rather crude spectral clipping method applied, and better results may be applied through fine tuning of the spectral clipping threshold, or by applying iterative RT filters over the same velocity fan. In addition, the amplitudes of the reflectors appear to be equal to, or even higher, than the flexural ice wave amplitudes at low velocities ($v < 400$ m/s), so any RT filtering applied to this part of the seismogram would remove the reflectors instead of the noise. This phenomena is not that likely to be found on real datasets though, as flexural ice waves in general tend to have higher amplitudes than reflectors at all velocity trajectories.

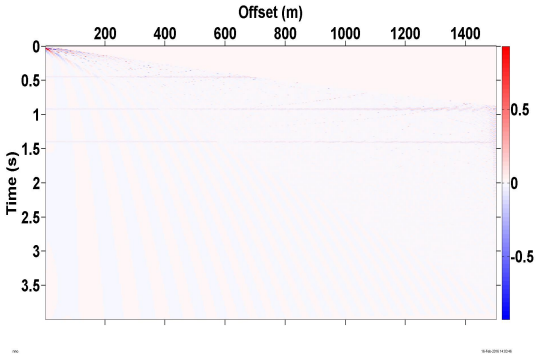

(a) NMO-corrected seismogram after RT filtering.

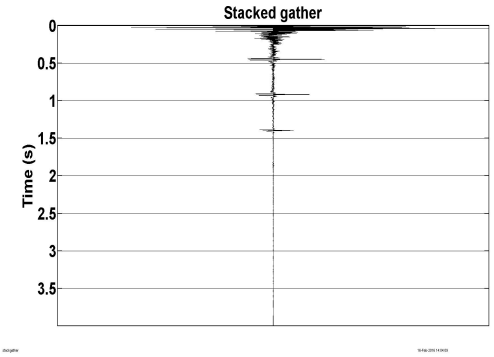

(b) Stacked seismogram after RT filtering.

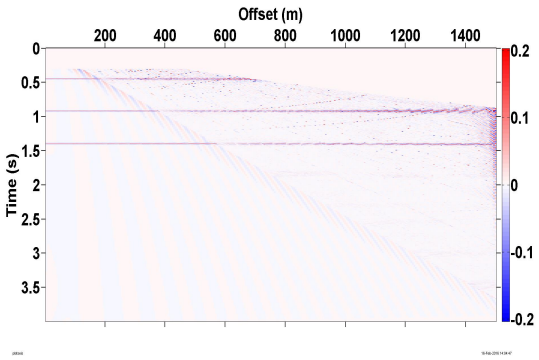

(c) NMO-corrected seismogram after RT filtering and muting.

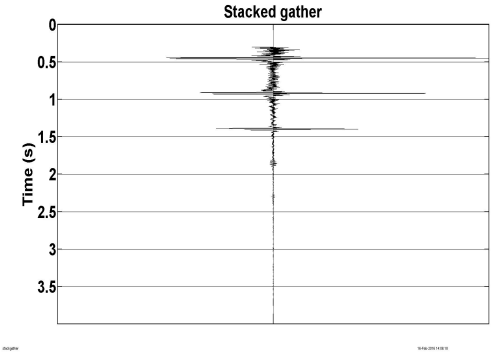

(d) Stacked seismogram after RT filtering and muting.

Figure 5.28: NMO-correction and stacking of Dataset 1 after RT filtering with and without muting in NMO-corrected dataset.

In conclusion, all three processing methods are effective in filtering flexural ice wave noise on Dataset 1. From the results presented in this subsection, it appears that $f-k$ filtering produces the best results when applied to Dataset 1 as hardly any flexural wave noise remains subsequent to filtering, and the phase spectrum is largely unaffected. The $\tau - p$ transform is also very efficient in filtering noise, but aliasing effects are prominent, and the resulting phase spectrum is by far the most distorted. RT filtering does not have

the same effect on the phase spectrum, but it leaves more remnant noise behind. This may, however, be improved through fine tuning of the spectral clipping threshold, or by applying an iterative RT filter over the parts of the seismogram most affected by flexural ice wave noise.

5.3 Processing of Dataset 2

Dataset 2, a full-waveform synthetic marine dataset with added synthetic flexural ice wave noise generated by a point source, was scaled prior to processing in order to enhance the visibility of the data. This scaling was done via the program 'AGCgain.m' from the SeismicLab package. The seismograms before and after the addition of flexural noise, and the interpreted dispersion relations estimated via the power spectrum, are presented in figure 5.29. The dispersion curve for the flexural waves can be seen here. Another interesting phenomena we can observe in the power spectrum is the presence of a constant velocity event at around 1500 m/s which most likely corresponds to the P-wave velocity of the waver wave.

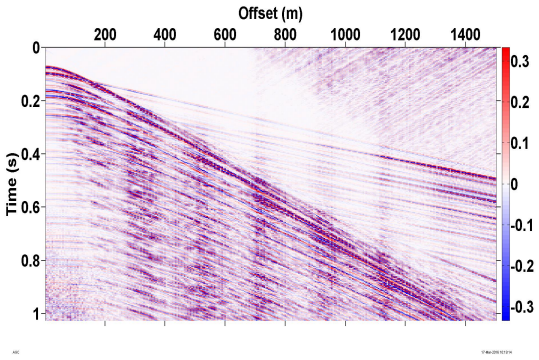

(a) Dataset 2 without flexural noise.

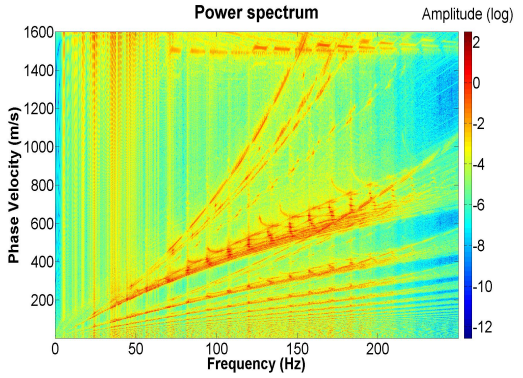

(b) Power spectrum without flexural noise.

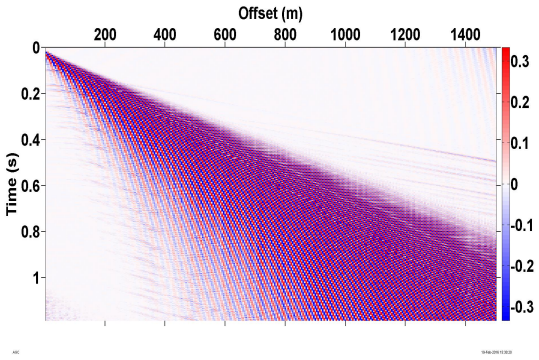

(c) Dataset 2 with flexural noise.

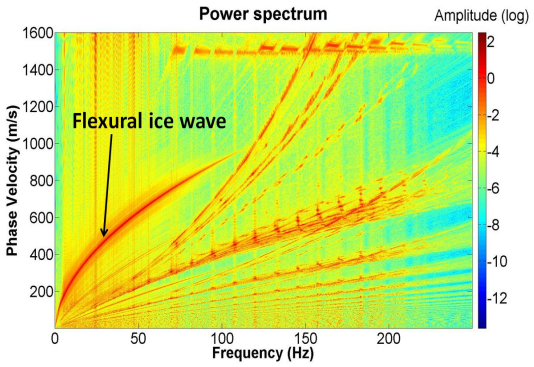

(d) Power spectrum with flexural noise.

Figure 5.29: Dataset 2 before and after added synthetic flexural noise. Notice the dispersion curve for the flexural waves in subfigure (d).

As the receiver spacing here was set to 5 meters, just as in Dataset 1, virtually no aliasing is present in the $f-k$ domain. Thus, a processing work flow utilizing the $f-k$ transform was designed for this dataset given that the processing attempts on Dataset 1 yielded very good results via the $f-k$ transform. The complete work flow for the processing of Dataset 2 using the $f-k$ filter was as follows:

- Transforming the data to $f-k$ domain
- Muting of flexural wave noise in $f-k$ domain
- Transforming the data back to $x-t$ domain and apply AGC-scaling
- RT filtering of high velocity noise ($v \geq 1500$ m/s)
- Predictive deconvolution of dataset for multiple attenuation
- Velocity picking
- NMO-correction

- Muting of low-offset noise in NMO-corrected gather
- Stacking

This processing is presented in figure 5.30. Notice that the flexural wave noise is separated from other events in the $f-k$ domain and may therefore be muted without affecting the reflected signals in the seismogram. The linear events in the $f-k$ spectrum represents the various layer velocities in the dataset whereas the clear non-linear event represents the flexural wave noise. The linear event with reverse slope is most likely an artefact which occurs since the data are synthetic and finite. We further note from figure 5.30d that noise is present at velocities higher than approximately 1500 m/s. RT filtering is effective at attenuation this noise, as can be seen in figure 5.30e. The predictive deconvolution step in the processing does not appear to have much effect, but at larger offset multiples appear to be somewhat attenuated and damped. After velocity analysis and NMO-correction is performed, the reflectors are visible, as can be seen in figures 5.30h and 5.30i. For velocity picking, only the first arrival for any given velocity is picked, as events occurring at later times with regular intervals for the same velocity value most likely represent multiples.

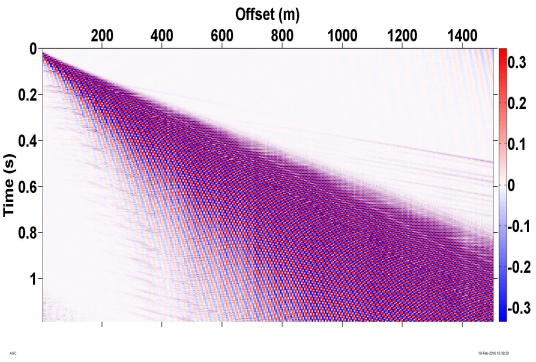

(a) Dataset 2 prior to processing.

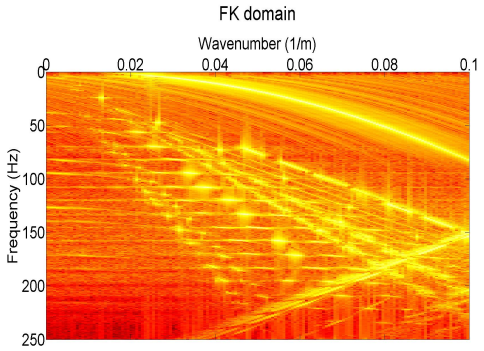

(b) Dataset 2 in the $f-k$ domain.

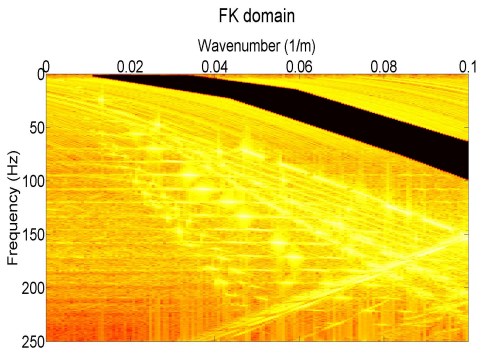

(c) Muting in the $f-k$ domain.

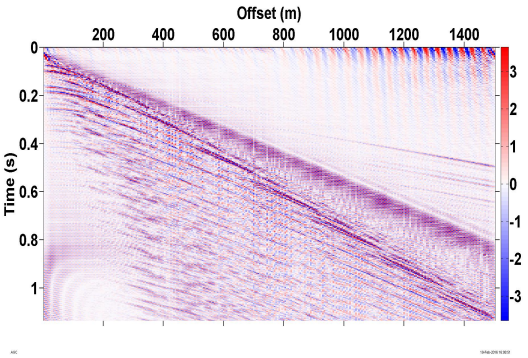

(d) Dataset 2 after $f-k$ filtering and scaling.

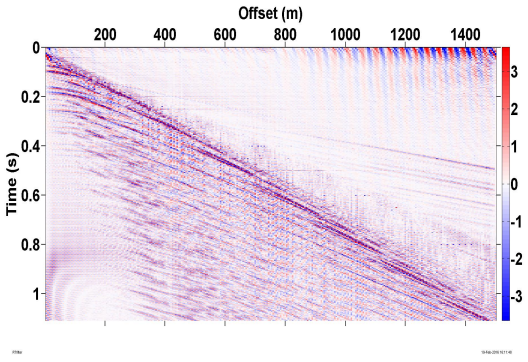

(e) Dataset 2 after RT filtering.

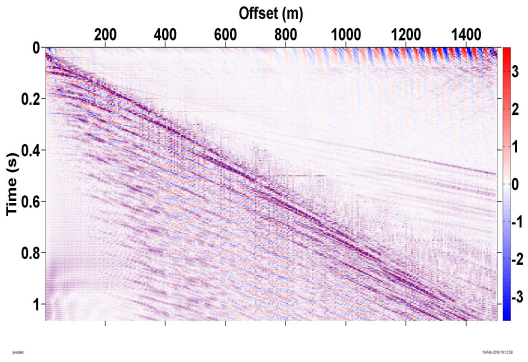

(f) Dataset 2 after predictive deconvolution.

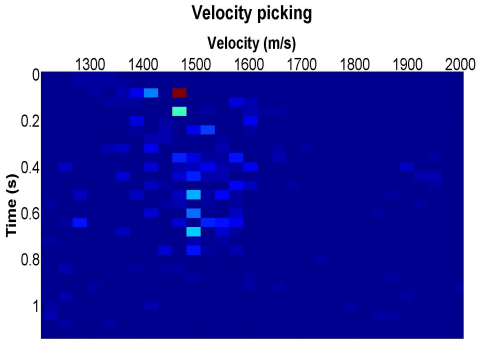

(g) Dataset 2 velocity picking.

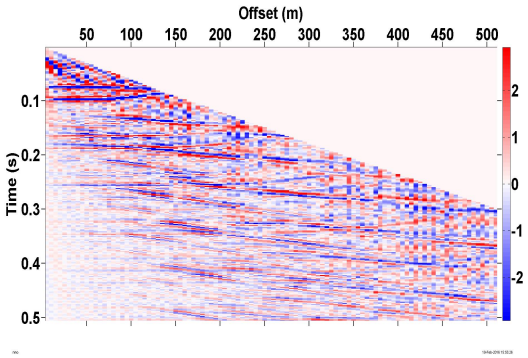

(h) Dataset 2 after NMO-correction.

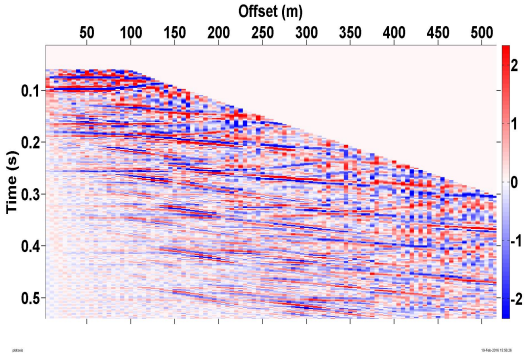

(i) Dataset 2 after NMO-correction and muting.

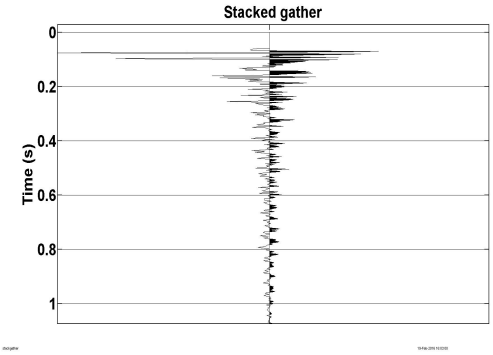

(j) Dataset 2 after stack.

Figure 5.30: Processing work flow for Dataset 2 with $f - k$ filtering.

As we have the raw data without added flexural wave noise for this seismogram available, we may compare the NMO-corrected and stacked raw data to the NMO-corrected and stacked seismogram obtained through the processing work flow presented above. This is done in figure 5.31. Observe that a fairly similar stacked gather is obtained despite the presence of some extra noise on the processed gather. However, as this represents the stacking of just a simple shot gather, we would expect the results to improve more in respect to enhancing the signal-to-noise ratio in a stacked CMP-gather. In conclusion, we obtain very good results using the $f - k$ processing work flow outlined above.

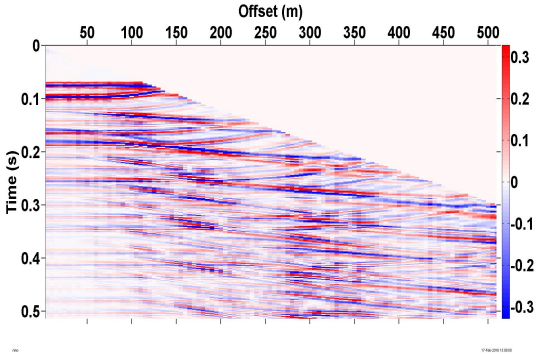

(a) NMO-corrected seismogram prior to noise addition.

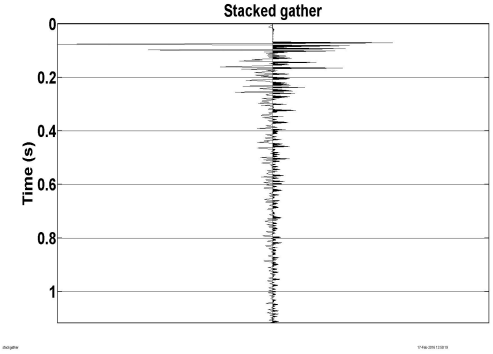

(b) Stacked seismogram prior to noise addition.

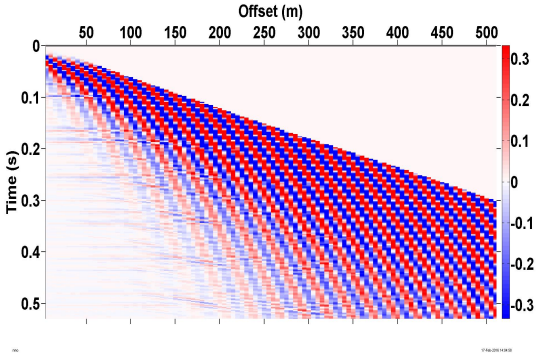

(c) NMO-corrected seismogram after noise addition.

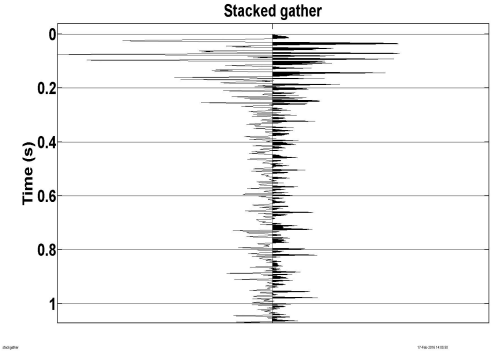

(d) Stacked seismogram after noise addition.

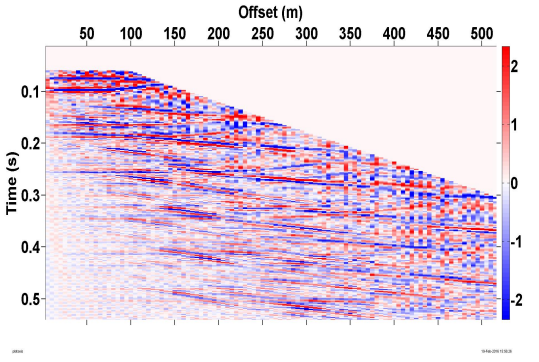

(e) NMO-corrected seismogram after $f-k$ processing.

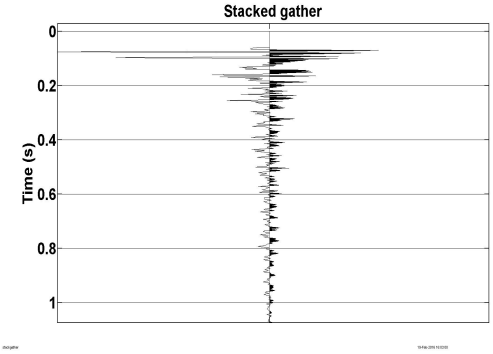

(f) Stacked seismogram after $f-k$ processing.

Figure 5.31: NMO-correction and stacking of Dataset 2 prior to noise addition, after noise addition, and after processing.

5.4 Processing of Dataset 3

Dataset 3, which is a real marine dataset obtained during Svalex 2012 at Van Mijenfjorden, Svalbard, and which served as the model for the synthetic dataset processed in the previous section, was processed subsequent to the adding of synthetic flexural waves as generated

by a point source. Dataset 3 without and with flexural noise is presented in figure 5.32.

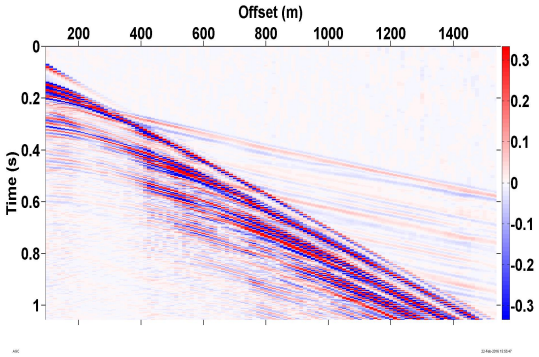

(a) Dataset 3 without flexural noise.

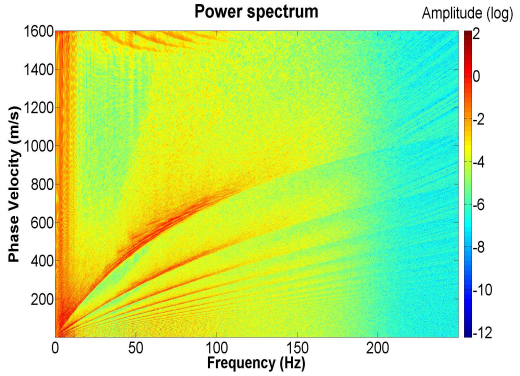

(b) Power spectrum without flexural noise.

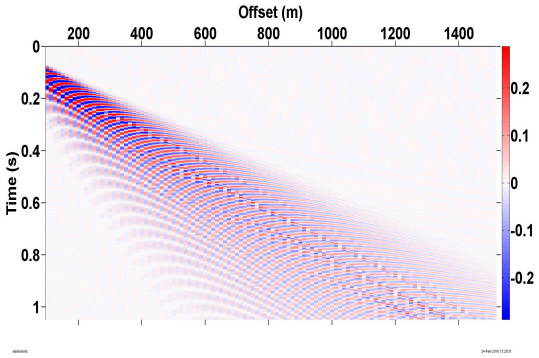

(c) Dataset 3 with flexural noise.

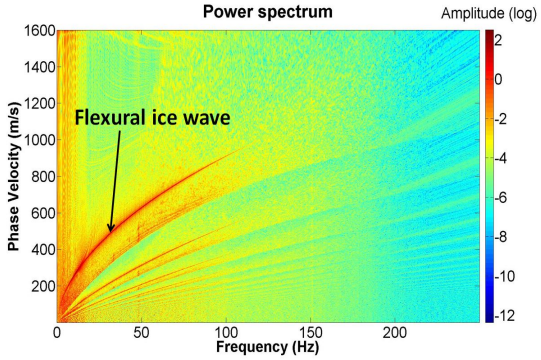

(d) Power spectrum with flexural noise.

Figure 5.32: Dataset 3 before and after added synthetic flexural noise. Notice the dispersion curve and side lobes for the flexural waves in subfigure (d).

An important difference between the synthetic shot gather discussed in the previous section and the real marine shot gather is that the real data were acquired using a receiver spacing of 12.5 meters. As such, conventional $f-k$ filtering does not work for this dataset due to spatial aliasing. This is illustrated in figure 5.33. We see here that we can not identify the dispersion curve for the flexural waves in the $f-k$ domain as the maximum k-value is too small (based on expected values for k as obtained from figure5.32d), thus causing spatial aliasing. As such, even when attempting to mute suspected parts of the $f-k$ spectrum, no discernible results are achieved. Even in the $x-t$ domain prior to processing aliasing is present as the flexural waves appear to be aliased and folded. In such situations, trace interpolation may be used to improve the data, but this was not done here.

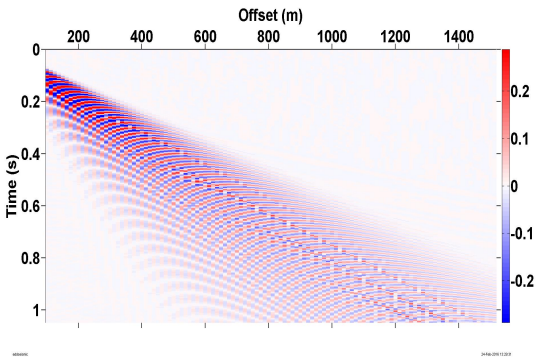

(a) Dataset 3 prior to filtering.

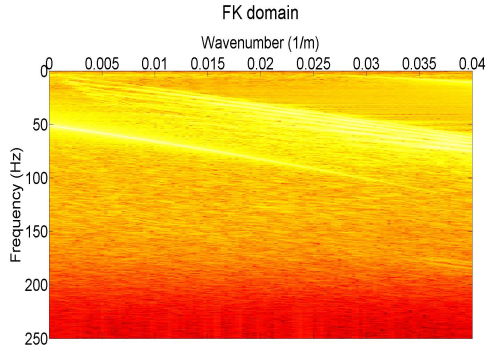

(b) Dataset 3 in the $f-k$ domain.

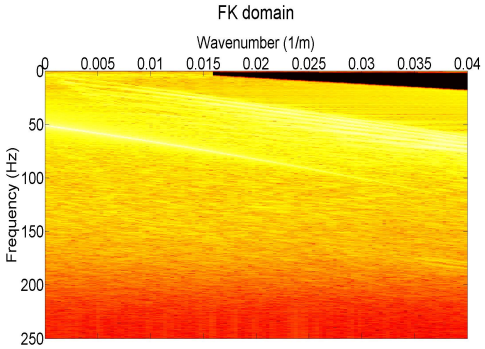

(c) Muting in the $f-k$ domain.

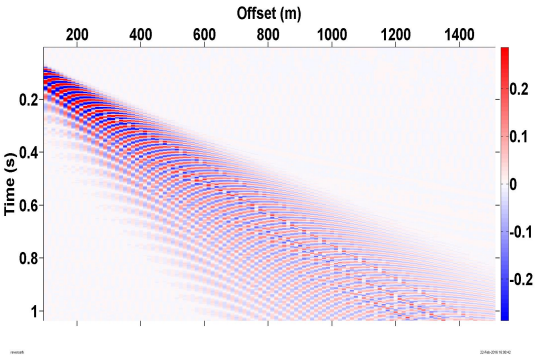

(d) Dataset 3 after attempted $f-k$ filtering.

Figure 5.33: Dataset 3 before and after attempted $f-k$ filtering. The dispersion curve is not easily identifiable in the $f-k$ domain, and even after muting the suspected part of the dataset, flexural wave noise remains.

Attempts to process the dataset via $\tau-p$ filtering was also attempted, but poor results were achieved due to aliasing effects and smearing, again most likely caused by the large receiver interval. The immediate result following a $\tau-p$ filtering attempt with $p \in \{0, 1/1350\}$ and spiking deconvolution is presented in figure 5.34.

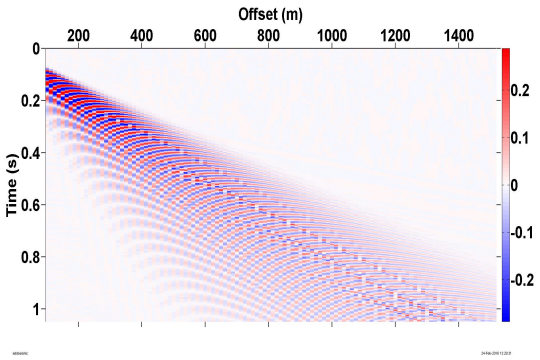

(a) Dataset 3 prior to filtering.

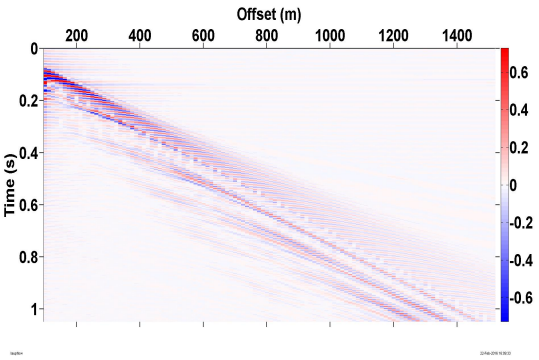

(b) Dataset 3 after $\tau-p$ filtering.

Figure 5.34: Dataset 3 before and after attempted $\tau-k$ filtering with spiking deconvolution. Quite a lot of remnant noise and aliasing effects are present.

The processing of Dataset 3 thus primarily utilized the RT transform to achieve flexural wave noise removal. The utilization of $\tau - p$ filtering subsequent to RT filtering was, however, performed to attenuate remaining noise events. The complete work flow for processing of Dataset 3 was as follows:

- RT filtering with velocity interval defined as $v \in \{1, 2500\}$ with spectral clipping threshold equal to 10 times the median value
- Muting of flexural wave noise in $\tau - p$ domain with $p \in \{0, 1/1350\}$
- Spiking deconvolution in $\tau - p$ domain
- Transforming the data back to $x - t$ domain and apply AGC-scaling
- Predictive deconvolution of dataset for multiple attenuation
- Muting of noise and artefacts
- Velocity picking
- NMO-correction
- Stacking

An illustration of this processing approach is presented in figure 5.35. From the illustration we see that subsequent to RT filtering, $\tau - p$ filtering and AGC-scaling, quite a lot of noise and artefacts are present at large offsets in the seismic data. A simple mute was applied to effectively remove this noise. Note also that some horizontal noise artefacts are present after RT filtering. This is most likely caused by slightly inaccurate discrete sampling along the radial traces causing some points to be omitted in each captured radial trace. From the NMO-corrected data we see that some reflectors are now visible, such as the reflector located at approximately $TWT = 0.2$ seconds.

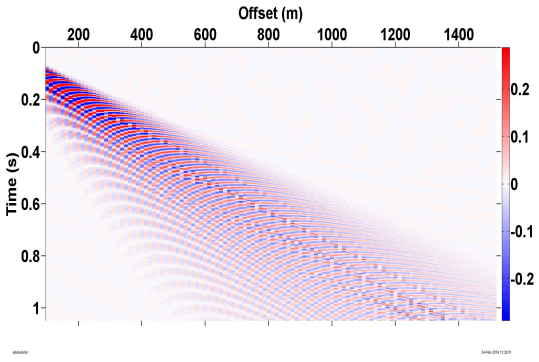

(a) Dataset 3 prior to processing.

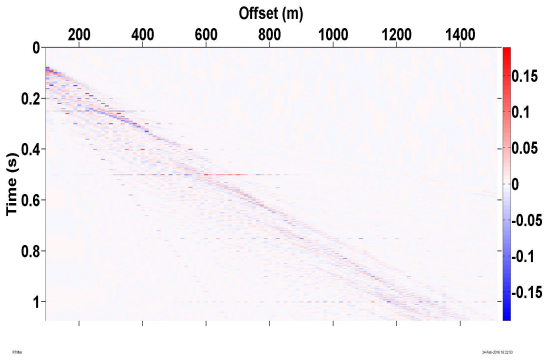

(b) Dataset 3 after RT filtering.

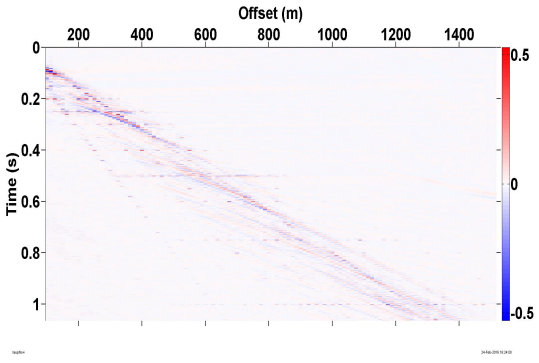

(c) Dataset 3 after $\tau - p$ filtering and spiking deconvolution.

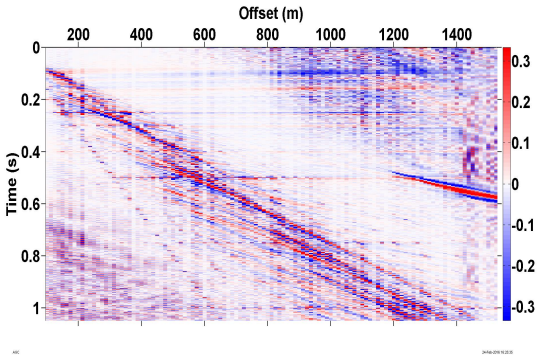

(d) Dataset 3 after AGC-scaling.

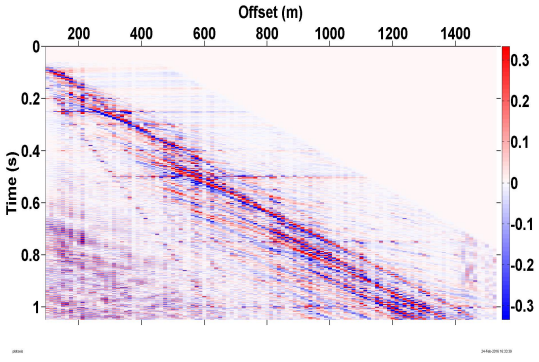

(e) Dataset 3 after muting of noise and artefacts.

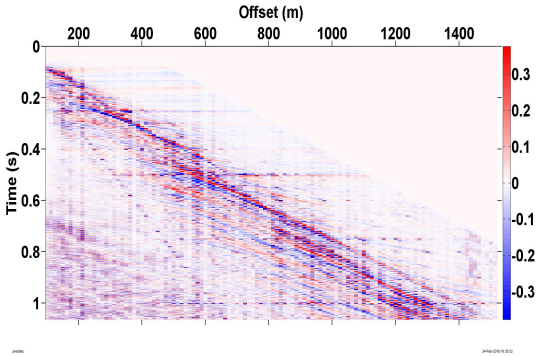

(f) Dataset 3 after predictive deconvolution.

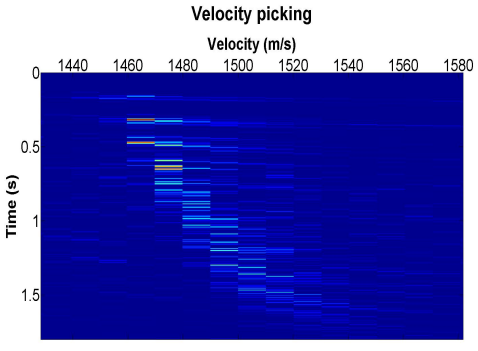

(g) Dataset 3 velocity picking.

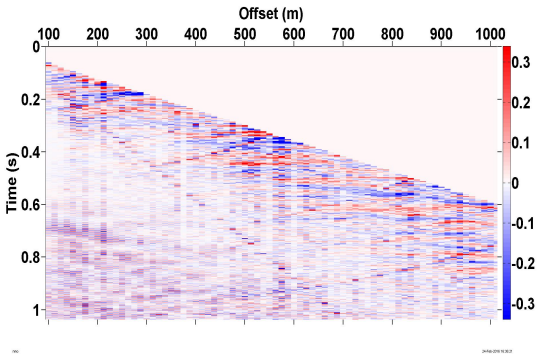

(h) Dataset 3 after NMO-correction.

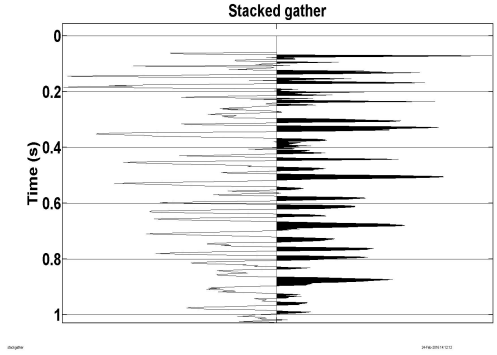

(i) Dataset 3 after stack.

Figure 5.35: Processing work flow for Dataset 3.

A comparison between the NMO-corrected original data with the processed data is presented in figure 5.36. From the figure we see that although a lot of the flexural wave noise has been removed from the data and reflectors are now visible (such as the event located at approximately $TWT = 0.2$ seconds), the processed dataset is nevertheless plagued with quite a bit of noise and apparent phase shifts. As such, other unconventional processing methods may yield better results here, but this was nevertheless the best result achieved through multiple attempts at combining of the $f - k$ method, $\tau - p$ method and RT method. The relatively poor results achieved when processing Dataset 3 is most likely related to the fact that the receiver interval was 12.5 meters, thus causing quite a lot of spatial aliasing. Again, however, it should be noted that as this only represents a single shot gather, better results would likely be achieved when stacking multiple shot gathers to a CMP-gather as much of the remnant noise would then cancel out through destructive interference. This is reasonable to assume given the fact that the reflectors are, after all, visible in the NMO-corrected and stacked processed gather.

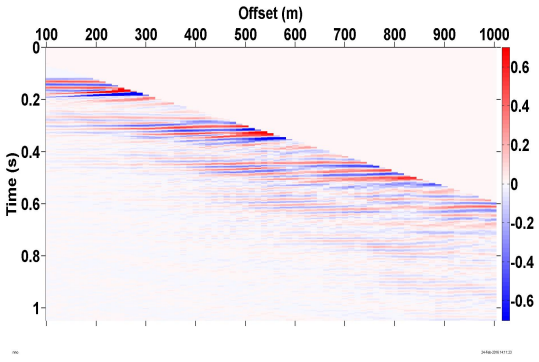

(a) NMO-corrected seismogram prior to noise addition.

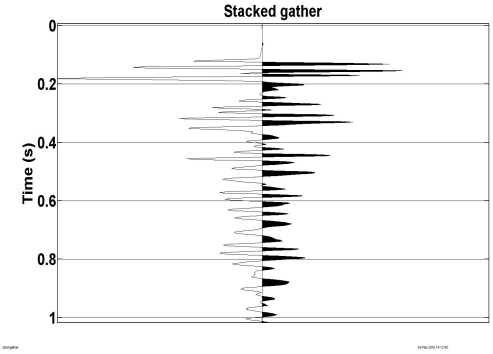

(b) Stacked seismogram prior to noise addition.

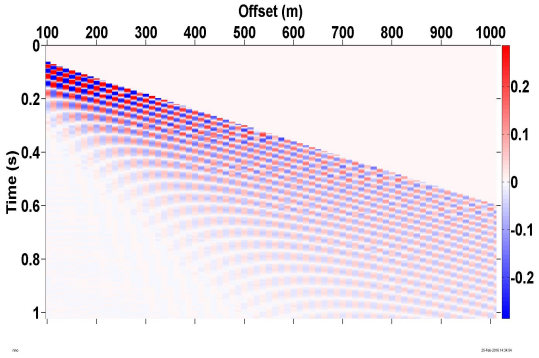

(c) NMO-corrected seismogram after noise addition.

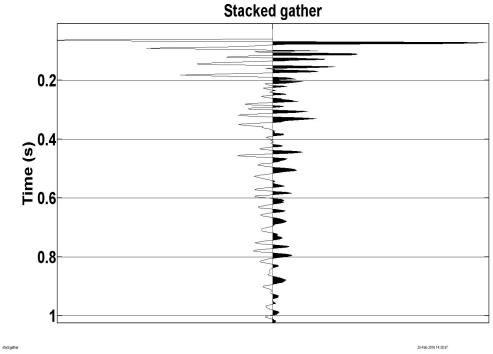

(d) Stacked seismogram after noise addition.

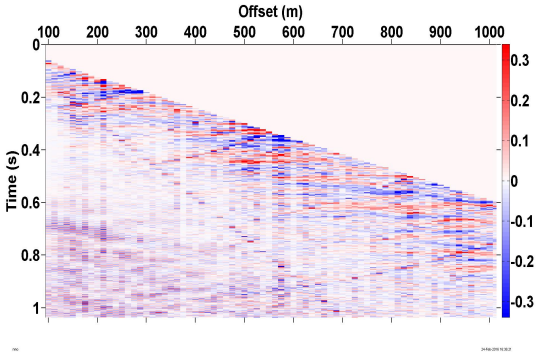

(e) NMO-corrected seismogram after processing.

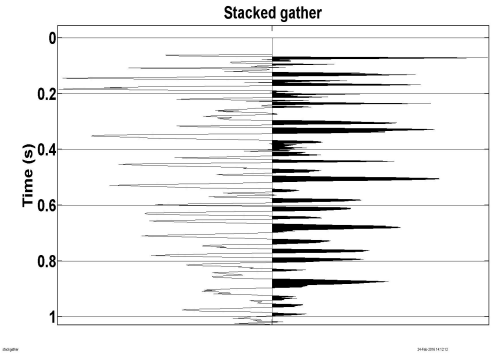

(f) Stacked seismogram after processing.

Figure 5.36: NMO-correction and stacking of Dataset 3 prior to noise addition, after noise addition, and after processing.

5.5 Processing of Dataset 4

Dataset 4, a synthetic shot gather generated from full-waveform modelling assuming a viscoelastic medium, was generated on the basis of a real shot gather obtained on sea ice

near Sveagruva, Svalbard in 2013. As this model assumes sea ice conditions, flexural waves are present on the dataset. The scaled shot gather and its power spectrum are presented in figure 5.37. From the figure we notice that the flexural waves are present, but at a much smaller velocity range than in Datasets 1-3 where the flexural waves were added synthetically to already existing shot gathers. Flexural waves only appear to be present at velocities below approximately 350 m/s, and this is also confirmed via the interpreted dispersion curve observed in the power spectrum. The reason for this low velocity range is probably the result of two factors. One factor is that whereas in the modelling performed using the thin plate theory as presented in Yang and Yates (1995) assumes vacuum above the plate, air is here considered present. This is also evident though the presence of a high-amplitude air wave propagating with a velocity of approximately 330 m/s as seen in figure 5.37a. As such, flexural waves propagating close to this velocity will radiate energy into the air, just as flexural waves propagating with velocities close to the wave velocity in water will radiate energy into the water, thus causing dispersion to dampen. In addition, as the dataset is based on a viscoelastic medium, more anisotropy in the ice may cause more effective attenuation of high-frequency events.

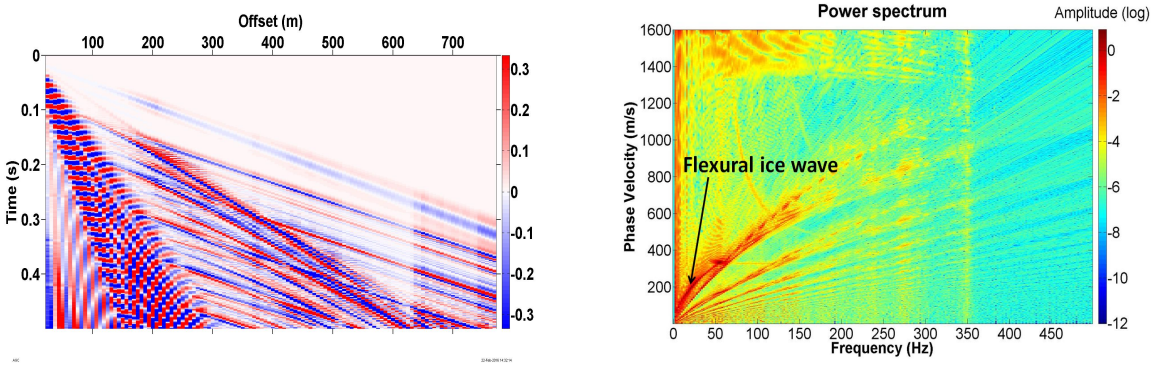

(a) Dataset 4. **(b)** Power spectrum of Dataset 4.

Figure 5.37: Dataset 4 prior to processing and its power spectrum.

As the receiver spacing was set to 6.25 meters for this dataset, $f-k$ filtering again proves to have little effect on flexural ice wave removal. This is illustrated in figure 5.38. We see that although some damping of the flexural waves is evident at low velocities, the noise is still clearly present and no information hidden behind the flexural wave noise becomes visible.

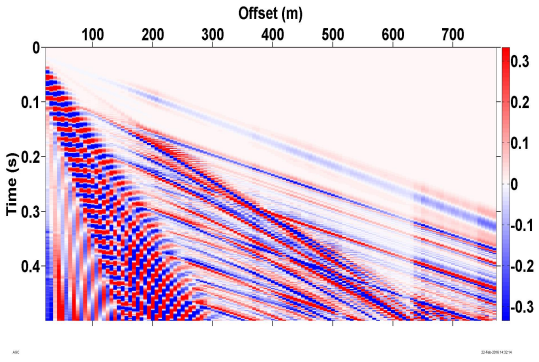

(a) Dataset 4 prior to filtering.

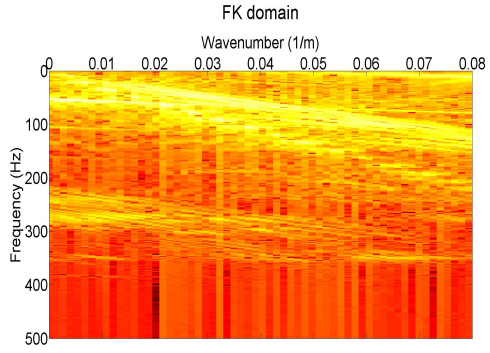

(b) Dataset 4 in the $f-k$ domain.

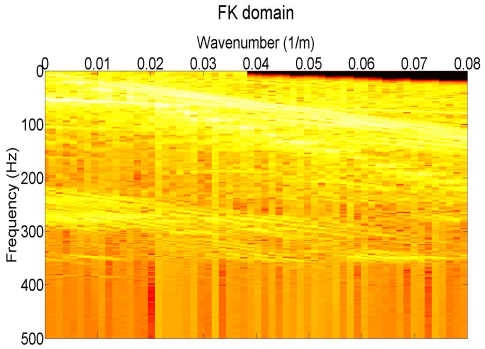

(c) Muting in the $f-k$ domain.

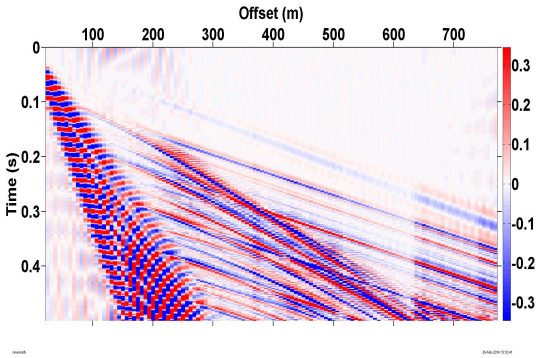

(d) Dataset 4 after attempted $f-k$ filtering.

Figure 5.38: Dataset 4 before and after attempted $f-k$ filtering. The dispersion curve is not easily identifiable in the $f-k$ domain, and even after muting the suspected part of the dataset, flexural wave noise remains.

As the velocity interval of the flexural waves are limited to velocities below approximately $v = 350$ m/s, however, it is quite reasonable to assume that the flexural wave velocities are quite a bit lower than the P-wave velocities in the subsurface layers. Due to this separation of flexural wave velocities and layer velocities, a processing approach utilizing primarily $\tau - p$ filtering was designed as this allows for simple separation of velocity intervals based on the defined slowness interval input. By selecting $p \in \{0, 1/1350\}$, all velocities below 1350 m/s are effectively muted. As such, the following work flow was implemented for processing of Dataset 4:

- Muting of flexural wave noise in $\tau - p$ domain with $p \in \{0, 1/1350\}$
- Spiking deconvolution in $\tau - p$ domain
- Transforming the data back to $x - t$ domain and apply scaling.
- Muting of air wave

- RT filtering of high velocity noise events and artefacts ($v \geq 1500$ m/s)
- Predictive deconvolution of dataset for multiple attenuation
- Velocity picking
- NMO-correction
- Stacking

The processing approach is illustrated in figure 5.39.

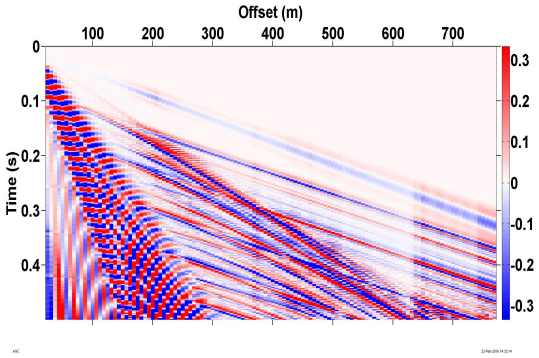

(a) Dataset 4 prior to processing.

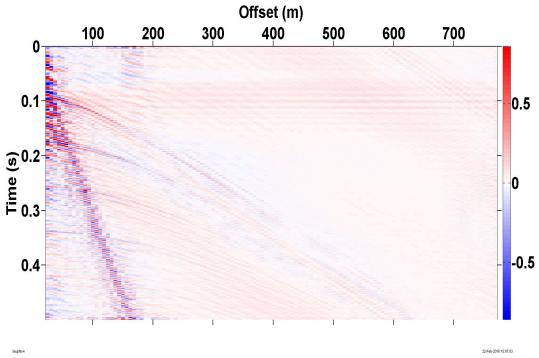

(b) Dataset 4 after $\tau - p$ filtering and spiking deconvolution.

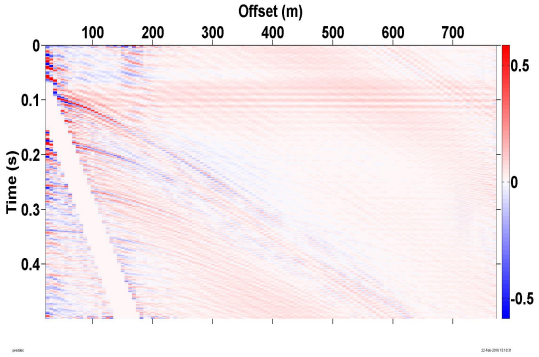

(c) Dataset 4 after muting of air wave.

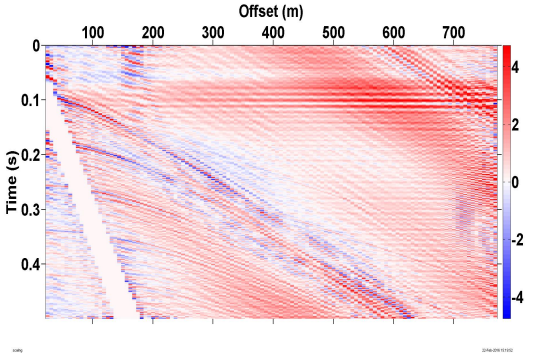

(d) Dataset 4 after scaling.

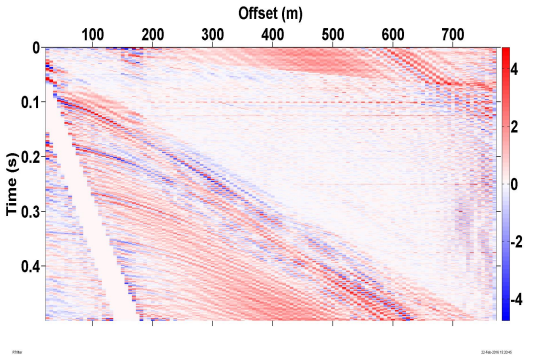

(e) Dataset 4 after RT filtering.

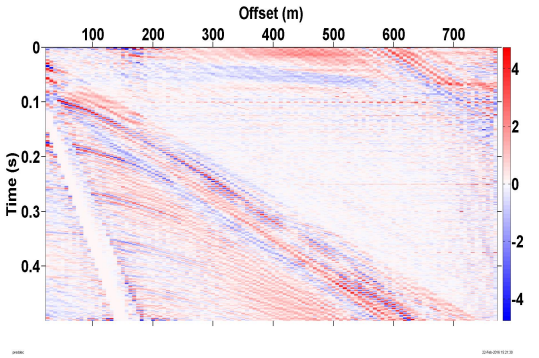

(f) Dataset 4 after predictive deconvolution.

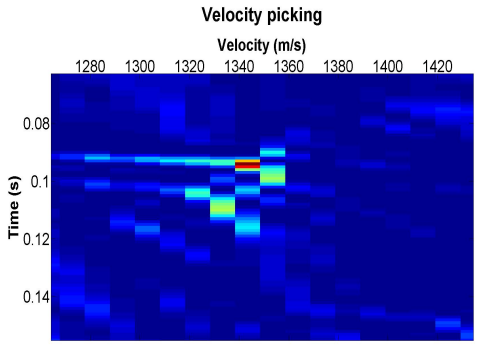

(g) Dataset 4 velocity picking.

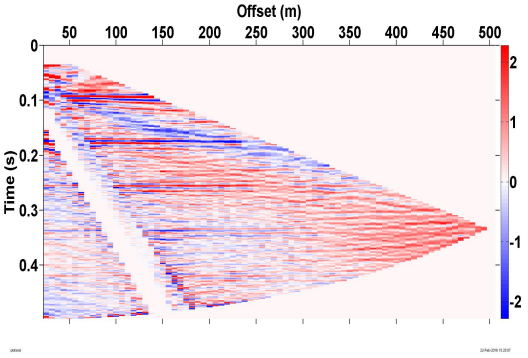

(h) Dataset 4 after NMO-correction.

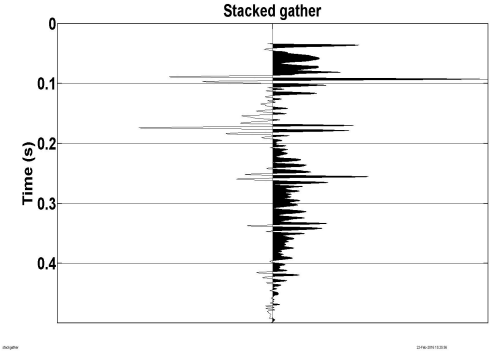

(i) Dataset 4 after stack.

Figure 5.39: Processing work flow for Dataset 4.

Comparing the NMO-corrected and stacked gathers obtained from the original data versus the processed data, we clearly see an improvement subsequent to processing. This is illustrated in figure 5.40. We see that, except for the muted part of the gather where the air wave was dominating, signals previously obscured by flexural wave noise are now greatly enhanced. Note in particular the reflection event at approximately $TWT = 0.1$ seconds which is not easily identifiable in the original stacked gather, but which dominates the stacked processed seismogram.

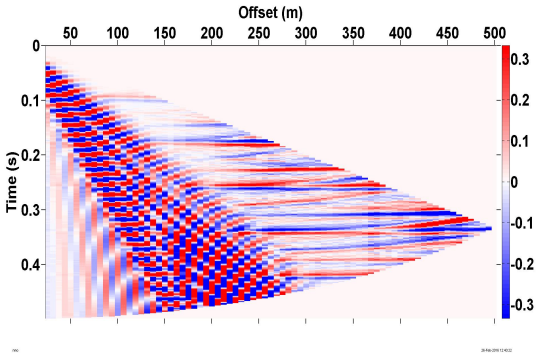

(a) NMO-corrected seismogram prior to filtering.

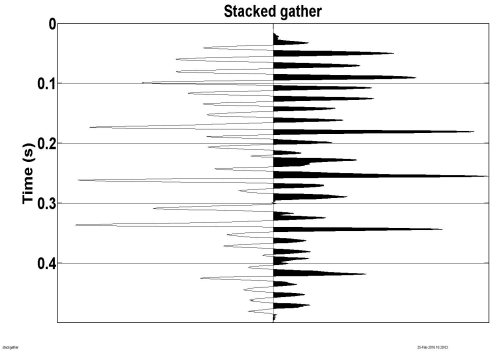

(b) Stacked seismogram prior to filtering.

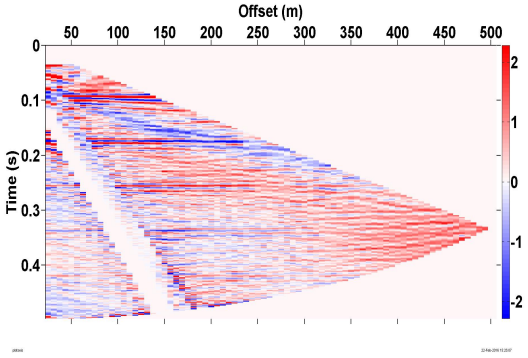

(c) NMO-corrected seismogram after processing.

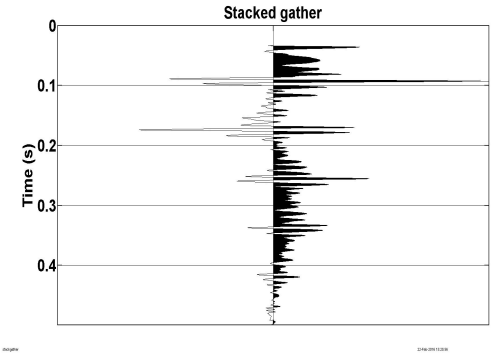

(d) Stacked seismogram after processing.

Figure 5.40: NMO-correction and stacking of Dataset 4 prior to processing and after processing.

5.6 Processing of Dataset 5

Dataset 5, a real dataset obtained on sea ice at Van Mijenfjorden near Sveagruva, Svalbard in 2013, and which served as the model for the synthetic dataset processed in the previous section, was processed in almost the exact same manner as Dataset 4. As the two datasets have the same receiver spacing (6.25 meters), and almost the exact same flexural wave dispersion, virtually the same processing procedure was implemented successfully. Dataset 5 and its interpreted dispersion relation estimated from the power spectrum are presented in figure 5.41. Note how the flexural wave is only present a low velocities. In the power spectrum we can also see the air wave which is propagating with approximately 330 m/s. As noted in Section 4.3.5, the white vertical lines in the seismogram most likely represent malfunctioning geophones.

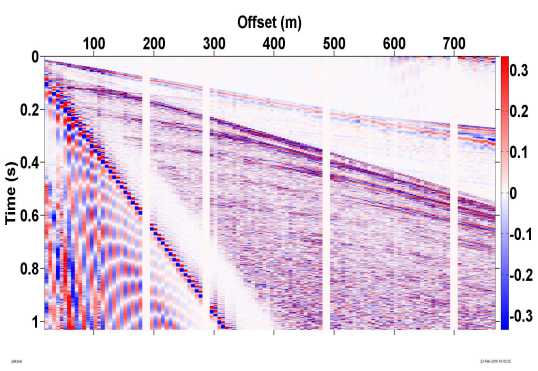

(a) Dataset 5.

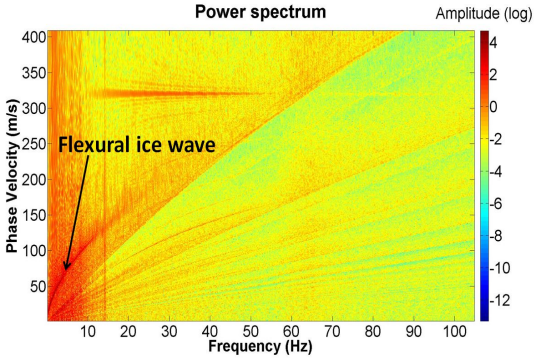

(b) Power spectrum of Dataset 5.

Figure 5.41: Dataset 5 prior to processing and its power spectrum.

As with Datasets 3 and 4, $f-k$ filtering is not effective in this case either. This is illustrated in figure 5.42. Although the flexural waves are slightly damped, very little filtering is achieved, and there are also major aliasing effects all over the seismic data.

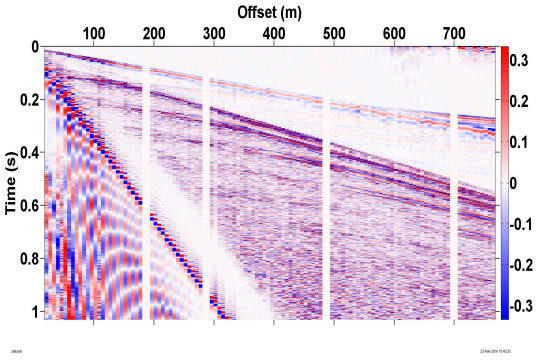

(a) Dataset 5 prior to filtering.

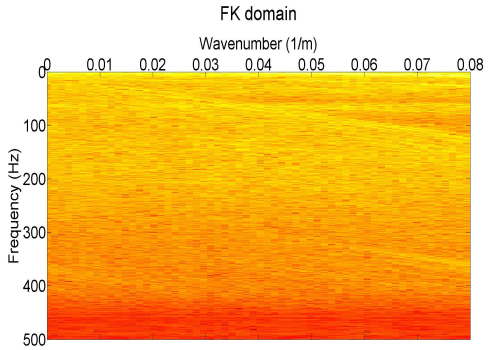

(b) Dataset 5 in the $f-k$ domain.

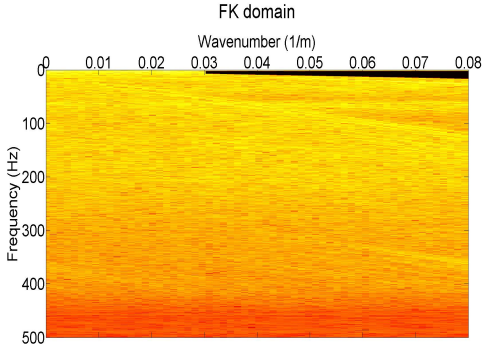

(c) Muting in the $f-k$ domain.

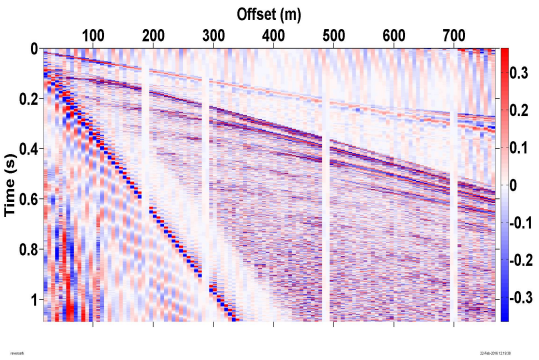

(d) Dataset 5 after attempted $f-k$ filtering.

Figure 5.42: Dataset 5 before and after attempted $f-k$ filtering. The dispersion curve is not easily identifiable in the $f-k$ domain, and even after muting the suspected part of the dataset, flexural wave noise remains.

The processing work flow for Dataset 5 consisted of the following steps:

- Muting of air wave
- Muting of flexural wave noise and spiking deconvolution in $\tau - p$ domain with $p \in \{0, 1/1350\}$
- Transforming the data back to $x - t$ domain and perform scaling.
- RT filtering of high velocity noise events and artefacts ($v \geq 1500$ m/s)
- Predictive deconvolution of the dataset for multiple attenuation
- Velocity picking
- NMO-correction
- Stacking

The processing is illustrated in figure 5.43. From the illustration we see that we obtain a result which is in fairly high agreement with the results obtained for Dataset 4. The reflector at approximately $TWT = 0.1$ seconds is now visible, and seismic data previously obscured by flexural wave noise can now be seen. The NMO-corrected and stacked datasets obtained prior to, and subsequent to, processing are presented in figure 5.44. Notice that the flexural waves are not too problematic in the shot gather due to their presence at low velocities only, but the processing nevertheless enhances the signal-to-noise ratio and thus effectively attenuates much of the flexural wave noise.

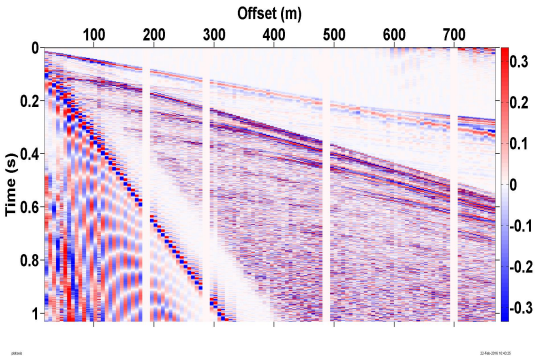

(a) Dataset 5 prior to processing.

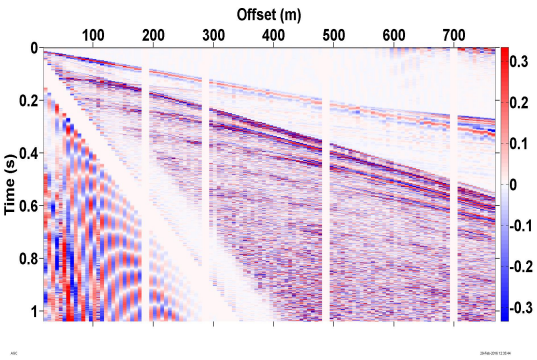

(b) Dataset 5 after muting of air wave.

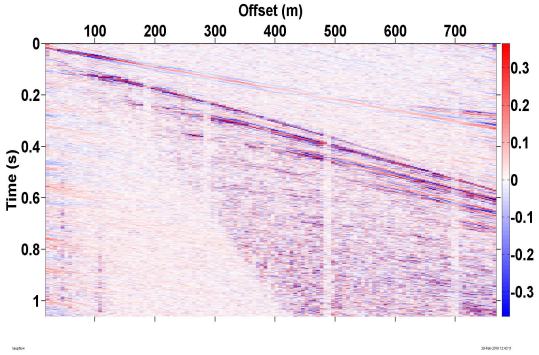

(c) Dataset 5 after $\tau - p$ filtering and spiking deconvolution.

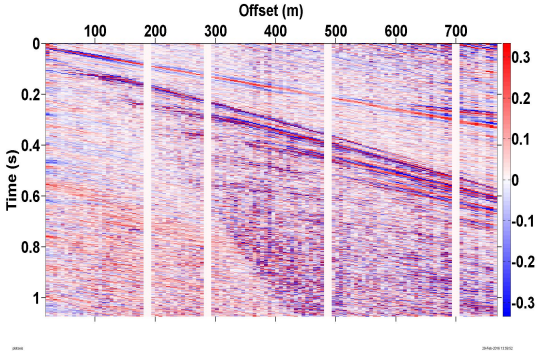

(d) Dataset 5 after scaling.

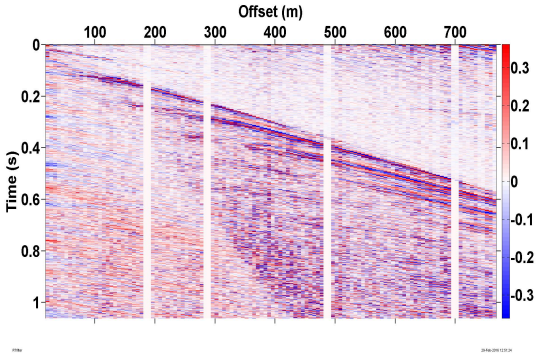

(e) Dataset 5 after RT filtering.

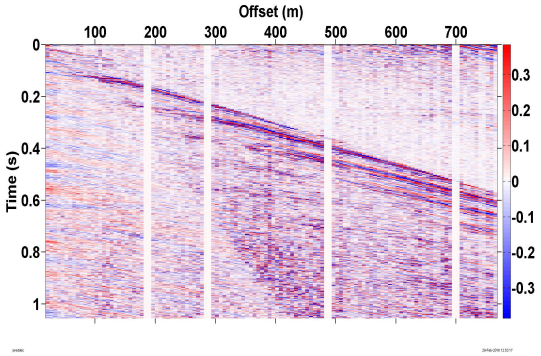

(f) Dataset 5 after predictive deconvolution.

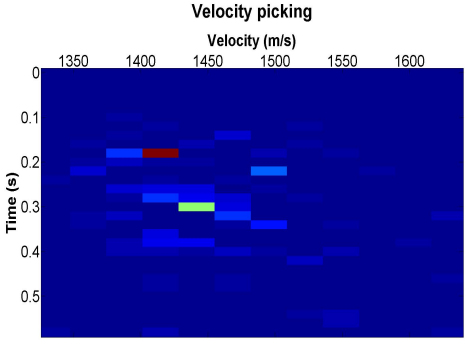

(g) Dataset 5 velocity picking.

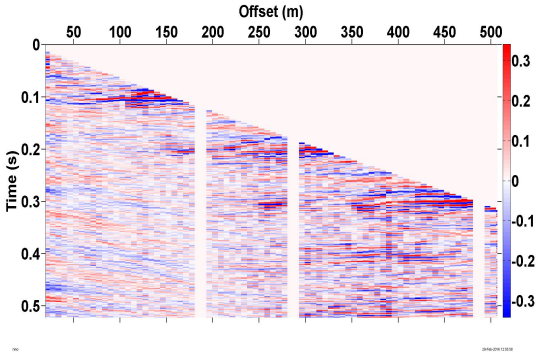

(h) Dataset 5 after NMO-correction.

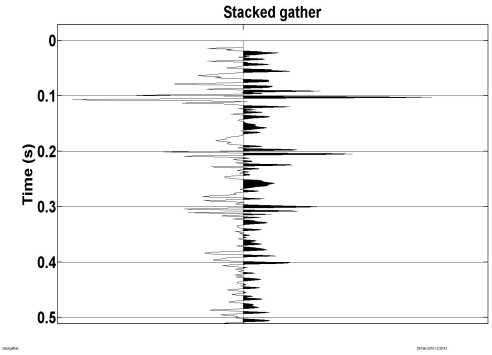

(i) Dataset 5 after stack.

Figure 5.43: Processing work flow for Dataset 5.

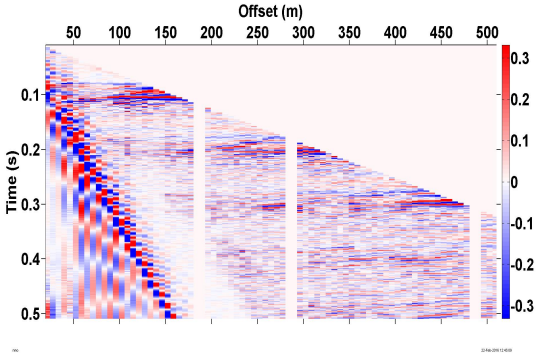

(a) NMO-corrected seismogram prior to processing.

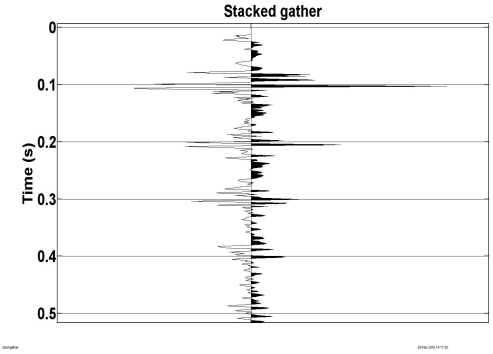

(b) Stacked seismogram prior to processing.

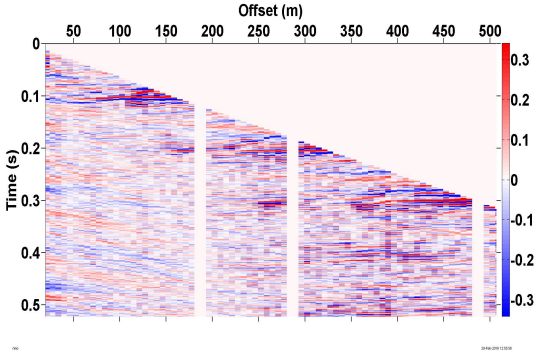

(c) NMO-corrected seismogram after processing.

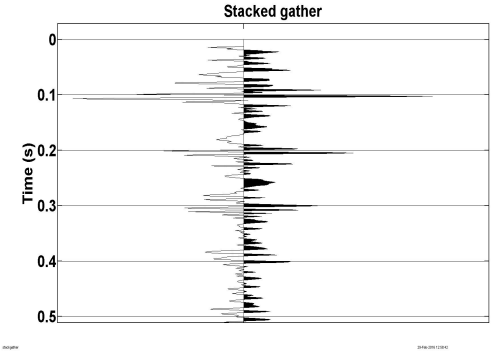

(d) Stacked seismogram after processing.

Figure 5.44: NMO-correction and stacking of Dataset 5 prior to processing and after processing.

5.7 Summary of results

This chapter has illustrated how flexural wave dispersion and flexural wave displacement may be modelled via the fluid-loaded thin plate theory outlined in Yang and Yates (1995), and also how parameters such as ice temperature and ice thickness may influence the dispersion relations. It is clear that low temperature, or high ice thickness, lead to higher velocities at low frequencies and a smaller bandwidth of flexural wave dispersion.

Through the processing of five datasets, it has further been illustrated how different processing methods, or a combination of these methods, may be used to obtain improved results when processing data obscured by flexural wave noise. Parameters such as receiver spacing, ice conditions and the flexural wave noise bandwidth (which is directly related to velocity range) all affect how flexural wave noise manifests itself on seismic data, and, subsequently, influences which processing approach will yield the best results.

Chapter 6

Discussion and Conclusions

Having now presented the theory, methods and some results, a brief discussion will follow. The discussion aims to highlight the principle findings, and also evaluate the results in terms of their quality and usefulness. Suggestions will also be offered for future research which may improve further upon the obtained results.

6.1 Discussion

Using the fluid-loaded thin plate theory as outlined in Yang and Yates (1995), flexural ice waves were modelled. The implementation of the relevant equations for wave displacement (line source and point source) yielded dispersive waves with the higher frequency components travelling at faster phase velocities than lower-frequency components. This is in concurrence with the theory outlined in Ewing and Crary (1934), Press and Ewing (1951b), and Press and Ewing (1951a) as well as other modelling attempts presented in various literature, e.g. Rendleman and Levin (1990); Del Molino et al. (2008); Rovetta et al. (2009).

In order to investigate the nature of the dispersion relation, the theories of Langleben and Pounder (1963), Cox and Weeks (1974), Cox and Weeks (1983) and Weeks and Assur (2009) were included in order to study how ice temperature and ice thickness affect the dispersion relation. The results reveal that a decrease in temperature results in higher phase- and group velocities at low frequencies, but at higher frequencies the group velocities in the warmer ice plates will be the highest (see figures 5.9, 5.10, 5.11 and 5.12). This may be obvious from the formula linking phase- and group velocity (equation 2.17) in that the group velocity will converge to the phase velocity as the frequency increases,

and this occurs at lower frequencies in the colder ice plates than in the warmer ice plates. The fact that the phase velocity increases with decreasing temperature follows from the fact that a decrease in temperature will lead to an increase in the elastic moduli of the ice. There is an increase in phase velocity as the ice temperature drops from $-2°$C to $-4°$C, but further drops in temperature have very little effect on the phase velocity. The explanation for this is that ice tends to be slushy and pore water may begin to melt as the ice temperature approaches $0°$C, but once the ice is frozen, any further decrease in temperature will have virtually no effect on the elastic moduli.

By further modelling the effects of ice thickness on the dispersion relation, it was shown that an increase in ice thickness leads to higher phase- and group velocities at low frequencies, but at higher frequencies the group velocities will be highest for the ice layers with the lowest thickness values (see figures 5.13, 5.14 and 5.15). This also follows from equation 2.17, and the overall effect of ice thickness on the dispersion relation is to affect the bending stiffness (equation 2.29). An issue that must be kept in mind, however, is that the fluid-loaded thin plate theory assumes that the ice thickness is very small compared to the wavelength. From plotting velocity as a function of frequency it is easy to estimate the wavelength at each point via equation 2.1. As we plot how the dispersion varies with ice thickness, we should, in theory, only consider the results to be valid at points where the ice thickness is less than one quarter of the wavelength. If we look at figure 5.13a, we can consider the dispersion curve corresponding to an ice thickness equal to 1 meter. At a frequency of 100 Hz, the velocity is approximately 550 m/s. From this we obtain the wavelength $\lambda = 5.5$ meters, and we then see that $\lambda/4 \approx 1.38$. This value is larger than the ice thickness, so we may therefore assume the estimated dispersion to be valid at this point. However, if we consider the same curve at a frequency value of 300 Hz, we obtain a velocity value of approximately 990 m/s. We now obtain $\lambda = 3.3$ meters, and $\lambda/4 \approx 0.83$ meters. Since this value is lower than the ice thickness, the estimated dispersion relation may not be entirely valid for this frequency value.

Nevertheless, the results obtained show the relative behavior of the dispersion relation as the various input parameters of temperature and ice thickness varies, and the results are in concurrence with similar results obtained elsewhere (see Shei et al. (1983), Hunkins (1995) and Bakke (2015)). However, at this point it may be interesting to discuss how *accurate* the modelled dispersion relation results are. Even though the modelled results

accurately reveal the general *trend* of the dispersion curve as function of ice temperature and ice thickness, the goal should be to obtain results which are applicable to real data. If a very accurate dispersion relation curve may be obtained for a seismic dataset, filters may potentially be developed based on the dispersion relation by subsequently modelling flexural waves which then may be subtracted from the seismic dataset and, in theory, remove the flexural ice wave noise. Such an approach is presented in Rovetta et al. (2009). Thus, we may, for instance, compare modelled dispersion relation curves to the dispersion relation for Dataset 5, which is the only real dataset featuring flexural ice waves. The data presented in Dataset 5 were obtained on sea ice with an ice thickness of approximately 0.8 meters. The air temperature was approximately $-10°$C during the survey, and it may be reasonable to assume that the ice temperature was somewhat lower than this. By comparing the interpreted dispersion relation from the power spectrum for Dataset 5 with the dispersion relation obtained from running the MATLAB program which estimates dispersion relation curves as function of ice temperature with ice thickness set to 0.8 meters, we obtain the results presented in figure 6.1. From the figure we see that the modelled dispersion relation curve which most accurately matches the real dispersion curve in the power spectrum is the curve obtained for an ice temperature of $-2°$C. As the ice temperature most likely was quite a bit lower than this, we must conclude that the modelled results do not match the real-world dispersion perfectly. The primary reason for this discrepancy most likely stems from inhomogeneity in the real ice. Whereas the modelled dispersion relation assumes a constant thickness with isotropic ice, real-world ice may have varying ice thickness, cracks and anisotropy. As such, modelled results will tend to show higher velocities for a given ice temperature and ice thickness than real-world data (see Oliver et al. (1954) and Hunkins (1995)). In order to compensate for this, a lower thickness value may be used for modelling purposes. If we, for instance, assume an ice thickness equal to 0.5 meters, and compare this to the real dispersion, we obtain a much more accurate result, and this is presented in figure 6.2. Assuming that the ice temperature was somewhere between $-10°$C and $-15°$C, we can now see that the expected phase velocity from our modelling is closer to the actual phase velocity, even though the modelled velocity is still slightly higher.

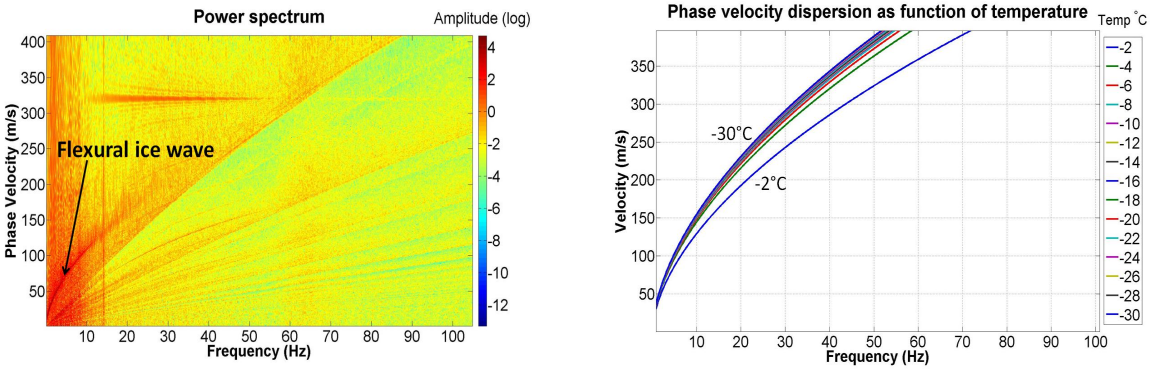

(a) Power spectrum for Dataset 5. **(b)** Modelled dispersion relation

Figure 6.1: Power spectrum for Dataset 5 and modelled dispersion relation as function of temperature with ice thickness equal to 0.8 meters.

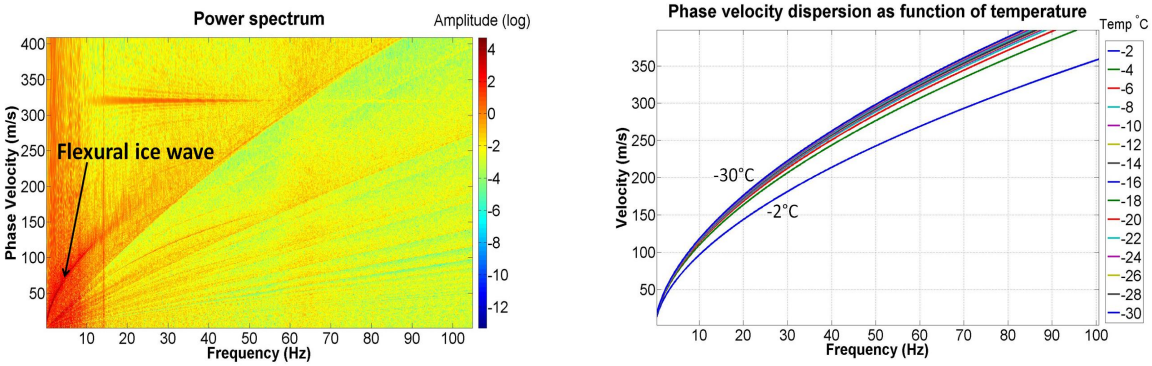

(a) Power spectrum for Dataset 5. **(b)** Modelled dispersion relation

Figure 6.2: Power spectrum for Dataset 5 and modelled dispersion relation as function of temperature with ice thickness equal to 0.5 meters.

There are, of course, other parameters that so far have not been taken into account during the dispersion relation modelling. The most obvious one is the negligence of air pressure above the ice plate. By omitting the air and assuming a vacuum above the ice plate, realistic conditions are not fully modelled, and more accurate dispersion relation curves will be obtained if the complex transmission coefficients between the ice/air and ice/water interfaces are taken into account (Rovetta et al., 2009). Further, the effects of ice temperature on Young's Modulus and the Poisson's ratio, as found via equations 2.48 and 2.49, are primarily based on empirical models which may not be fully applicable in more complex situations. As such, the modelling performed in this study may serve as a starting point for dispersion relation estimation of flexural ice waves, but more parameters should be taken into account if dispersion relation based filters are to be designed for flexural ice wave processing. The equation for estimating ice salinity (equation 2.47) is also empirical, and may as such not realistically model ice salinities in all geographic

locations. A potential future research topic which may build upon the results achieved in this thesis will therefore be to include more parameters in the modelling work and, if results are in great concurrence with real data, attempt to design dispersion relation based processing filters for flexural ice wave removal. This will connect the modelling and processing work in regards to flexural ice waves more than what has been possible to achieve within the scope of this study.

Regarding the processing performed, the results in Chapter 5 reveal that not one single processing approach is guaranteed to work every time, and a processing approach which works very well on one seismic dataset may be virtually useless on another. The most important parameter in regards to flexibility in the choice of processing method appears to be the receiver spacing, as spatial aliasing may cause problems when performing both $f-k$ filtering and $\tau-p$ filtering. This is evident through equations 3.3, 3.13 and 3.14. If spatial aliasing can be avoided, or at least severely reduced, $f-k$ filtering was proven to be very efficient. A proper modelling of the dispersion relation of the flexural ice waves may in this case be helpful. An accurate dispersion relation will provide information about the frequency bandwidth of the flexural wave, and, from the relation $k = \omega/v_p$, the wave number interval may also be quantified. Through formula 3.3 and the formula for the spatial Nyquist frequency, information may be obtained as to which receiver spacing would be sufficient to avoid large spatial aliasing effects. Although logistically more challenging, a potential strategy could be, if a seismic survey is done from land and out to sea on top of sea ice, to use denser receiver spacing in the transition zone than on other parts of the seismic line. This could make seismic processing of flexural ice waves far easier as it would then be possible to use conventional processing approaches that are easy to implement and included in most processing software.

As for determining what receiver spacing is dense enough, it will vary from time to time depending on the dispersion relation curve. By setting ice thickness equal to 2 metes, and assuming a Young's Modulus of $8.7 \cdot 10^9$ Pa, as was done for the synthetic flexural waves generated for Datasets 1-3, it was revealed during the processing of the datasets that once the receiver spacing is increased from 5 meters to 6.25 meters, aliasing becomes quite problematic. To test this further, simple $f-k$ processing of the shot gather consisting of nothing more than flexural ice waves (figure 5.1) generated by a line source may be illustrated. When performing $f-k$ filtering of this shot gather with receiver spacing set

to 5, 6 and 7 meters, respectively, we obtain the results presented in figure 6.3. From the figure we see that once receiver spacing is above 6 meters, $f-k$ filtering becomes ineffective. In this particular case, then, dense enough receiver spacing would be less than approximately 6 meters. This again illustrates how accurate modelling of the dispersion relation and the flexural wave displacement may allow us to experiment with different receiver spacings on a computer prior to a survey in order to determine the receiver spacing necessary for $f-k$ filtering to be efficient.

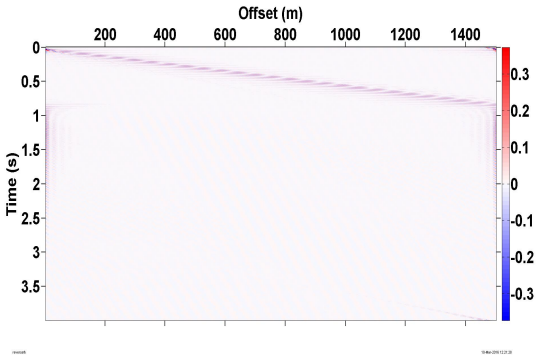

(a) Flexural waves after $f-k$ filtering with receiver interval of 5 meters.

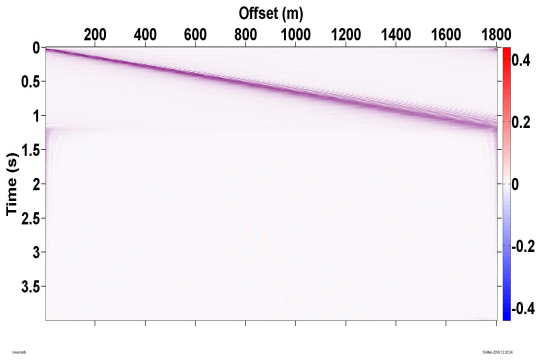

(b) Flexural waves after $f-k$ filtering with receiver interval of 6 meters.

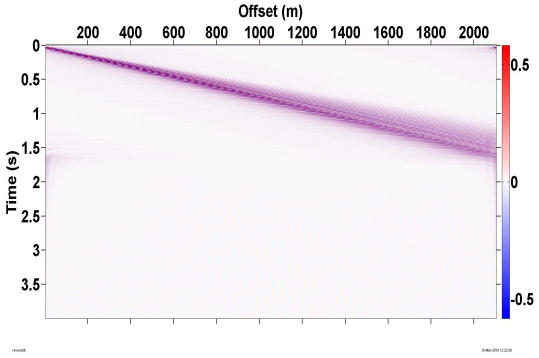

(c) Flexural waves after $f-k$ filtering with receiver interval of 7 meters.

Figure 6.3: $f-k$ filtering of flexural waves with varying receiver spacing.

Regarding the $\tau-p$ transform, it has been shown that if a distinct separation between flexural wave velocities and P-wave velocities in the sedimentary layers exist, $\tau-p$ filtering may be an efficient approach for separating signal and noise in the $\tau-p$ domain. This was especially the case for Datasets 4 and 5. It should once more be noted that during the processing, a certain degree of spatial aliasing in the $\tau-p$ domain was accepted as a trade-off for faster computation time. There are however, several algorithms that may be used implement the $\tau-p$ transform much faster than what was done in this thesis where the frequency domain approach outlined in Sacchi (2002), and presented in Appedix C,

was utilized. If a uniform sampling is used for both x and p, the matrix which is inverted during the transform is a so-called Toeplitz matrix, and several algorithms and methods may then be used to reduce computation time. For an overview of such methods, the reader is referred to Sarajaervi (2010).

Such algorithms were not implemented, however, but good results were nevertheless obtained for Datasets 4 and 5 despite the presence of some spatial aliasing artefacts. Yet, more refinement of the $\tau - p$ algorithms is definitely an issue which should be followed up, in particular in regards to studying the effects of the aliased noise, and then infer if the implementation of other $\tau - p$ algorithms which reduce computation time makes a noticeable difference or not in terms of noise reduction.

As was demonstrated on Dataset 3, unconventional methods must be used when conventional methods such as $f - k$ filtering and $\tau - p$ filtering come up short. For this study, the only unconventional method used has been the RT transform. Processing work done on Datasets 1 and 3 revealed that the transform may be used to effectively attenuate noise, but, in this case, the implemented RT transform has been rather crude. The program used for RT filtering assumes radial traces originating from the origin only, and the spectral clipping threshold is given as a fixed number for all processed traces in an input velocity array. For a better result, the spectral clipping threshold should, ideally, be trace dependent, and a more refined algorithm would therefore be needed for a more accurate filtering. As an example, consider the radial trace obtained from Dataset 1 along the trace $v = 1000$ m/s. By performing spectral clipping with spectral clipping threshold set equal to ten times the median value, we obtain the amplitude spectrum presented in figure 5.27b. If we compare this result with the amplitude spectrum obtained along the same trace for Dataset 1 prior to the addition of any flexural ice wave noise, we notice that the spectral clipping threshold may, in fact, attenuate signals too. This is illustrated in figure 6.4. We see that the signal is primarily present at low frequencies ($f < 100$ Hz). Subsequent to RT filtering, however, parts of this signal is attenuated, and the normalized amplitude value is only half of what it was originally. In addition, higher modes of the flexural ice wave are still present in the dataset as can be noticed by the peaks present at higher frequencies. Thus, although RT filtering does attenuate flexural ice waves, an improved spectral clipping method may yield better results.

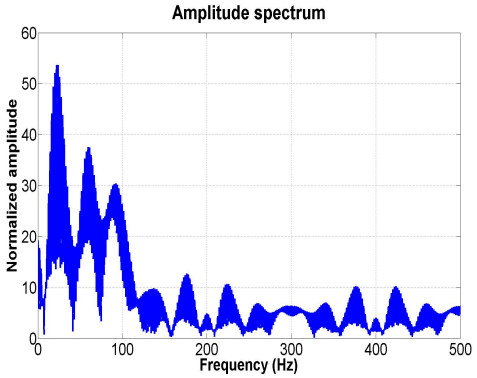

(a) The radial trace $v = 1000$ m/s in Dataset 1 prior to flexural wave noise addition.

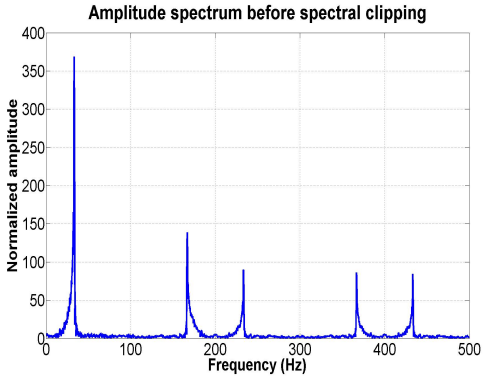

(b) The radial trace $v = 1000$ m/s in Dataset 1 after flexural wave noise addition.

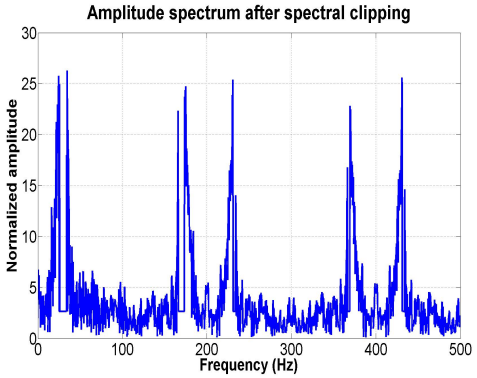

(c) The radial trace $v = 1000$ m/s in Dataset 1 after flexural wave noise addition and RT filtering.

Figure 6.4: The radial trace $v = 1000$ m/s in Dataset 1 prior to flexural wave noise addition and after flexural wave noise addition with RT filtering.

The problem of fine-tuning the spectral clipping technique to attenuate proper frequencies based on a normalized amplitude threshold value, brings up another issue worth noting - the issue of proper amplitude scaling. For Datasets 1-3 no flexural wave noise was initially present. Instead, noise was added by generating synthetic flexural ice waves and then adding this to the original seismic shot gathers. Once a synthetic shot gather featuring nothing but flexural wave noise has been generated, it must be scaled so that when the noise is added to a different seismic dataset, the relative magnitude values of the flexural ice waves are realistic in comparison to the signal magnitudes. This is difficult to achieve accurately, and for this thesis a trial-and-error approach was used to scale the synthetically generated noise. As noted in the introduction of this thesis, flexural wave noise tends to be of an order of magnitude $40-60$ dB higher than reflected signals (Rovetta et al., 2009). From figure 6.4 we see that the original signal has a normalized amplitude value of approximately 53 at its peak. After flexural wave noise addition, the peak value increases to approximately 370. Converting this to decibels, we obtain a maximum decibel

value of approximately 34.5 dB for the original radial trace, and a maximum decibel value of approximately 51 dB for the trace once flexural wave noise has been added. Thus, the order of magnitude is here approximately 16.5 decibels higher for the flexural wave noise than for the reflected signals, and this is somewhat lower than what we may observe in nature. As such, any time different synthetic datasets are combined, scaling inaccuracies may be present.

Overall, however, the attempted processing methods turned out to be quite efficient in dampening flexural wave noise and increasing the signal-to-noise ratio, but various approaches were required for different datasets. When conventional $f - k$ filtering fails, a combination of $\tau - p$ filtering and RT filtering supplemented with other filtering operations such as deconvolution, muting, scaling, etc., yielded promising results. It should be noted that more work could be done by incorporating other unconventional processing methods such as the methods outlined in Section 3.4. This could potentially provide even better knowledge as to which processing method would be most suitable when faced with different scenarios. For instance, as has been pointed out earlier in this thesis, RT filtering generally does not work very well if the ice thickness is highly varying (Del Molino et al., 2008). As such, in a scenario where receiver spacing is large, flexural wave velocities overlap with reflected wave velocities, and ice thickness varies considerably, none of the approaches outlined in this thesis may be fully effective. Thus, more research into unconventional processing methods could yield further information about the most efficient processing procedures in regards to flexural ice wave removal.

Nevertheless, the work performed for this study has hopefully provided a general framework for understanding the characteristic nature of the flexural ice wave, its dispersive nature, how physical parameters such as ice temperature and ice thickness affect dispersion, and the various processing challenges flexural ice waves pose. Through an investigation of the fundamental physics of the flexural wave as well as the attempted processing of flexural waves on numerous different datasets, the goal has been to propose, at the very least, some modelling and processing techniques that may be useful as a starting point for further studies of flexural ice waves.

6.2 Conclusions

In summary, the following conclusions may be drawn:

- Flexural ice waves may be modelled synthetically through a fluid-loaded thin plate theory as outlined in Yang and Yates (1995) in order to investigate the dispersion relation of the waves and estimate wave displacement in the $x - t$ domain.
- A decrease in ice temperature leads to an increase in the phase velocity of the dispersive wave. This follows from the increased stiffness of the elastic moduli as ice becomes colder. The increase in phase velocity with decreased temperature is most significant at the interval between approximately 0°C and −2°C as the ice is more slushy and may have more unfrozen pore water near 0°C.
- A decrease in ice temperature leads to an increase in the group velocity of the dispersive wave at low frequencies. At higher frequencies, group velocity is higher in the warmer ice layers, as the group velocity curves for the coldest ice layers start converging towards the phase velocity curves.
- An increase in ice thickness leads to an increase in the phase velocity of the dispersive wave because of the increased bending stiffness of the ice plate.
- An increase in ice thickness leads to an increase in the group velocity of the dispersive wave. At low frequencies, the thickest ice plate has the highest group velocity, but at higher frequencies, the thinner ice plates have the highest group velocity as the group velocity curves for the thickest layers start converging towards the phase velocity curves.
- Receiver spacing interval appears to be the primary factor in determining whether or not conventional processing approaches may be used for effective flexural ice wave removal.
- If receiver spacing is dense enough to avoid spatial aliasing, conventional $f - k$ filtering tends to be the simplest and most effective processing approach for flexural ice wave removal.
- If the velocity interval of the flexural ice waves is separate from the velocity interval of the reflected P-waves, $\tau - p$ filtering provides an efficient approach for

separating signal and noise in the $\tau - p$ domain provided that spatial aliasing can be reduced. Usually a trade off between aliasing effects and computation time must be considered.

- If conventional processing methods such as $f - k$ filtering and $\tau - p$ filtering fail, unconventional methods such as RT filtering with spectral clipping of flexural ice wave peak frequencies may be utilized.

- Sometimes the best processing result is achieved through a combination of various processing techniques. For the datasets processed in this thesis where $f - k$ filtering did not work, a combination of $\tau - p$ and RT filtering worked well in attenuating flexural ice waves and enhancing the signal-to-noise ratio. For Dataset 3. RT filtering was used as the primary processing technique, supplemented by subsequent $\tau - p$ filtering, whereas for Datasets 4 and 5, $\tau - p$ filtering was used as the primary processing technique followed by subsequent RT filtering of high velocity noise.

Appendix A

The characteristic equation for flexural ice waves

Here the derivation of the characteristic equations for flexural ice wave noise as outlined in Press and Ewing (1951a) will be presented. A sketch showing the wave displacement is included in figure A.1.

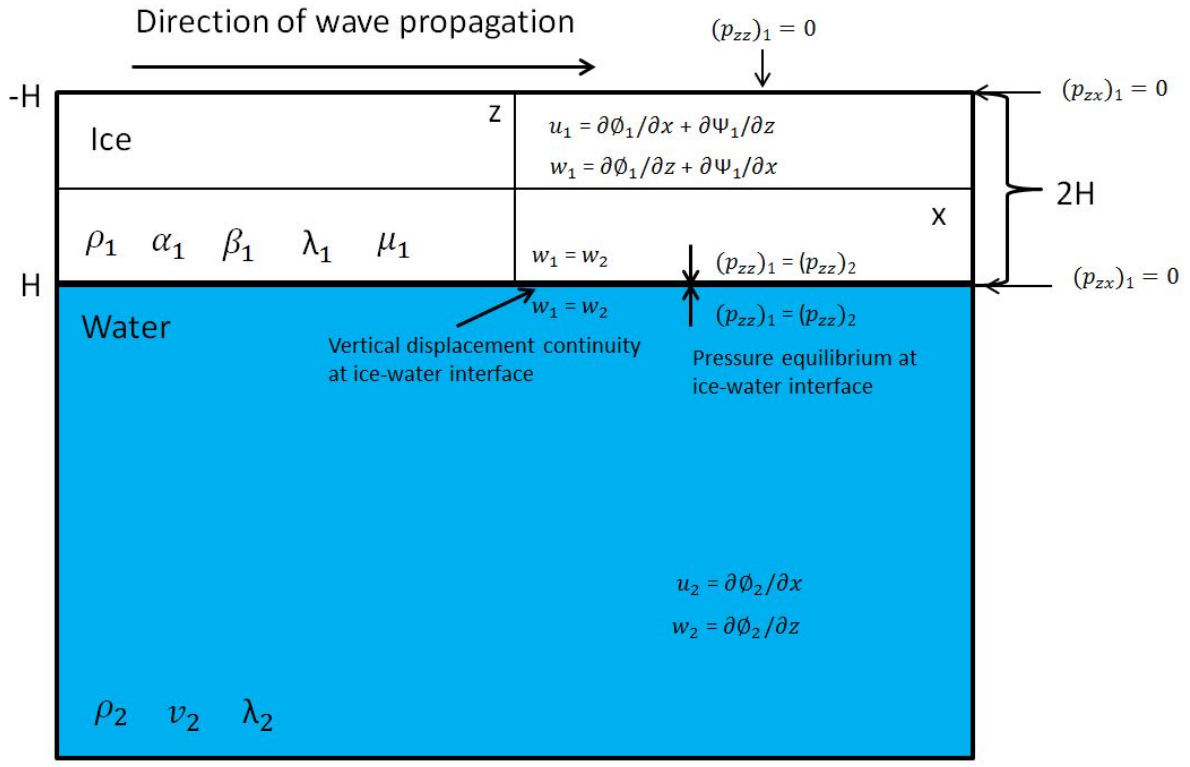

Figure A.1: Sketch of the displacements and boundary conditions in the Press and Ewing (1951a) derivation of the flexural wave period equations. Here u represents horizontal particle displacement and w represents vertical particle displacement. Subscript 1 refers to ice whereas subscript 2 refers to water.

We consider the propagation of elastic waves in an infinite, floating ice sheet with thickness $2H$, density ρ_1, in which the velocities of the compressional and shear waves are respectively α_1 and β_1. The underlying liquid has a density of ρ_2 and compressional wave velocity v_2. We assume the liquid layer to be infinitely deep. λ_1, μ_1 and Lamé's constants for the ice and λ_2 is the incompressibility of the liquid related to the elastic wave velocities as follows:

$$\alpha_1 = \sqrt{\frac{\lambda_1 + 2\mu_1}{\rho_1}} \quad \beta_1 = \sqrt{\frac{\mu_1}{\rho_1}} \quad v_2 = \sqrt{\frac{\lambda_2}{\rho_2}}, \tag{A.1}$$

which we recognize as the standard formulas for P- and S-velocity.

Now we choose a Cartesian coordinate system with the x-axis in the median plane of the ice sheet parallel to the propagation direction and the z-axis vertically downward. The subscripts 1 and 2 refer to the ice and liquid respectively. Next, we introduce the functions $\phi(x, z, t)$ and $\psi(x, z, t)$ defined by the equations:

$$\begin{aligned} u_1 &= \partial\phi_1/\partial x + \partial\psi_1/\partial z \\ w_1 &= \partial\phi_1/\partial z - \partial\psi_1/\partial x \\ u_2 &= \partial\phi_2/\partial x \\ w_2 &= \partial\phi_2/\partial z. \end{aligned} \tag{A.2}$$

Here u and w are the horizontal and vertical particle displacements. Notice that the shear components vanish in the liquid, which is consistent with the shear modulus being equal to zero here. SH waves are not included in this discussion. The vertical stress p_{zz} and the tangential stress p_{xz} can be expressed in terms of ϕ, ψ and the elastic constants in the following manner:

$$\begin{aligned} p_{zz} &= \lambda\nabla^2\phi + 2\mu(\partial^2\phi/\partial z^2 - \partial^2\psi/\partial x\partial z) \\ p_{xz} &= \mu(\partial^2\psi/\partial z^2 - \partial^2\psi/\partial x^2 + 2\partial^2\phi/\partial x\partial z). \end{aligned} \tag{A.3}$$

It is further required that ϕ and ψ satisfy the wave equations

$$\begin{aligned} \partial^2\phi_1/\partial t^2 &= \alpha_1^2\nabla^2\phi_1 \quad \text{in the ice} \\ \partial^2\psi_1/\partial t^2 &= \beta_1^2\nabla^2\psi_1 \quad \text{in the ice} \\ \partial^2\phi_2/\partial t^2 &= v_2^2\nabla^2\phi_2 \quad \text{in the liquid,} \end{aligned} \tag{A.4}$$

as well as the boundary conditions

$$\begin{aligned}
(p_{zz})_1 &= 0 \qquad \text{at } z = -H \\
(p_{zx})_1 &= 0 \qquad \text{at } z = -H \\
(p_{zz})_1 &= (p_{zz})_2 \qquad \text{at } z = H \\
(p_{zx})_1 &= 0 \qquad \text{at } z = H \\
w_1 &= w_2 \qquad \text{at } z = H.
\end{aligned} \tag{A.5}$$

Solving equation A.4 gives

$$\begin{aligned}
\phi_1 &= [A\sinh(\xi z) + B\cosh(\xi z)]\exp[i(kx - \omega t)] \\
\psi_1 &= [C\sinh(\eta z) + D\cosh(\eta z)]\exp(i(kx - \omega t)] \\
\phi_2 &= E\exp(-\zeta z)\exp[i(kx - \omega t)],
\end{aligned} \tag{A.6}$$

where

$$\begin{aligned}
\xi^2 &= k^2(1 - c^2/\alpha_1^2) \\
\eta^2 &= k^2(1 - c^2/\beta_1^2) \\
\zeta^2 &= k^2(1 - c^2/v_2^2),
\end{aligned} \tag{A.7}$$

and $c = \omega/k$ as defined in equation 2.5. In equation A.6, ϕ_1,ψ_1, and ϕ_2 make up a system of waves progressing in the x-direction with phase velocity c. ϕ_2 decreases exponentially with depth in the liquid as energy is lost by refraction into the liquid (Press & Ewing, 1951a).

By combining equations A.6, the boundary conditions from equations A.5, and equations A.2 and A.3, we obtain five independent homogeneous equations with five unknown amplitude coefficients (A, B, C, D, E). By simplifying the equations through assuming a Poisson ratio $\sigma = 0.25$ for ice so that $\lambda_1 = \mu_1$, we can write the period equation as

$$P[Q + \delta\cosh(\xi H)\cosh(\eta H) + Q[P + \delta\sinh(\xi H)\sinh(\eta H)] = 0, \tag{A.8}$$

where

$$\begin{aligned}
\delta &= \rho_2 v_2^2(\eta^2 - k^2)(\zeta^2 - k^2)\xi/\rho_1\beta_1^2 \\
Q &= (\eta^2 + k^2)^2\sinh(\xi H)\cosh(\eta H) - 4\xi\eta k^2\cosh(\xi H)\sinh(\eta H) \\
P &= (\eta^2 + k^2)\cosh(\xi H)\sinh(\eta H) - 4\xi\eta k^2\sinh(\xi H)\cosh(\eta H).
\end{aligned} \tag{A.9}$$

In equation A.8 an implicit relation between the phase velocity c and the angular frequency ω can be obtained by substituting $k = \omega/c$ - this is the dispersion relation of the flexural waves (Press & Ewing, 1951a).

Appendix B

Analytical derivation of formulae for estimating dispersion relation for flexural ice waves

The analytical solutions for estimating phase and group velocity dispersion based on the theory of Yang and Yates (1995) will here be presented.

From equation 2.40 we have, for each frequency in our frequency array, $k_f = (m\omega^2/D)^{1/4}$. Further, we define $k_0 = \omega/c_0$ and k as the horizontal wave number. In order to find the root of the denominator in equations 2.42 and 2.44, we define:

$$\Omega(k) = (k^4 - k_f^4)\gamma - \mu k_f^4 = 0. \tag{B.1}$$

From equation 2.39 we have

$$\gamma = (k^2 - k_0^2)^{1/2} \Rightarrow k^4 = \gamma^4 + 2\gamma^2 k_0^2 + k_0^4. \tag{B.2}$$

And using this as input in equation B.1, we obtain

$$\gamma^5 + 2k_0^2\gamma^3 + (k_0^4 - k_f^4)\gamma - \mu k_f^4 = 0. \tag{B.3}$$

This polynomial equation can then easily be solved numerically to find the γ value corresponding to each frequency value. From equation 2.39 we further have for the horizontal wave number, k:

$$\gamma = (k^2 - k_0^2)^{1/2} \Rightarrow k = \sqrt{\gamma^2 + k_0^2}. \tag{B.4}$$

And from this, we can now obtain the phase velocity for each frequency:

$$v_p = \frac{\omega}{k} = \frac{\omega}{\sqrt{\gamma^2 + k_0^2}}. \tag{B.5}$$

The denominator in equations 2.42 and 2.44 is then found through simple algebra:

$$\frac{\partial \Omega}{\partial k} = (k^4 - k_f^4)\frac{\partial \gamma}{\partial k} + 4k^3\gamma = (k^4 - k_f^4)\frac{k}{\gamma} + 4k^3\gamma, \tag{B.6}$$

where we, from equation B.2, can see that

$$\frac{\partial \gamma}{\partial k} = \frac{1}{2}(k^2 - k_0^2)^{-1/2} \cdot 2k = \frac{k}{\gamma}. \tag{B.7}$$

In order to derive the formula for group velocity, we use that:

$$v_g = -\frac{\partial \Omega / \partial k}{\partial \Omega / \partial \omega}. \tag{B.8}$$

An expression for $\partial\Omega/\partial k$ has already been derived in equation B.6. Combining equations 2.28 and 2.40, we obtain

$$k_f = (\rho h \omega^2 / D)^{1/4}. \tag{B.9}$$

And from this we define

$$\Omega(\omega) = (k^4 - k_f^4)\gamma(\omega) - \mu\frac{\rho h}{D}\omega^2. \tag{B.10}$$

We then obtain

$$\frac{\partial \Omega}{\partial \omega} = (k^4 - k_f^4)\frac{\partial \gamma}{\partial \omega} + (-2\frac{\rho h}{D}\omega)\gamma - 2\mu\frac{\rho h}{D}\omega. \tag{B.11}$$

From equation B.4 we can write

$$\gamma^2 = k^2 - \frac{\omega^2}{c_0^2}, \tag{B.12}$$

which then gives us

$$2\gamma\frac{\partial \gamma}{\partial \omega} = -2\frac{\omega}{c_0^2}, \tag{B.13}$$

so that we obtain

$$\frac{\partial \gamma}{\partial \omega} = -\frac{\omega}{\gamma c_0^2} = -\frac{k_0^2}{\omega\gamma}. \tag{B.14}$$

Plugging this expression for $\partial\gamma/\partial\omega$ into equation B.11, we then get

$$\frac{\partial\Omega}{\partial\omega} = \frac{-1}{\omega}\left[(k^4 - k_f^4)\frac{k_0^2}{\gamma} + 2k_f^4(\gamma+\mu)\right], \tag{B.15}$$

so that we finally obtain in equation B.8

$$v_g = \omega\frac{(k^4 - k_f^4)k/\gamma + 4k^3\gamma}{(k^4 - k_f^4)k_0^2/\gamma + 2k_f^4(\gamma+\mu)}. \tag{B.16}$$

Appendix C

Discrete $\tau - p$ transform via the frequency domain

The following derivation for how the forward and inverse $\tau - p$ transform may be carried out via the frequency domain is obtained from Sacchi (2002).

Assume that we have a seismogram consisting of $N = L_f - L_n$ traces, where the indices L_f and L_n denote far and near offset traces respectively. We then obtain, for the forward $\tau - p$ transform

$$s(p, \tau) = \sum_{l=L_n}^{L_f} p(x_l, \tau + px_l)\Delta x_l, \tag{C.1}$$

where $\Delta x_l = (x_{l+1} - x_l)$ for $l = L_n, \ldots, L_f - 1$. Similarly, the inverse $\tau - p$ transform is found via

$$p(x, t) = \sum_{j=J_{min}}^{J_{max}} s(x, t - px)\Delta p_j, \tag{C.2}$$

where $\Delta p_j = (p_{j+1} - p_j)$ for $j = J_{min}, \ldots, J_{max} - 1$. By taking the Fourier transform of the above equations, we obtain

$$S(p, f) = \sum_{l=L_n}^{L_f} P(x_l, f)e^{2\pi i f x_l p}\Delta x_l, \tag{C.3}$$

$$P(x, f) = \sum_{j=J_{min}}^{J_{max}} S(p, f)e^{-2\pi i f x p_j}\Delta p_j. \tag{C.4}$$

Using matrix notation, we may rewrite this transform and its adjoint as follows (f is

omitted in order to avoid notational clutter),

$$\mathbf{m} = \mathbf{L^H d}, \tag{C.5}$$

$$\widetilde{\mathbf{d}} = \mathbf{L m}. \tag{C.6}$$

Here the operators $\mathbf{L}$ and $\mathbf{L^H}$ form an adjoint pair. The matrix $\mathbf{L}$ is the forward operator, and the matrix $\mathbf{L^H}$ denotes the adjoint operator. The vector $\mathbf{m}$ represents the $\tau - p$ space $S(p, f)$ at discrete values of p and a fixed frequency f, whereas the vector $\mathbf{d}$ indicates the data $P(x, f)$ at discrete values of x and a fixed frequency f.

From the above derivations we see that equation C.5 maps the $t - x$ space into the $\tau - p$ domain, and the adjoint, equation C.6, maps the $\tau - p$ domain into the $t - x$ domain. Since $\mathbf{L}$ is non-orthogonal, $\mathbf{L}$ and $\mathbf{L^H}$ do not constitute an inverse pair. Thus, given $\mathbf{m} = \mathbf{L d}$, the problem is how to recover $\mathbf{d}$. A relationship between $\mathbf{d}$ and $\widetilde{\mathbf{d}}$ is obtained after substituting C.5 into C.6 so that one obtains

$$\widetilde{\mathbf{d}} = \mathbf{L L^H d}. \tag{C.7}$$

Assuming $\det(\mathbf{L L^H}) \neq \mathbf{0}$ in the band B where $f \in B$, we obtain

$$\mathbf{d} = (\mathbf{L L^H})^{-1} \widetilde{\mathbf{d}} = \mathbf{G}^{-1} \widetilde{\mathbf{d}}. \tag{C.8}$$

The $N \times N$ matrix $\mathbf{G} = \mathbf{L L^H}$ represents a discrete version of the ρ filter (see Section 3.2). Thus, the pair of transformations which map a signal from $f - x$ to $f - p$ and vice-versa is given by

$$\begin{aligned} \mathbf{m} &= \mathbf{L d} \\ \mathbf{d} &= \mathbf{G}^{-1} \mathbf{L m}. \end{aligned} \tag{C.9}$$

This system of equations may be solved via a least squares solution. If we assume that the data is a result of applying a slant stack operator to $\mathbf{m}$, we need to find the $\mathbf{m}$ that minimizes the objective function

$$J = \|\mathbf{d} - \mathbf{L m}\|^2. \tag{C.10}$$

The solution to this problem is the least squares solution

$$\mathbf{m} = (\mathbf{L^H L})^{-1}\mathbf{L^H d}. \tag{C.11}$$

In general, however, the inverse needs to be stabilized using a damping parameter

$$\mathbf{m} = (\mathbf{L^H L} + \mu\mathbf{I})^{-1}\mathbf{L^H d}. \tag{C.12}$$

This is the approach for computing the $\tau - p$ transform via the frequency domain.

Appendix D

MATLAB programs

The following is a list the MATLAB programs written specifically for this thesis:

'flexline.m' - Program for modelling flexural ice waves from line source

'flexsource.m' - Program for modelling flexural ice waves from point source

'tempdisp.m' - Program for estimating how ice temperature influences dispersion relation

'thicknessdisp.m' - Program for estimating how ice thickness influences dispersion relation

'dispviataup.m' - Program for estimating power spectrum of seismogram as a function of frequency and velocity via the $\tau - p$ transform. From the spectrum, the dispersion relation of the seismogram may be interpreted.

'mutext.m' - Program for muting events in the $x - t$ domain

'mutetp.m' - Program for muting events in the $\tau - p$ domain

'mutefk.m' - Program for muting events in the $f - k$ domain

'tapmute.m' - Program for tapering along edges of mutes

'fkprocess.m' - Program for performing $f - k$ filtering

'forwardfk.m' - Program for performing forward $f - k$ transform

'reversefk.m' - Program for performing reverse $f - k$ transform

'taupflow.m' - Program for performing $\tau - p$ filtering

'forwardtaup.m' - Program for performing forward $\tau - p$ transform

'reversetaup.m' - Program for performing reverse $\tau - p$ transform

'spikdectaup.m' - Program for performing spiking deconvolution in the $\tau - p$ domain

'RTfilter.m' - Program for performing RT filtering

'scaling.m' - Program for performing simple scaling of dataset

'preddec.m' - Program for performing predictive deconvolution for multiple attenuation

'reflections.m' - Program for modelling three synthetic reflectors for Dataset 1

Note that several of these programs call upon functions from the downloadable packages SeisLab 3.01 and SeismicLab.

Any reader interested in obtaining these programs is welcome to send an e-mail to `kjensen80@gmail.com`.

References

Achenbach, J. D. (1984). *Wave propagation in elastic solids.* New York: Elsevier.

Appendix B - Useful quantities. (n.d.). Retrieved 29.01.2016, from `http://people.ee.ethz.ch/~luethim/pdf/script/pdg/appendixB.pdf`

Auld, B. A. (1990). *Acoustic fields and waves in solids, volume ii.* Malabar, Florida: Robert E. Krieger Publishing Company.

Austegard, A., & Rondenay, S. e. (2013). *Processing of multichannel seismic data: An introduction, including exercises and matlab programs.* Bergen, Norway: Department of Earth Science, University of Bergen.

Bakke, S. (2015). *Seismiske bølger i havis* (Unpublished master's thesis). Department of Earth Science, University of Bergen, Bergen, Norway.

Barr, F. J., Nyland, D. L., & Sitton, G. A. (1993). *Attenuation of flexural ice waves and random noise using both geophones and hydrophones.* 1993 SEG Annual Meeting.

Basak, R. L., Rana, K. S., Rao, A. K., Gangaiah, A., & Chandrasekaran, C. R. (2012). *Removal of noises using tau-p transformation - an indigenous tool for noise attenuation in shallow seismic data.* 9th Biennial International Conference and Exposition on Petroleum Geophysics, Hyderabad, India.

Beresford-Smith, G., & Rango, R. N. (1988). Dispersive noise removal in t-x space: Application to arctic data. *Geophysics*, *53*(3), 346-358.

Brincker, R., Lagö, T. L., Andersen, P., & Ventura, C. (2007). *Improving the classical geophone sensor element by digital correction.* Proceedings of the International Model Analysis Conference, Orlando, FL, USA, Feb. 19-22, 2007.

Claerbout, J. (1975). *Slant-stacks and radial traces.* Stanford Exploration Project Report, SEP-5, 1-12.

Cox, G., & Weeks, W. (1974). Salinity variations in sea ice. *Journal of Glaciology*, *13*(67), 109-120.

Cox, G., & Weeks, W. (1983). Equations for determining the gas and brine volumes in sea-ice samples. *Journal of Glaciology*, *29*(102), 306-316.

Del Molino, G., Andreoletti, C., Sandroni, S., Poletto, F., Farina, B., Bellezza, C., & Lovo, M. (2011). Seismic interferometry application to improve seismic reflection signals affected by ice-plate flexural noise. *The Leading Edge*, *30*(5), 538-545.

Del Molino, G., Rovetta, D., Mazzucchelli, P., Sandroni, S., Rizzo, F., & Andreoletti, C. (2008). *Seismic exploration on ice: the flexural wave noise challenge.* SEG Las Vegas 2008 Annual Meeting.

Ewing, M., & Crary, A. (1934). Propagation of elastic waves in ice. part ii. *Journal of Applied Physics*, *5*(7), 181-184.

Ewing, M., Crary, A., & Thorne Jr, A. (1934). Propagation of elastic waves in ice. part i. *Journal of Applied Physics*, *5*(6), 165-168.

Gardner, G. H. F., & Lu, L. e. (1991). *Slant-stack processing.* Tulsa, Oklahoma: Society of Exploration Geophysicists.

Gonzalez, R., Woods, R., & Eddins, S. (2004). *Digital image processing using MATLAB.* Upper Saddle River, New Jersey, USA: Pearson Education, Inc.

Henley, D. C. (2003). Coherent noise attenuation in the radial trace domain. *Geophysics*, *68*(4), 1408-1416.

Henley, D. C. (2004). *Effective noise attenuation and deconvolution in the radial trace domain.* SEG International Exposition and 74th Annual Meeting, Denver, Colorado, 10-15 October 2004.

Henley, D. C. (2006). *Attenuating the ice flexural wave on arctic seismic data.* 2006 SEG Annual Meeting.

Henley, D. C. (2009). A convenient truth: Radial trace filtering - simple and effective. *CSEG Recorder*, *January issue*, 16-26.

Hunkins, K. (1995). Seismic studies on sea ice. *Journal of Geophysical Research*, *65*(10), 3459-3472.

Jensen, M. (2015). *Metodar for demping av fleksurbølgjer i havis* (Unpublished master's thesis). Department of Earth Science, University of Bergen, Bergen, Norway.

Johansen, T. A., Ruud, B. O., Bakke, N. E., Riste, P., Johannessen, E. P., & Henningsen, T. (2011). Seismic profiling on arctic glaciers. *First Break*, *29*(2), 65-71.

Kohnen, H. (1974). The temperature dependence of seismic waves in ice. *Journal of Glaciology*, *13*(67), 144-147.

Krebes, E. S. (2004). Seismic forward modeling. *CSEG Recorder*, *April issue*, 28-39.

Lamb, H. (1889). On the flexure of an elastic plate. *Proceedings of the London Mathematical Society*, *s1-21*(1), 70-91.

Lamb, H. (1917). On waves in an elastic plate. *Proceedings of the Royal Society of London*, *93*(648), 114-128.

Langleben, M. P., & Pounder, E. R. (1963). Elastic parameters of sea ice. In Kingery, W. D., (ed.). *Ice and show; properties, processes, and applications: proceedings of a conference held at the Massachusetts Institute of Technology, February 12-16, 1962*, 69-78.

Lansley, R. M., Eilert, P. L., & Nyland, D. L. (1984). *Surface sources on floating ice: The flexural ice wave.* 1984 SEG Annual Meeting.

Mellor, M. (1983). *Mechanical behavior of sea ice.* Hanover, New Hampshire: CRREL Monograph 83-1.

Mæland, E. (2005). *Prosessering av seismiske data.* Bergen, Norway: Department of Earth Science, University of Bergen.

Müller, G. (1985). The reflectivity method: a tutorial. *Journal og Geophysics*, *58*, 153-174.

Oliver, A., Crary, P., & Cotell, R. (1954). Elastic waves in arctic pack ice. *Transactions, American Geophysical Union*, *35*(2), 282-292.

Osborne, M. F. M., & Hart, S. D. (1945). Transmission, reflection, and guiding of an exponential pulse by a steel plate in water. I. Theory. *The Journal of the Acoustical Society of America*, *17*(1), 1-18.

Pounder, E. (1965). *The physics of ice.* Oxford: Pergamon Press. (The Commonwealth and International Library, Geophysics Division).

Press, F., & Ewing, M. (1951a). Propagation of elastic waves in a floating ice sheet. *Transaction, American Geophysical Union*, *32*(5), 673-678.

Press, F., & Ewing, M. (1951b). Theory of aircoupled flexural waves. *Journal of Applied Physics*, *22*(7), 892-899.

Proubasta, D. (1985). Ice saw - an incisive solution to seismic noise. *The Leading Edge*, *4*(10), 18-23 and 82.

Pujol, J. (2003). *Elastic wave propagation and generation in seismology.* Cambridge, United Kingdom: Cambridge University Press.

Rendleman, C. A., & Levin, F. K. (1990). Seismic exploration on a floating ice sheet. *Geophysics*, *55*(4), 402-409.

Rice, S. L., Dudley, T., Schneider, C., Pierce, R. J., Horn, B., Cameron, S., ... Zhou, Z.-Z. (2013). Arctic seismic acquisition and processing. *The Leading Edge*, *32*(5), 546-554.

Rovetta, D., Mazzucchelli, P., Del Molino, G., & Sandroni, S. (2009). *Flexural ice wave: modelling by analytical approach.* SEG Houston 2009 International Exposition and Annual Meeting.

Sacchi, M. D. (2002). *Statistical and transform methods in geophysical signal processing.* Edmonton, Canada: Department of Physics, University of Alberta.

Sarajaervi, M. (2010). *Inversion of the linear and parabolic radon transform* (Unpublished master's thesis). Department of Earth Science, University of Bergen, Bergen, Norway.

Schuster, G. T. (2010). *Seismic interferometry.* Cambridge, United Kingdom: Cambridge University Press.

Shei, S., Ward, R. W., & Veith, K. F. (1983). *Flexural waves in floating ice.* 1983 SEG Annual Meeting, 11-15 September, Las Vegas, Nevada.

Smith, S. W. (2003). *Digital signal processing: A practical guide for engineers and scientists.* Newnes.

Soubaras, R. (2001). *Dispersive noise attenuation for converted wave data.* 2001 SEG International Exposition and Annual Meeting.

Sunwall, D. A., Speece, M. A., & Pekar, S. F. (2012). Advances in on-sea-ice seismic reflection methods using an air gun: Mcmurdo sound, antarctica. *Geophysics*, *77*(1), 19-30.

Timco, G., & Weeks, W. (2010). A review of the engineering properties of sea ice. *Cold Regions Science and Technology*, *60*(2), 107-129.

Tran, T., Nguyen, K., Sacchi, M., & Le, L. (2014). Imaging ultrasonic dispersive guided wave energy in long bones using linear radon transform. *Ultrasound in Medicine and Biology*, *40*(11), 2715-2727.

Treitel, S., Gutowski, P. R., & Wagner, D. E. (1982). Plane-wave decomposition of seismograms. *Geophysics*, *47*(10), 1375-1401.

Trupp, R., Hastings, J., Cheadle, S., & Vesely, R. (2009). Seismic in arctic environs: Meeting the challenge. *The Leading Edge*, *28*(8), 936-942.

Turner, G. (1990). Aliasing in the tau-p transform and the removal of spatially aliased coherent noise. *Geophysics*, *55*(55), 1496-1503.

United States Geological Survey - Circum-Arctic Resource Appraisal Assessment Team. (2008, july). *Circum-arctic resource appraisal: Estimates of undiscovered oil and gas north of the arctic circle* (Tech. Rep.).

Viktorov, I. A. (1967). *Rayleigh and lamb waves: Physical theory and applications.* New

York: Plenum Press.

Wapenaar, K., Dragaonv, D., Snieder, R., Campman, X., & Verdel, A. (2010). Tutorial on seismic interferometry: Part 1-basic principles and applications. *Geophysics*, *75*(5), 195-209.

Weeks, W. F., & Assur, A. (2009). *The mechanical properties of sea ice.* Hanover, New Hampshire: CRREL Monograph IIC3.

Yang, T. C., & Giellis, G. R. (1994). Experimental characterization of elastic waves in a floating ice sheet. *The Journal of the Acoustical Society of America*, *96*(5), 2993-3009.

Yang, T. C., & Yates, T. W. (1995). Flexural waves in a floating ice sheet: Modeling and comparison with data. *The Journal of the Acoustical Society of America*, *97*(2), 971-977.

Yilmaz, O. (2001). *Seismic data analysis: Processing, inversion, and interpretation of seismic data: Vol. 2.* Tulsa, Oklahmoa, USA: Society of Exploration Geophysicists.